Characterization of Coupled Transport Phenomena in Large-Format Lithium-Ion Batteries



Howie N. Chu

St Peter's College

University of Oxford

A thesis submitted for the degree of

Doctor of Philosophy

Trinity 2021

This is dedicated to the people who didn't choose to do a PhD,
but had to deal with the people who did.

Acknowledgements

First of all, I hate every single one of you for not letting me quit when I wanted to, you know who you are. I don't think I can get away with not saying that if I want this to sound like I'm genuinely thanking everyone that has helped me through these years.

I would like to thank Prof. Charles Monroe for granting me the freedom to do basically whatever I wanted in the lab and for providing guidance whenever it was needed. It was great being in this group. Thanks to Dr. James Saraidaridis and Dr. Tianhong Hou for making the transition from Michigan to Oxford as smooth as it was. Thanks to Dr. Priyamvada Goyal for appreciating my occasionally dark humor. Thanks to Andrew and Kirk for the never-boring science and stock market talks, in and out of Begbroke. Thanks to Dr. Guanchen Li and Dr. Jie Lin for being modeling references in a field I was unfamiliar with. To Trishna, thanks for being the first person in Oxford to understand my obscure meme references.

To my parents and grandparents, thanks for supporting me even though I'm pretty sure none of you knew what I was doing or were particularly thrilled with me leaving. Also, I'm forever grateful that my family eventually figured out to stop asking me how much longer it will take me to finish. To the friends from high school, William, Courtland, Jeffrey, and Cynthia, I was terrible at keeping in touch through the years, but I appreciated every time you reached out to check up on me.

To Jenn, thanks for sticking with me and supporting me through every single move away from New York, from Pennsylvania, California, Michigan, and finally, to Oxford. Thanks for listening to my depressive ramblings and the incessant whining about quitting and working at Whole Foods, but willing to support me even if that was what I ended up doing. Your unconditional love and support were what got me through it all. I've finally finished writing this dissertation and I'm coming home.

P.S., thanks Bill Gates.

Abstract

Large-format lithium-ion batteries are inherently complicated systems, consisting of many stacks of repeating current-collector/cathode/separator/anode/current-collector structures. When a current is applied to either charge or discharge the battery, a multitude of processes occur, which are, more often than not, coupled to each other. The movement of lithium ions from one electrode to the other during charge/discharge can also generate large amounts of heat, and the positioning of the tabs can make the temperature distribution highly non-uniform. The same process can also cause the electrodes to volumetrically expand and contract when the lithium ions move in or out of it. This non-uniformity, although being an unwanted side effect, offers a method of looking at how lithium-ions move through the battery from an external viewpoint. Taking local measurements and assembling them into a spatial map – whether of temperature or strain – provides insight into the coupled transport processes.

By tracking the temperature non-uniformity and a few characteristic features of the voltage signal that result in response to a squarewave input signal, a streamlined 3D model was proposed to simulate large-format lithium-ion batteries of two different chemistries and shapes in Chapter 2. The electrochemical behavior was described by the Newman-Tobias porous-electrode theory, which was coupled to a local heat balance. Dimensional analysis was done to justify a simplification in which the many-layered geometry could be represented by a single stack of the individual components, dramatically speeding up computation. By matching the simulation output to the experimental data, material property values were extracted that adequately describe the observable thermal and electrical behavior of the batteries. Providing a method of parameter estimation that can resolve many parameters at once through a single experiment. In Chapter 3, the inverse modelling approach was used to study battery degradation by tracking the changes to the extracted material property values. By looking at which parameters changed and by how much, the degradation mechanism that can result in these variations can be inferred.

Intercalation/deintercalation-induced mechanical strain and stress effects in batteries are easily convoluted with temperature effects because of thermally induced volume change. Typically, experiments are designed with the intention of minimizing thermal contributions, so that a single point measurement of temperature

describes the whole cell. But cells do not always satisfy this assumption in practice, consequently, in Chapter 4, an experimental rig that simultaneously measures cell surface temperature and dilation non-invasively was designed and built. The apparatus consisted of multiple non-contact sensors, such as an IR sensor/camera and two laser profilers. The setup measured both temperature and dilation simultaneously under the effects of various high-rate current signals and the relaxation that followed, which provided a means to probing the relative contributions of intercalation and temperature induced volume change.

Contents

List of Figures xiii

List of Tables xvii

List of Abbreviations xix

1 Introduction and Background 1
- 1.1 Motivation . . . 1
- 1.2 Length scales within batteries . . . 3
- 1.3 Side processes through various length scales . . . 4
  - 1.3.1 Thermal response . . . 4
  - 1.3.2 Mechanical response . . . 5
- 1.4 Characterization techniques . . . 6
  - 1.4.1 Electrochemical Measurements . . . 7
  - 1.4.2 Thermal measurements . . . 9
  - 1.4.3 Mechanical Measurements . . . 11
- 1.5 Summary . . . 12

2 Electrochemical/Thermal Characterization and Modeling 15
- 2.1 Introduction . . . 15
- 2.2 Design of experiments . . . 18
  - 2.2.1 Experimental Apparatus Design . . . 18
  - 2.2.2 Input Signal . . . 21
  - 2.2.3 Infrared Thermography . . . 22
- 2.3 Modeling . . . 26
  - 2.3.1 Newman–Tobias Porous Electrode Theory . . . 26
  - 2.3.2 General Energy Balance . . . 30
- 2.4 COMSOL Multiphysics and model implementation . . . 33
  - 2.4.1 Non-dimensionalization . . . 33
  - 2.4.2 Scaling laws for multilayer cells . . . 36
  - 2.4.3 Model implementation and parameter estimation . . . 38
- 2.5 Results and discussion . . . 41
- 2.6 Conclusions . . . 45

3 State of Health Tracking using Lock-in Thermography 47
3.1 Introduction . . . 47
3.2 Experimental . . . 49
3.2.1 Experimental Apparatus Design Update . . . 49
3.2.2 Matte Paint Effects . . . 52
3.2.3 Thermal Characterization of Pristine Kokam Cells . . . 54
3.2.4 Degradation conditions . . . 58
3.2.5 Characterizing Degraded Kokam Cells Using Lock-in Thermography . . . 61
3.3 Results and discussion . . . 65
3.3.1 Modeling and optimization . . . 65
3.3.2 Fitting and Validation results . . . 68
3.4 Conclusions . . . 76

4 Electrochemical/Thermal/Mechanical Measurements 81
4.1 Introduction . . . 81
4.2 Equilibrium stress measurements . . . 84
4.3 Experimental setup for laser dilatometry . . . 87
4.3.1 Frame update . . . 87
4.3.2 Laser Profilers . . . 88
4.4 Scanning laser dilatometry with IR camera measurements . . . 91
4.5 Localized laser dilatometry with IR sensor measurements . . . 97
4.6 Conclusions . . . 103

5 Conclusions and future work 105
5.1 Summary . . . 105
5.2 Future work . . . 107
5.2.1 Streamlined electrochemical/thermal model . . . 107
5.2.2 Electrochemical/thermal/mechanical apparatus: experiments and upgrades . . . 109
5.3 Conclusions . . . 110

Appendices

A Supplementary fitting results 115
A.1 Various temperature and voltage fittings for Kokam NMC cells . . . 115

References 121

List of Figures

1.1 Modified images from patents [4, 5] representing stacked electrode configuration (a) and flatwound jellyroll configuration (b) with relevant components colored and labeled for ease of identification. . . . 4

1.2 Temperature distribution of A123 15 Ah battery measured using an array of thermocouples [54] (a) and schematic depicting current path inside of large-format pouch cells (b). 10

2.1 Three infrared images ($\Delta T = T - T_\infty$) of the surface of a 20 Ah lithium-ion battery cell, under 4C charge-discharge cycling with 100 s period, freely hanging in stagnant air with $T_\infty = 25°C$. To illustrate how surface temperature develops, the images show the temperature of an initially isothermal battery after (left) 5 min, (center) 20 min, and (right) 45 min of continuous cycling. 16

2.2 Acrylic frame drawing with render for use with A123 20 Ah pouch cells 20

2.3 Nylon front and back plates for electrical connections to A123 20 Ah pouch cells. The part on the left in the render depicts the nylon piece with the silicone rubber pads glued in and the part on the right is the front plate that houses the press fitted copper bars. 21

2.4 Free standing unistrut frame for supporting the cell holders. Labeled measurements refer to the length of the piece of unistrut. The bronze colored beam is used to prevent the uprights from being askew. . . 21

2.5 Examples of thermocouple arrays from the works of Mastali *et al.* and Kim[54, 95] 23

2.6 (a) Assembled battery holder with prismatic cell and (b) FLIR A35sc camera. (c) Completed experimental setup. 24

2.7 General (a) electrical and (b) thermal responses to AC squarewave current. Characteristic features used for sensitivity testing of the thermoelectrochemical model are labeled on the figures. 26

2.8 Pseudo-OCP curves for A123 20 Ah cell at 25 °C, generated by galvanostatic cycling at C/25 29

2.9 A plot of $\frac{dV}{dSOC}$ for the pseudo-OCP curves from Figure 2.8, used for k_U estimation 38

2.10 Geometry (left,colored) and mesh (right) that were implemented in COMSOL for the simulations. The copper bars were added to more closely mimic the experimental setup. 41
2.11 Comparison of model output and experimental data for three different excitation tests of the LFP cell for (a) 4c100s, (b) 2c100s, and (c) 4c50s input signals. The plots in (a) were the result of data fitting, while (b) and (c) were validation tests obtained by using the parameter set from (a). 42

3.1 Acrylic frame drawing with render for Kokam 16 Ah pouch cells . . 51
3.2 Nylon frame drawing for Kokam 16 Ah pouch cells 51
3.3 Complete cell holders for Kokam 16 Ah cells (left) and A123 20 Ah cells (right) 52
3.4 Thermogram of a Kokam cell without a layer of matte paint. 53
3.5 Thermograms of a Kokam cell with (a) no spray paint applied and (b) a layer spray paint applied, at various times during a squarewave excitation experiment. 54
3.6 Series of thermograms showing two pristine cells (labelled KKMG and KKMI) undergoing a 5c100s experiment after 2500 seconds. . . 55
3.7 Processed $T_{\max}$, T_{avg}, $T_{\min}$, and V data for cells KKMG (red) and KKMI (green). 57
3.8 Percent change between KKMG and KKMI for the four datasets used to run the parameter extraction. 57
3.9 Capacity *vs.* cycle number plots for cells KKMB and KKMF. Capacity checks were performed by discharging the battery from full at a C-rate of C/25 to a lower voltage limit of 2.71 V. 60
3.10 Initial and final POCV curves, and DVA for cells (a) KKMB [25°C cycling] and (b) KKMF [10°C cycling]. 61
3.11 ΔT thermograms of a pristine Kokam cell *vs.* cells degraded in a cold 10° C ambient and in a standard 25° C ambient. The three chosen time frames, 275, 750, and 1600 seconds were chosen to represent the initial, middle, and final stages of the squarewave experiment. . . . 62
3.12 Percent change at various time steps comparing the temperature distributions for the pristine cell and the two degraded cells. 63
3.13 $T_{\max}$, T_{avg}, $T_{\min}$, and V data sets for the pristine, cold degraded, and ambient degraded cells. 64
3.14 Experimental thermogram for Kokam cell undergoing squarewave testing (left) compared to simulated thermogram under the same conditions (right). 66

3.15 Pristine cell (KKMG) fitting results for a 5c100s squarewave in the top row, followed by 3c100s and 5c50s validations at a mean SOC of 50%. 70
3.16 Pristine cell (KKMG) fitting results for a 4c100s squarewave in the top row, followed by 2c100s and 4c50s validations at a mean SOC of 30%. 71
3.17 Pristine cell (KKMG) fitting results for a 5c100s squarewave in the top row, followed by 3c100s and 4c50s validations at a mean SOC of 60%. 72
3.18 Cold degraded cell fitting results for a 4c100s squarewave in the top row, followed by 2c100s and 4c50s validations at a mean SOC of 50%. 73
3.19 Ambient degraded cell fitting results for a 4c100s squarewave in the top row, followed by 2c100s and 4c50s validations at a mean SOC of 50%. 74

4.1 Stress response of prismatic cells after applying a change in SOC or a change in ambient temperature. (a) Represents the stress response under a preloaded stress of 15.5 PSI and (b) represents the stress response under a preloaded stress of 21.5 PSI. 85
4.2 Updated T-slot frame to hold cell holders in an upright position with components and dimensions 88
4.3 Drawings for various components used to assemble the holder used to carry the laser profilers 89
4.4 (a) Belt and ball screw driven motorized stage configuration and (b) completed laser assembly. The four holes of the adapter plate are used to bolt the entire assembly in (b) to the vertical stage's platform. 90
4.5 Hook up diagram between Sparkfun Redboard (microcontroller) and two Sparkfun Autodrivers (stepper motor drivers) 92
4.6 Render of assembled laser rig on motorized stages with IR camera. . 93
4.7 Sample dataset of the battery thickness (top) and sample dataset from the IR camera in the same area captured by the lasers (bottom). 94
4.8 Single profile of battery thickness with filtered data (left), FFT output of the single profile (middle), and tallied occurrence of frequency signals in every scan of the 2C CCCV experiment (right). 94
4.9 Filtered upper edge scan of a Kokam 16 Ah pouch cell showing cell thickness separated by dashed lines to represent the different horizontal areas for analysis (left). Average expansion of the areas highlights on the left plot as a function of SOC (right). 96

4.10 Filtered upper edge scan of a Kokam 16 Ah pouch cell showing cell thickness separated by dashed lines to represent the different vertical areas for analysis (left). Average expansion of the areas highlights on the left plot as a function of SOC (right). 96
4.11 Detailed drawings of the acrylic IR sensor holder that is attached to the laser profilers. 98
4.12 Calculated cell thickness (top) with FFT analysis of the data signal (bottom) 99
4.13 Volume change and temperature change *vs* time in the squarewave analysis experiment (left), and volume change *vs* temperature change (right). 100
4.14 Center volume change of Kokam 16 Ah pouch cell with temperature effects removed 100
4.15 Data from Figure 4.9 and Figure 4.10 replotted with thermally induced volume change effects taken out. 101
4.16 Bandpass output of the volume expansion and temperature data with the current input as a reference 102

A.1 Cold degraded cell fitting results for a 4c100s squarewave in the top row, followed by 2c100s and 4c50s validations at a mean SOC of 30%. 116
A.2 Cold degraded cell fitting results for a 4c100s squarewave in the top row, followed by 2c100s and 4c50s validations at a mean SOC of 60%. 117
A.3 Ambient degraded cell fitting results for a 4c100s squarewave in the top row, followed by 2c100s and 4c50s validations at a mean SOC of 30%. 118
A.4 Ambient degraded cell fitting results for a 4c100s squarewave in the top row, followed by 2c100s and 4c50s validations at a mean SOC of 60%. 119

List of Tables

2.1 Parameter values for fitting the 4c100s squarewave data. The modified values were implemented to recreate a reasonable reaction distribution in the porous electrode after simplifying its geometry. . 43
2.2 A123 20 Ah electrode and current collector fixed parameters used in the model. 44

3.1 Kokam SLPB75106205 specifications 50
3.2 Extracted parameter sets for fresh cells, KKMG and KKMI at 50% SOC. 56
3.3 Degradation overview of the Kokam cells chosen for this study . . . 59
3.4 Kokam fixed parameters used in optimization 68
3.5 Effective thermal conductivity (W m^{-1} K^{-1}) and ionic conductivity (S m^{-1}) changes at the three different tested SOCs for the pristine and degraded cell comparisons 76
3.6 Pristine Kokam cell parameters 77
3.7 Cold degraded Kokam cell parameters 78
3.8 Ambient degraded Kokam cell parameters 79

List of Abbreviations

CC . . . . . Constant current.

CCCV . . . . . Constant-current constant-voltage.

CV . . . . . Constant voltage.

DCIR . . . . . Direct current internal resistance.

DVA . . . . . Differential voltage analysis.

ECM . . . . . Equivalent circuit model

EIS . . . . . Electronic impedance spectroscopy.

FFT . . . . . Fast Fourier transform.

GITT . . . . . Galvanostatic intermittent titration technique.

(H)EV . . . . . (Hybrid) Electric vehicle.

ICA . . . . . Incremental capacity analysis.

IR . . . . . Infrared

KKM . . . . . Kokam

LCO . . . . . Lithium cobalt oxide

LFP . . . . . Lithium iron phosphate.

LLI . . . . . Loss of lithium inventory

LVDT . . . . . Linear variable differential transformer.

NMC . . . . . Nickel manganese cobalt

OCV . . . . . Open circuit voltage.

POCV . . . . . Pseudo-OCV.

SEI . . . . . Solid electrolyte interphase.

SOC . . . . . State of charge.

SOH . . . . . State of health.

1 Introduction and Background

1.1 Motivation

Large format lithium-ion batteries have become the go-to choice for use in electric vehicles because of their attractive gravimetric and volumetric energy densities and relatively low manufacturing costs. Management of these systems is difficult because a variety of complex physical processes occur when a battery is put under an electric load. These processes are often coupled to other phenomena, and they inevitably produce side effects that are often undesired. Without thorough understanding of the coupled phenomena, the simplest solution currently employed is to operate the battery packs under restricted control conditions to minimize exposure to cell states where these side effects can manifest. Side effects such as heat generation and mechanical fatigue can cause cells to degrade incrementally until they are no longer operational – a state typically decided by some pre-established amount of capacity loss. Further insight into this state can be probed *via* other experimental methods such as measuring internal resistances and analyzing the discharge/charge curves. In worst-case scenarios, excessive heat generation and physical short circuits can cause catastrophic failures.

As wider varieties of vehicles undergo electrification and the demand for these electric vehicles (EV) increases, and also because the performance of newer battery

packs is always improving, it is reasonable to expect greatly increased amounts of hazardous waste in the foreseeable future from retired packs. Although simply disposing of all of these cells raises environmental concerns, recycling processes have not yet developed to a point where the pros outweigh the cons (from both economic and environmental viewpoints). But with lithium-ion's continual increase in popularity across many applications, extending the useful life of a battery pack and the cells that comprise it through alternative use cases that exploit partially degraded cells may become a viable solution.

There is a large body of research dedicated to understanding degradation mechanisms in different battery chemistries. Understanding the performance limits of battery packs with time and usage is important to determine when a pack is no longer suitable for its intended use. Even after their 'first life' powering EVs, packs can still retain 50-80% of their initial capacity and can be used in less power hungry 'second life' applications such as stationary storage.

In order to give battery cells a second life, diagnostic tools and techniques will have to be developed to determine performance limits. Along with their reduced capacity and power delivery capabilities, performance may be limited by less considered factors such as heat generation/dissipation signatures and the extent of internal mechanical fatigue. Characterization techniques are often postmortem, requiring cutting open the cells to probe for degradation signatures. For example, various microscopic and spectroscopic methods are used to check for physical damage and crystal structure changes in the electrodes [1–3]. Clearly this renders the cell useless and destines it for landfill or a recycling plant. New diagnostic techniques to inform second-life capabilities will have to be non-destructive. A thorough understanding of the many electrochemical, thermal, and mechanical processes that occur within a battery — and how they interact with each other can — guide how to perceive some of these effects noninvasively.

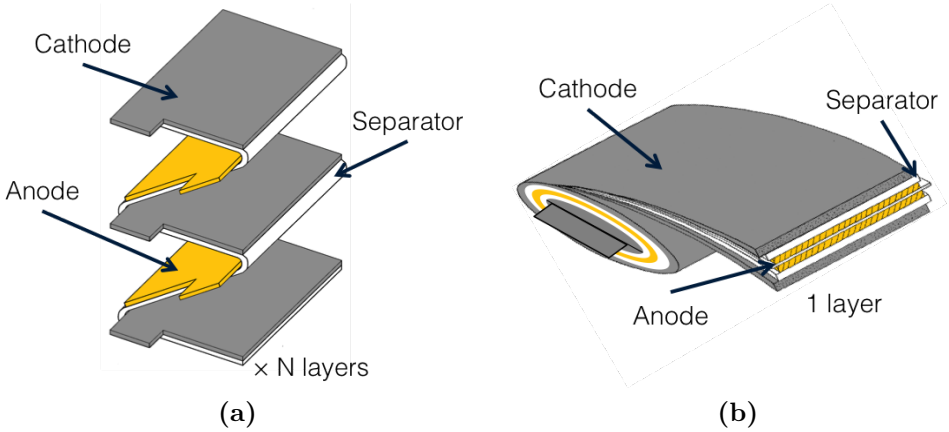
The objective of this research is to develop the understanding of how coupling among charge evolution, strain evolution, heat evolution, and heat transfer impact a battery cell's performance. Furthermore, we aim to leverage that understanding

to, develop a suite of tools and techniques that allow quick diagnoses of cells for second-life applications. Understanding the coupling among the various transport processes, and their effects on thermal and mechanical behavior, can help inform the design of control schemes that offer safer operation and more efficient usage of a battery's active materials.

1.2 Length scales within batteries

To study how matter and heat are transported within the materials comprising a battery, it is important to understand a cell's design and fabrication process. Active materials such as graphite for the anode and various transition-metal oxides for the cathode are synthesized and processed into particles with sizes on the order of tens of micrometers. Afterwards the particles are combined with other additives, such as electronically conductive carbon black and a polymer binder, before being mixed with a solvent to form a slurry. The slurry is then casted on to metal current collectors; the resulting electrodes are typically in the 100 - 200 micrometer thickness range. After drying, these electrodes can be wound or stacked in a few different ways, depending on the cell format it will eventually become. Whether a cell is ultimately cylindrical or prismatic, its electrodes comprise many sandwiched layers of repeating current-collector/cathode/separator/anode/current-collector units. Figures 1.1a and 1.1b are modified images from patents depicting the winding and stacking configurations for different cells [4, 5]. While wound configurations can be made much faster than their stacked counterparts, electrodes in the stacked configuration are generally more consistent in their geometric characteristics. Each configuration has its own pros and cons, further discussion on which geometry is more appropriate for which application can be found in the works of Full *et al.* and Pesaran *et al.* [6, 7]. Anodes were colored yellow while cathodes were colored grey and separators were left as white. The jellyroll or stack is then placed inside a cylindrical or prismatic metallic case, or a soft pouch. The exterior casing isolates the active materials from air and moisture and serves double duty as a mechanical constraint that ensures good contact between all the layers. Detailed manufacturing steps for higher-level

configurations such as modules and packs can be found in the works of Ciez and Whitacre [8], Sakti *et al.* [9], and Wood *et al.* [10].



(a) **(b)**

Figure 1.1: Modified images from patents [4, 5] representing stacked electrode configuration (a) and flatwound jellyroll configuration (b) with relevant components colored and labeled for ease of identification.

1.3 Side processes through various length scales

1.3.1 Thermal response

During cell operation, lithium ions are transported back and forth between the positive and negative electrodes within individual layers of the cell. The processes by which lithium ions insert into and are removed from the crystal lattices of the active electrode materials are called intercalation and deintercalation, respectively. The relative amounts of lithium ions in each electrode determine the state of charge (SOC) of a battery. SOC is defined as a percentage, where 100% means the cell is fully charged and 0% means the cell is empty. In terms of lithiation states, 100% refers to a self-imposed lithiation limit where most of the lithium ions are in the anode, while 0% is the opposite. Both of these limits correlate to a cell voltage value that can be easily measured.

The intercalation/deintercalation process also generates or consumes heat. Because every component of a battery produces of electrical resistance, current flow through the cell interior leads to joule heating in any component it passes through.

Joule heating can arise from interfacial, electrical, or ionic resistance; it will always produce heat, regardless of the direction of the current and scales as I^2R, where I is the current and R is the resistance. There is also a reversible heat generation or consumption that can be associated with the flow of current. This owes to the entropy of reaction associated with the electrochemical intercalation/deintercalation reactions that occur in the electrodes. Unlike joule heating, entropic heat does depend on the direction of current [11, 12], and therefore can act as a heat source or a heat sink.

Another aspect of the thermal behavior that is worth noting is the significant nonuniformity of the temperature within large-format prismatic cells [13, 14]. This nonuniformity can severely limit the usage of the cell because temperature driven failure modes do not always require the whole battery to reach a certain temperature [15, 16]. Depending on the battery's ability to transfer heat to its surface and then dissipate to its surroundings, small regions can produce enough heat to drive catastrophic material failure at a particular location, which can spread through the cell and even to rest of the pack.

It is important to understand the way heat is generated and distributed during battery-cell operation, because high local temperatures can lead to catastrophic failures of the entire battery pack. For instance, 'thermal runaway' is a failure mechanism wherein exothermic side reactions are triggered when battery materials rise above a certain temperature [15]. This can occur from internal short circuits, overcharge, and many other mechanisms [17]. The evolved heat increases the rates of other exothermic processes and slows heat transfer to the battery exterior, thus creating a positive feedback loop. The consequent unbounded increase in temperature can ignite the volatile electrolytes within lithium-ion batteries, leading to fires or even explosions.

1.3.2 Mechanical response

It has been previously shown that changing SOC induces noticeable volume changes in the graphite negative electrodes; changes also occur in typical positive electrodes,

although to a lesser extent [18]. During the charge process, lithium ions from the cathode insert into the anode (graphite), so there is an expansion in the anode while there is a contraction in the cathode [19]. The opposite occurs during discharge. The strain felt by the electrode materials in response to the insertion and removal of lithium ions can affect the observed performance of the battery across all length scales, beginning at the electrode level and ending at the pack level [20–25]. This is because repetitive strain cycling can cause the materials to fatigue over time, eventually leading to fracture. The worst fractures quickly drive failure by causing electronic disconnects, which isolate the electrode material from the rest of the battery or trap useful lithium within its structure. Micrometer-scale dilation occurs in a single electrode [26, 27], so a stack configured battery could contain up to hundreds of these individual electrodes which results in larger stress/strain response[28, 29].

Even though the electrochemical reaction can cause the mechanical changes mentioned above, thermally induced mechanical changes can also occur. Typical operational loads can generate enough heat to raise surface temperatures of the cell significantly [30, 31]. Mechanical fatigue as the battery temperature swings from ambient to higher operational temperatures repeatedly could lead to a gradual mechanical degradation of active materials through repeated thermal expansion and contraction [30, 32]. This degradation mechanism also does not necessarily need to correlate with the extent of electrical cycling or operating power; for example, an end user might reside in an area where ambient temperature swings across a wide range throughout the day. Since vehicles are most often stationary, an automotive battery could experience many thermal cycles even without electrical cycling, creating new scenarios for failure due to the stress and strain history and is a research area that is worth exploring.

1.4 Characterization techniques

Several challenges make it difficult to study an operational battery cell holistically. The different electrical, thermal, and mechanical phenomena occur over and can

be coupled across multiple relevant length scales. Thus, studying how to isolate specific characteristics, and making sure that such isolated knowledge can be reassembled to understand the complete system, is important. Experimental design and interpretation are of particular importance when two phenomena cannot be decoupled in a particular operational mode of the battery. In recent years there have been many groups researching methods and developing techniques to characterize batteries and developing techniques to measure the resulting mechanical or thermal effects from an electrical load on top of the standard voltage and amperage measurements [14, 21, 22, 30, 33–40]. So, there is a wide variety of sensors available to measure physical signatures, e.g., temperature, stress, and, strain. And, if correlated through a carefully designed physical model, these external macroscale measurements can be used to infer properties on the microscale. In this section, the discussion will be centered upon the various types of measurements one can make, the techniques used to analyze the data, how useful parameters can be extracted from data, and how measurements and analysis can help to elucidate the health state of a battery.

1.4.1 Electrochemical Measurements

Depending on the input current signal, a lot of valuable information can be extracted from voltage measurements alone. Simply cycling a battery with a constant current (CC) input signal and looking at characteristic features of the voltage can give some insight into the battery's state. Depending on the cell chemistry, voltage can be loosely correlated to the SOC; and the length of time it takes for a cell to complete a cycle under consistent CC conditions yields a practical capacity that evolves over time and can be used to track state of health (SOH). The rate at which current is applied to charge/discharge a battery relative to its nominal capacity is known as the C-rate. C-rate measures charge or discharge rate in units of the total battery capacity per hour. For example, a battery that is fully charged from 0% to 100% SOC in 1 hour is charged at 1C; if the charging occurs over 30 minutes instead, the battery is charged at 2C. When cycling at a very slow C-rate, ohmic losses

are low, so pseudo-OCV (POCV) data can be generated. When cycling at a high C-rate, voltage losses are larger, allowing tests of power capability.

Given POCV charge/discharge data, differential voltage analysis (DVA) or incremental capacity analysis (ICA) can be used to observe features that are not as easily seen in the regular discharge voltage curve [41, 42]. This analysis involves differentiating the voltage with the amount of current passed (DVA) or *vice versa* (ICA). Phase changes in the material can be precisely located as peaks in the SOC differential. Seeing how the location of these peaks shift allows one to track how the health of the individual electrodes, and consequently, the battery as a whole [43–46]. We exploit this technique to quantify battery states in Chapter 2. Chapter 3 also briefly compares the conclusions that can be drawn using this technique with similar SOC differentials obtained by lock-in thermography.

The Galvanostatic Intermittent Titration Technique (GITT) involves pulse charging or discharging the cell and allowing the voltage to relax, then assigning the asymptotically attained value as the OCV that describes the present state of the battery. Although GITT is arguably the more accurate method of measuring OCV data [47], we will see that POCV usually suffices to generate a voltage curve as a function of SOC for the cells of interest here. It is worth noting that GITT takes an already long process and makes it even longer. POCV takes approximately one full day to complete one direction of a charge or discharge(C/25 rate), while GITT takes multiple hours per SOC titer (*i.e.* each additional input of charge). The granularity that is desired for SOC *vs.* voltage data causes the experimental time to add up. The upside of GITT is that it does offer some more information, such as providing a means to calculate diffusion parameters from the relaxation data [47–49]. Depending on the C-rate, the resulting voltage response to the GITT pulse current profile can also be used to calculate the cell's direct current internal resistance (DCIR) [50–52].

Electrochemical impedance spectroscopy (EIS) is done by applying an alternating current with a wide spectrum of different frequencies. This experimental technique allows for the measurement of properties such as bulk and charge transfer resistances

when looking at the resulting nyquist plot. In addition, properties such as exchange-current density and its corresponding activation energy can be extracted from EIS measurements repeated at various temperatures [47, 53].

The different parameters extracted from all these experiments are often required inputs for physics-based modelling. Some of them have strong temperature dependences, so in operational scenarios where the batteries are highly stressed (*e.g.*, fast charging, fast acceleration, *etc.*), cell temperatures can significantly increase and change their behavior. Therefore, it is important to collect temperature data in addition to standard voltage and current data.

1.4.2 Thermal measurements

In prior work [30, 54], thermocouples have been used to measure local surface temperature on cycling battery cells. Temperature distributions for large-format lithium-ion batteries were captured using an array of thermocouples. In automotive applications cell sizes are generally increasing over time; cells that have large characteristic dimensions (being distictly long or wide) may sustain nonuniform temperature distributions due to tab sizing and orientation with respect to the shape of the electrode. Determining the locations where temperature reaches its greatest extremes will be key to safety and health monitoring. Thermocouples give off a voltage that is temperature dependent and is converted into a temperature value. They are relatively inexpensive and are easily implemented by adhesion to the object of interest. Since thermocouples are used in many applications, they have standardized connections, making them quick to get set up and running. Some issues with thermocouples for this area of research is that higher spatial resolutions require greater numbers of sensors, all of which need to be properly calibrated and attached with tape; this effectively insulates the battery surface.

Figure 1.2a shows the nonuniformity that was previously mentioned in the surface temperature of the battery. For reference, the active-material area is 200 mm tall and 150 mm wide. The cell surface is significantly hotter near the tabs (near the top) of the battery, while the areas further away are cooler. This characteristic

of the temperature distribution owes in part to the tab placement within the battery. Figure 1.2b schematically shows current streamlines within the tabs and the cell; the current prefers to take the path of least resistance, so most of the current will always travel the shortest path between the two tabs until there are no lithium ions available for intercalation/deintercalation in that localized area. This preliminary experiment confirmed that there is indeed a considerable 2D temperature distribution across the cell surface and served as a first step towards the development of the lock-in thermography experiments that will be described in Chapter 2.

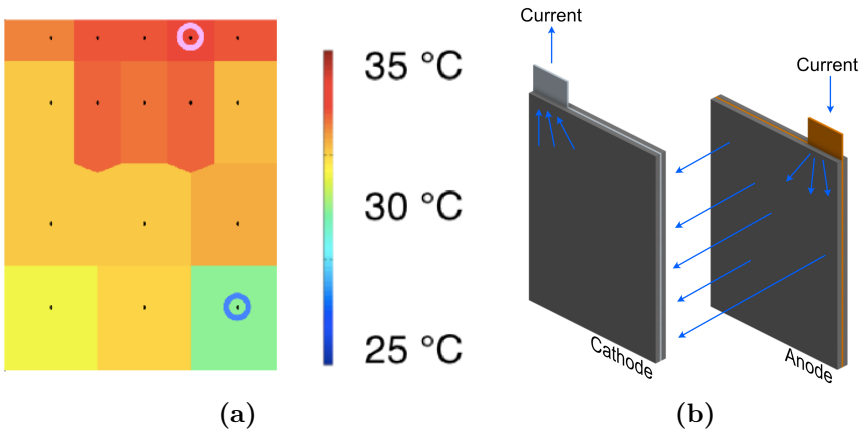


Figure 1.2: Temperature distribution of A123 15 Ah battery measured using an array of thermocouples [54] (a) and schematic depicting current path inside of large-format pouch cells (b).

Various experiments can be done to determine thermal material properties such as heat capacity and thermal conductivity. Thermal characterization experiments are usually decoupled from electrochemical effects by keeping the cell electrically isolated while heating or cooling by external means, for example, using heat lamps, calorimeters, or environmental chambers [35, 55–57].

There are, however, methods that involve some coupling, wherein a thermal response is induced as a result of an applied current signal [13, 34]. Fleckenstein *et al.*[34] developed an equivalent circuit type model to represent thermal phenomena. Using a technique analogous to EIS called thermal spectroscopy, they extracted a heat capacity and a radial thermal conductivity for a cylindrical Li-ion cell. Much like EIS, sinusoidal current waveforms were applied to a cylindrical-format cell;

temperatures were measured using thermocouples on opposite sides of the surface. Robinson *et al.* [13] used an infrared (IR) camera to record surface-temperature distributions in pouch cells under a sinusoidal current with a single frequency. They showed that this process allowed for fast identification of defects, which were revealed by the phase lag in local temperature variation.

1.4.3 Mechanical Measurements

The fundamental sources of volume expansion are SOC-related dilation in the active particles and thermal expansion; once electrodes have been stacked or wound, a cell has been assembled, and a cell string has been placed in a module or a pack, there are many additional sources of mechanical constraints. Therefore, stress measurements have been previously explored on multiple scales, and have successfully been used at the cell level to better approximate SOC [21, 22]. In these works, prismatic cells were put under a preloaded stress similar to what they would experience in a practical module, by being compressed between endplates connected to a force sensor. This rig aggregates the entire cell's stress evolution into a single value (the readout of the force sensor) that is easily tracked. Compared to a voltage signal, stress undergoes a noticeable and steady change across the cell's entire SOC range, making it a potentially useful gauge for SOC to complement OCV estimation.

Alternatively, if a cell is allowed to freely swell and contract, strain can be measured with linear variable differential transformer (LVDT) sensors [28, 30, 32, 58]. In the cases of Schiffer and Mohtat and their respective colleagues, a single LVDT sensor was used on top of an endplate that can freely move, once again aggregating the entire pouch cell's behavior into a single measurement. Although one could argue that the weight of the endplate does introduce a compressive force, effectively converting some of the strain effects into stress. If that is ignored, this research has shown that strain measurements, provide improved ability to estimate the state of the battery [28, 58].

Oh *et al.* [30] conducted experiments measuring localized strain at various locations across a prismatic cell by implementing a three-by-three array of these

sensors and contacting it to the front and back surfaces of their prismatic battery. A thermocouple was also attached to an area near the center of the battery (so as not to interfere with the displacement sensor), to track cell surface temperature. Besides Oh and his colleagues, the mentioned research [21, 22, 28, 32, 58] operates in a control space where thermal effects are expected to be negligible (low C-rates). Oh *et al.*, by contrast, were able to show the interplay between all three mechanisms, by studying strain and temperature evolution as a function of C-rate. When cycling at elevated C-rates, the strain was irreversible until the current was off and left alone for a period of time. This length of time correlated with the time it took for the cell to fall back to the ambient temperature. Thus, although stress/strain measurements can be insightful, they appear to be prone to being convoluted with temperature effects. Oh *et al.* also showed that the experimental array displayed significant differences in the measured strain signal at different locations of the battery, which could arise from both the nonuniform current distribution and the cell geometry. Prismatic cells introduce another source of convolution from the auxiliary components in the battery, such as bus bars, and the harder metallic casing.

Much like the thermocouples mentioned in the previous subsection, these LVDT sensors clog up the surface area available to make measurements, setting an upper limit on the spatial resolution. Rieger *et al.* in turn has implemented 3D and laser profile scanners to try to get a better look at the nonuniform strain distribution in pouch cells [29, 59]. Using similar low-rate cycling protocols, they were able to get high spatial resolution. Using their technique to determine that areas of the pouch cell that were closer to the tabs experience a larger change in volume compared to locations further away. Concluding that laser scanning with a profiler is another method of doing dilatometric experiments on smaller sized pouch cells.

1.5 Summary

We provided a survey of various non-destructive testing techniques useful to characterize and diagnose batteries, which rely on external measurements such as voltage, temperature, and stress/strain. It is worth noting that nonuniform

distributions of current, temperature, and stress/strain at the material and cell levels also propagate up to larger length scales. The tabs on an individual cell dictate how the current is distributed, the way the connections are made within a module in a pack also affects how much current is delivered to each cell comprising it. A few groups have shown that highly connected cells in series and parallel with a common tab orientation design will cause nonuniform current distributions within large battery packs [60, 61]. Small differences in impedance across the many cells in a module or pack, the location of the cell itself within the module or pack, and quality control in the connections between cells, are all factors that will affect how current flows through the packs, the modules within the pack, and the cells within the modules. In these situations, cells closest to the connection points of the module/pack experience the highest amounts of current throughput and therefore the highest amount of degradation, while the least used cells regularly experience as little as half.

More detailed non-invasive characterization needs to be conducted for individual cells to establish what type of second life application (if any) they are good for, or if they should just be scrapped and recycled altogether. A more detailed characterization can also aid in areas such as cell design, where the ability to extract effective properties can guide changes in manufacturing to tune these material characteristics. If the techniques are simple to implement and fast enough, they can also be used for quality assessments for cells.

This thesis will describe new techniques that can be used to characterize battery state at the materials level. In Chapter 2, the lock-in thermography technique is explored to supplement the qualitative conclusions one can draw from nonuniform surface-temperature maps by introducing a quantitative analysis. A minimal parameter set that effectively describes the battery system was determined by boiling down the 2D data into a few characteristic features that we wish to simulate. Once this minimal parameter set is determined, the capability in predicting temperature behaviors of large-format pouch cells will be assessed.

Chapter 3 aims to use the inverse modelling approach from the previous chapter to fingerprint the health state of pouch cells following a specific degradation process. By determining the parameter sets that describes the battery at known SOHs, it may be possible to infer the history of a cell with a less detailed history. This chapter will attempt to answer the question of whether or not the model and experiments are sensitive enough to depict the changes in the battery as modified parameter values and what these changes could mean for the battery. Many of the techniques used to determine material property values allow for one to two values to be obtained per experiment and are often destructive. This approach allows for a few more values to be obtained using a single experiment with a physics-based model.

And although the mechanical mechanisms are highly coupled to the electrochemical and thermal phenomena, work so far has tried to decouple them by minimizing thermal effects through experimental design. Therefore we develop a preliminary experimental setup in Chapter 4 that can be used to measure both temperature and strain in tandem under high current loads. The objective is to see if by capturing both volume and temperature change simultaneously, would it be possible to differentiate between the SOC induced volume change from the thermally induced volume change? And if it is possible to differentiate the two, is it possible to determine which effect dominates, and under which conditions?

2

Electrochemical/Thermal Characterization and Modeling

2.1 Introduction

Owing to their large energy densities and low packaging cost, large-format prismatic Li-ion cells are becoming ubiquitous. Among large-format cells, prismatic pouch cells are one of the most widely used types. One might think that thermal management would be easier for cells with large open surfaces that can be contacted to heatsinks, but several researchers have reported that the temperature distributions across prismatic cells can be significantly nonuniform, which can severely impact their performance [62–66]. Figure 2.1 presents infrared thermography images of 20 Ah prismatic pouch cells that exhibit such nonuniformity, with higher temperatures near the tabs. Even if such 'hot spots' do not cause catastrophic cell failure, inhomogeneities in temperature during cycling lead to a nonuniform thermal history within a battery, which may affect its cycle life [67, 68]. Thus, accurate health and performance models require detailed understanding of how cell materials and chemistry impact temperature distributions.

When performing electrochemical/thermal modeling, one must consider the possible coupling of heat and charge transport. The approach to modeling heat

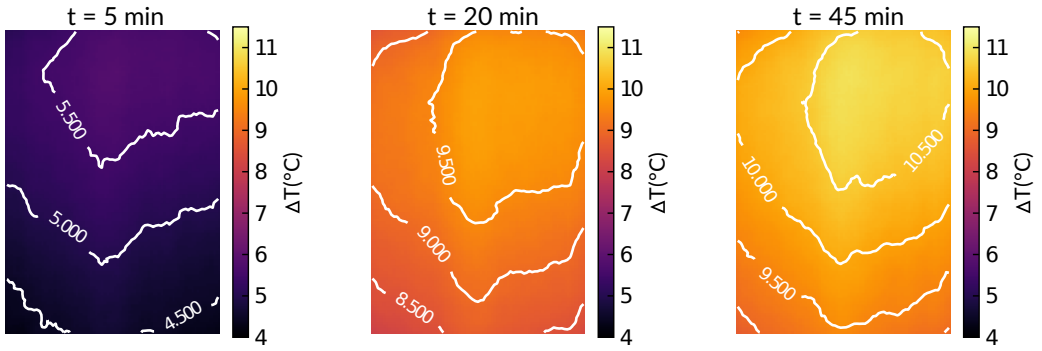


Figure 2.1: Three infrared images ($\Delta T = T - T_\infty$) of the surface of a 20 Ah lithium-ion battery cell, under 4C charge-discharge cycling with 100 s period, freely hanging in stagnant air with $T_\infty = 25°\text{C}$. To illustrate how surface temperature develops, the images show the temperature of an initially isothermal battery after (left) 5 min, (center) 20 min, and (right) 45 min of continuous cycling.

transfer is common across groups, but there are two distinct philosophies of charge-transport modeling: equivalent circuit modeling (ECM) [69–73] and physics-based electrochemical mass-transport modeling [38, 74–86]. Both methods describe the terminal-voltage responses of Li-ion battery cells quite accurately, but their levels of detail regarding the material properties of cell constituents differ significantly. Since battery temperature impacts phenomena like mechanical fatigue, side reactions, and other factors associated with aging, it is worthwhile to develop electrothermal models that incorporate material properties. On the other hand, it is desirable to work with simulations that keep computational complexity at a minimum, both to increase the utility of models for battery-management applications and to facilitate iterative model-parameterization schemes.

Fleckenstein et al. modeled a battery cell as an aggregate of volume elements through which charge transport is described by equivalent circuits, coupling these to a general energy balance that accounts for local heat accumulation, conduction, and generation [87]. The charge balance communicates irreversible joule heating and reversible (entropic) reaction heat into the local thermal-energy balance. Because both of these terms depend upon the amount of current being passed, the charge balance can thermally contribute to the calculation of temperature of each volume element in their simulation. Also, the thermal model in principle communicates

back to the equivalent circuits, through functions that establish the temperature dependences of resistances and capacitances. Although it was found to match experimental temperature-distribution data effectively for a 32113-type 4.4 Ah $LiFePO_4$ (LFP cathode) battery, the model of Fleckenstein et al. has the same limitations as other ECMs: it is not clear how the resistances and capacitances involved in the equivalent circuits relate to the physical properties of materials and interfaces within the cell.

Electrochemical mass-transport models [38, 74–81] have also been used to underpin thermoelectrochemical simulations. The now-standard Dualfoil scheme developed by Fuller, Doyle, and Newman is the most commonly used mechanistically based electrochemical model [75–77]. Dualfoil augments the Newman–Tobias porous-electrode theory [80] by accounting for concentration polarization in the separator, pore-filling electrolyte, and solid intercalation media. The original form of Dualfoil combined porous-electrode theory, concentrated-solution theory, and solid-phase intercalation dynamics.

Bernardi et al. explored the thermal management problem, under the assumption that the temperature within a cell is locally uniform [88]. Srinivasan and Wang [81] provided the most complete coupling of Dualfoil to a local heat balance. They solved the electrochemical and thermal model equations simultaneously by discretizing the partial differential equations involved and using an implicit linear multistep solution method. Prada et al. developed a pseudo-two-dimensional thermoelectrochemical model for LFP cells [85]. A simplified electro-chemical model (modified single-particle model) was coupled to Forgez et al.'s analytical solution of the temperature distribution in the cylindrical system [89] to reduce computational costs.

In 2013, Christensen et al. suggested a new approach to three dimensional thermoelectrochemical modeling, which was applied to 18650 Nickel Manganese Cobalt Oxide (NMC) lithium-ion cells [74] and larger 50 Ah automotive lithium-ion batteries [38]. Under an assumption that Soret/Dufour diffusion is negligible, the thermal and electrochemical models can be partially decoupled, allowing the electrochemical and thermal problems to be solved sequentially at a given timestep.

This approach permits the battery interior to be described with two different spatial meshes, with differing mesh spacings appropriate to the electrochemical and thermal problems. In order to decrease computation time, sparser meshing was adopted for the electrochemical description.

This chapter aims to describe the nonuniform thermal response of large-format prismatic LFP pouch cells using a microscopic electrothermal model that has computational efficiency comparable to an ECM, while still retaining some of the insight about material properties that Dualfoil provides. This objective is achieved by describing mass and charge transport within the battery through a simpler perspective provided by the original Newman–Tobias porous-electrode theory, while describing heat transfer through the more detailed perspectives of Srinivasan and Wang or Christensen *et al.* [74, 81].

The streamlined model put forward here can be solved relatively quickly with the COMSOL finite-element package, which enables multi-objective parameterization schemes based on direct processing of spatially resolved experimental lock-in thermography data. The complete electrochemical/thermal simulation is run iteratively to target parameters that minimize the difference between model predictions and experimental data describing the dynamic cell voltages and surface-temperature distributions of large-format prismatic LFP pouch cells. Although the proposed model is much simpler than Dualfoil, we find that it suffices to match the minimum, maximum, and surface-average temperatures during short-period charge/discharge experiments, as well as matching the dynamic output voltage of the cell. Finally, the parameters yielded by the optimization scheme can be analyzed to provide insight into the microscopic physics that controls the battery's electrochemical and thermal response.

2.2 Design of experiments

2.2.1 Experimental Apparatus Design

There are several ways to measure surface temperature distributions. A natural approach is to attach an array of thermocouples across the battery in a regular

pattern. The main drawback of this method is that the thermocouple array effectively insulates the battery thermally as the number of thermocouples increases. Robinson *et al.* introduced the use of lock-in infrared thermography on lithium-ion batteries as a non-invasive technique to qualitatively identify defects and faults within a battery [13]. The thermography measurements in that work were performed using a camera mounted above a cell that laid flat across a solid surface, e.g., table, bench top, *etc.* This large area of thermal contact with the table affects thermal boundary conditions in unpredictable ways.

To avoid thermal feedback between the measurement apparatus and the device being measured, we designed an apparatus to hold batteries without impeding their ability to dissipate heat by natural convection. Acrylic sheets (McMaster Carr/RS Components: 6 mm thick) were laser cut into frames to hold the battery. A few extra pieces were then acetone welded to the frame to serve as an overhang to support the battery from below, mitigating the stress that could arise from hanging the battery by its tabs. An additional piece was then cut and welded to the top part of the frame as an extra safety precaution. This piece prevents physical contact between positive and negative connections, which would short circuit the battery. The dimensions of the frame and the cutouts are shown in Figure 2.2. Even though 6 mm thick acrylic was used, other thicknesses could be used so long as they maintain structural integrity.

Traditionally, alligator clips have been used to make electrical connections for thermography experiments, but this was found to create substantial contact resistance, leading to the generation of extraneous heat in the tabs that led to systematic experimental error and some irreproducibility. It is also possible to avoid the contact resistance of alligator clips by cutting holes in the battery tabs and securing electrical connections with nuts and bolts. However, this permanently changes the tab geometry and can make operating temperature higher by reducing the amount of conductive tab materials. Techniques developed for second life assessment should prioritize preserving the tabs in the best condition possible, which removes hole punching as a viable option.

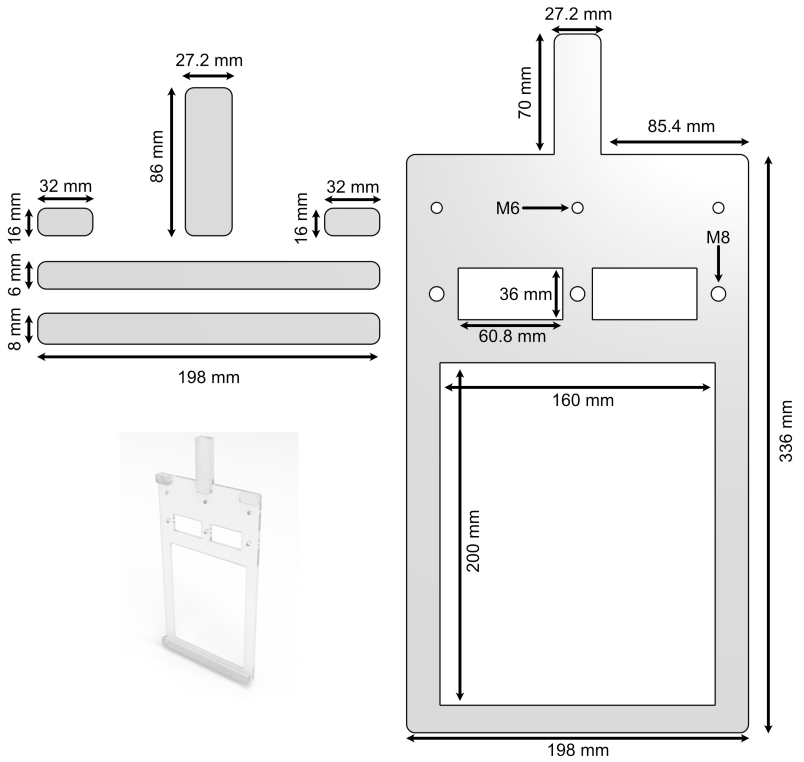


Figure 2.2: Acrylic frame drawing with render for use with A123 20 Ah pouch cells

The battery tabs were left pristine and connected to the power supply *via* contacting copper bars (McMaster-Carr super-conductive 101 copper bars). These bars contained holes that allowed the potentiostat leads to be connected with nuts, bolts, and ring terminals. The battery tabs were pressed against the opposite ends of the copper bars and held in place with silicone rubber (McMaster-Carr high-temperature silicone rubber). Machined nylon sheets (McMaster-Carr nylon grade 6) were used to enclose both the copper bars and the silicone rubber, because they are good electrical insulators and safe to use over a large range of temperatures. The front plate was cut, and two slots were hollowed out so that the copper bars could be press fitted into each slot. The back plate was cut and then the silicone rubber pads were glued to it. Holes were drilled out and all these parts were secured with nuts and bolts. The dimensions of these components are highlighted in Figure 2.3. These components were then aligned through the holes with a long bolt and secured with a nut.

Finally, the cell holders were designed to maintain uniform natural convection

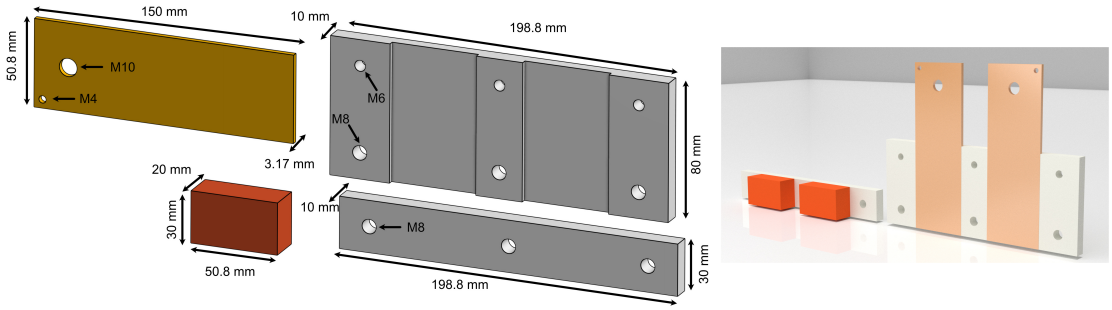


Figure 2.3: Nylon front and back plates for electrical connections to A123 20 Ah pouch cells. The part on the left in the render depicts the nylon piece with the silicone rubber pads glued in and the part on the right is the front plate that houses the press fitted copper bars.

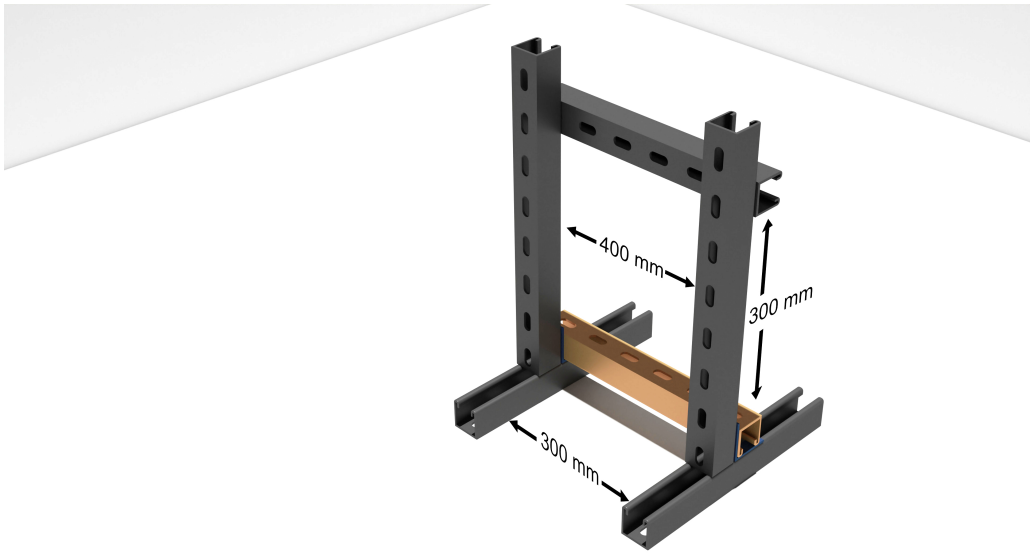


Figure 2.4: Free standing unistrut frame for supporting the cell holders. Labeled measurements refer to the length of the piece of unistrut. The bronze colored beam is used to prevent the uprights from being askew.

by holding the cell vertically. A frame was built using unistrut framing. Pieces were assembled into a free-standing structure using bolts and channel nuts. The lengths of individual pieces are labeled in Figure 2.4. Figure 2.6a shows a photograph of the assembled rig containing the metal frame, nylon plates, and the acrylic frame.

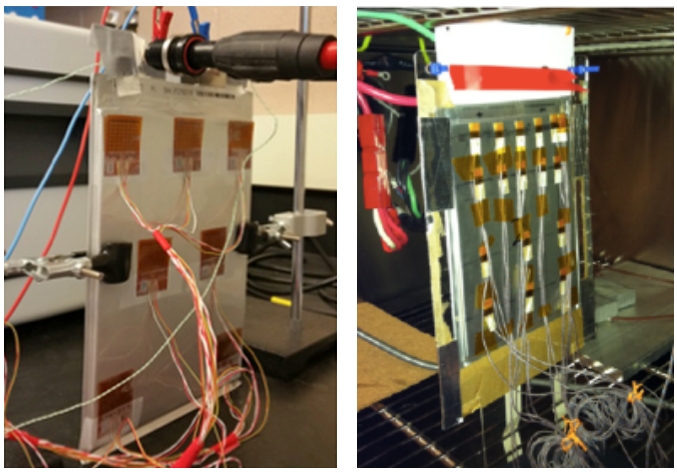
2.2.2 Input Signal

Several of the fundamental properties of a battery depend on its state of charge (SOC) [11, 12, 57, 90–92]. Therefore, a control scheme involving short-duration

charges and discharges with fixed periodicity around a given SOC was introduced to allow the study of rate and temperature effects without inducing significant changes in the volume-averaged thermodynamic state. Squarewave excitation tests with variable wave amplitude A and period p were performed around various average SOCs, such as 30%, 50%, and 70%. The open circuit potential (OCP) of the A123 battery used for experiments exhibits a plateau (or linear characteristics with very small gradient) with respect to charge state, further supporting the relative constancy of thermodynamic properties. After determining the SOC swing induced by the input signal, the initial battery SOC was offset in such a way that the average state during the excitation centered around the SOC of choice. For example, for the $A = 4$C and $p = 100$ s squarewave, the charge portion of the signal increases the SOC by 5.56%. To keep the mean SOC at 30% during the cycling, the battery was initially equilibrated at an SOC of 30-5.56/2 = 27.22%. To set its initial state, the cell was charged with a constant current, constant voltage (CCCV) protocol until fully charged (3.6 V until the current decayed to C/100), and then discharged to the desired charge state by coulomb counting, using the manufacturer-specified 20 Ah as the assumed charge capacity. The cell was then left to rest for 2-3 hours until both voltage and surface temperature had equilibrated before starting the thermography experiments.

2.2.3 Infrared Thermography

While the battery was subjected to AC excitations, surface-temperature profiles were measured with a FLIR A35sc infrared (IR) camera. Infrared cameras operate much like regular cameras except, instead of detecting visible light, it detects infrared waves. An IR sensor detects infrared waves and then converts the data into images called thermograms. Although many of its applications are used in the military, it is a technology that has been developed to be useful in other areas such as product quality assurance and fault detection [93]. It is most often used in testing electronics as heat is a contributor to the stresses that parts can endure while in operation, and can have a strong thermal response moments before failure[94].



(a) (b)

Figure 2.5: Examples of thermocouple arrays from the works of Mastali *et al.* and Kim[54, 95]

The tests were performed on 20 Ah LFP pouch cells from A123 Inc. Figure 2.6c shows the IR camera setup: the camera was placed sufficiently far from the battery to be at a distance greater than the minimum focal distance, and also far enough so that auxiliary components (copper bars and ambient spot) were within frame – in practice, this distance was about 0.75 m. Krylon ultra-flat black paint was applied to the battery surface to establish a uniform emissivity of 0.95 – 0.97. It is worth mentioning that in order to ensure good contact between thermocouples and the battery surface, a layer of aluminum or copper tape is applied and then a layer of kapton tape. The wires of the thermocouples will also be draping down from the higher regions of these large-format cells as shown in Figure 2.5, which can also impede heat from dissipating into the environment from the surface. Because of the long focal length of the camera lens, thermography experiments could not be performed inside a temperature-controlled chamber. Instead, the experiments were conducted in an isolated room with stable ambient temperature controlled by exterior air conditioning. All data sets from this study had ambient temperature readings that never exceeded 2 °C worth of change during the course of the 50 minute experiments.

The use of black paint was supported by a comparative squarewave experiment

with an unpainted battery in Section 3.2.2. In this experiment, the reflective nature of the pouch material led to interference, showing an image of reflected heat from the IR camera in the thermograms. Practically, one could circumvent this issue by orienting the camera at an oblique angle to the battery surface, but this induces a need for image processing to perform a perspective transformation of images. It should be noted that aside from the reflected image of the camera in the thermograms, the characteristic data sets for hot spot, average, and cold spot temperatures were effectively the same for painted and unpainted cells.



(a) **(b)** **(c)**

Figure 2.6: (a) Assembled battery holder with prismatic cell and (b) FLIR A35sc camera. (c) Completed experimental setup.

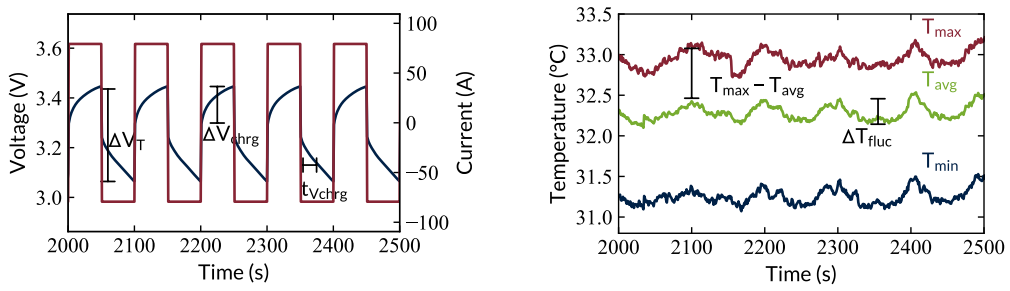
An ambient spot, comprising a piece of black felt held up by a type T thermocouple, was used to help mitigate errors associated with IR thermography. IR cameras measure relative temperature very precisely (sensitive to changes as small as 50 mK), but are susceptible to larger errors in absolute temperature ($\pm$ 5 °C or $\pm$ 5% of reading). The felt square used as the ambient spot is visible on the right of the battery cell in Figure 2.6a and Figure 2.6c. All reported IR temperature data was post-processed by taking the average temperature of the region of interest and subtracting the surface-average temperature of the ambient spot, to reduce noise and remove artificial temperature jumps caused by the IR sensor recalibrating due to the sensor temperature. At the outset of every experiment, the absolute

temperature read out by the thermocouple was calibrated against a thermometer (Fisher Scientific General Purpose Liquid-in-Glass thermometer) with an accuracy of ±3 °C. This temperature was added back to the relative temperatures measured by IR thermography to establish the absolute temperature across the battery surface.

The rightmost image of Figure 2.1 shows a representative temperature measurement from the IR camera after 45 minutes of squarewave excitation with $A = 4$C and $p = 100$ s (abbreviated as 4c100s). One would expect irreversible joule heating during the excitation; the squarewave excitation was chosen because it keeps the rate of joule heating constant when compared to a sinusoid. Power scales as I^2R, and I has the same magnitude despite its switch in sign. Any oscillations in temperature in the periodic steady state can therefore be more readily attributed to reversible heating. The surface temperature is nonuniform during the excitation tests; thus additional factors contribute to the thermal response of these prismatic cells.

Typical transient voltage and temperature data in response to a squarewave excitation are shown in Figure 2.7. The cell responses were characterized by observing several key features of the voltage and temperature profiles once the system reached a periodic steady-state; these features are labeled in Figure 2.7 as well. The alternating electric current generates a corresponding output voltage which has a maximum variation ΔV_{T}. Unlike the input current, the output-voltage profile does not follow a squarewave, but exhibits transient relaxations; the transients are described by tracing the magnitude of the voltage increase during the charge step, ΔV_{chrg}, and the voltage relaxation's characteristic time constant, $t_{V_{\mathrm{chrg}}}$. This relaxation is thought to arise from slow diffusion, but this effect can actually be accounted for by the capacitance induced by the change in OCV with respect to SOC. However we will later see that even though this is not an effect of solid diffusion, one of the shortcomings of the model can be explained if it was included.. The value of $t_{V_{\mathrm{chrg}}}$ is identified by finding the time after the step begins when the voltage has relaxed across 50% of ΔV_{chrg}.

Figure 2.7b shows the evolution of minimum, maximum, and surface temperatures on the battery surface in the periodic steady state. Thermal oscillations



(a) (b)

Figure 2.7: General (a) electrical and (b) thermal responses to AC squarewave current. Characteristic features used for sensitivity testing of the thermoelectrochemical model are labeled on the figures.

are observed, implying that heat absorption occurs at some points as the SOC swings. Such behavior is ascribed to the reversible heat – that is, the entropy – of the cell reaction, which can act as a heat source or sink depending on the sign of the current and the SOC. The maximum temperature fluctuation in the periodic steady state, ΔT_{fluc}, is also noted as a characteristic feature and used for parameterization. Reaction entropy has been quantified for a number of battery systems and electrode materials [11, 12, 15, 91, 96]. The nonuniformity of the temperature profile is quantified by taking the difference between the maximum temperature and the surface average temperature, $T_{\max} - T_{\text{avg}}$.

2.3 Modeling

2.3.1 Newman–Tobias Porous Electrode Theory

The Newman–Tobias model [80] is a simplified version of the now more popular Dualfoil [75]. It neglects concentration polarization in the separator, the porous solid, and the electrolyte in the pores, describing charge transport from a purely electrical standpoint. A 'macrohomogeneous approach' is taken, in which the microscopic geometry of porous materials is described by a local porosity ϵ and surface-to-volume ratio a_V. Newman and Tobias originally analyzed the steady-state current, potential, and reaction distributions in planar porous electrodes with both linear and Tafel interfacial kinetics under isothermal conditions [80]. They

identified a few key dimensionless parameters that govern the charge distribution and reaction distribution within porous electrodes. The Newman–Tobias model is computationally much more efficient than Dualfoil, and, when coupled to an energy balance, provides enough parameters to match all of the characteristics of the responses labeled in Figure 2.7, despite the neglect of concentration polarization. Each volume element of the electrodes comprises two phases that allow charge transport — electrically conductive solid and ionically conductive liquid — which also permit charge exchange through local interfacial reactions. Dynamic charge balances on the solid and liquid phases, which are designated with subscripts sol and liq, respectively, take the form

$$\vec{\nabla} \cdot \vec{i}_{\text{sol}} = -a_V i_{\text{k}} \tag{2.1}$$

$$\vec{\nabla} \cdot \vec{i}_{\text{liq}} = a_V i_{\text{k}} \tag{2.2}$$

Note that overall charge conservation within each volume element implies that the sum of these currents is solenoidal, $\vec{\nabla} \cdot (\vec{i}_{\text{sol}} + \vec{i}_{\text{liq}}) = 0$. The generation terms in Equation 2.1 and Equation 2.2 account for the kinetic current i_{k}, which expresses the charge flux across the liquid/solid interface within a volume element due to electrochemical reactions. Generally, the bulk-liquid and solid current densities $\vec{i}_{\text{liq}}$ and $\vec{i}_{\text{sol}}$ are positive when anodic; positive current associated with interfacial charge exchange, i_{k}, flows into the solid from the electrolyte.

Since the LFP chemistry has been observed to exhibit relatively high exchange-current densities, the kinetic current was described using linear kinetics, as

$$\rho_{\text{k}} i_{\text{k}} = a_V(\Phi_{\text{sol}} - \Phi_{\text{liq}} - U), \tag{2.3}$$

in which a_V is the surface-area-to-volume ratio, Φ_{sol} and Φ_{liq} are the potentials in the solid and electrolyte phases, U is the open-circuit potential (OCP), and ρ_k is the kinetic resistivity. Here the kinetic resistivity relates to the interfacial exchange-current density i_0 through

$$\frac{1}{\rho_{\text{k}}} = \frac{i_0 nF}{a_V RT} \tag{2.4}$$

where n is the number of charges involved in the half reaction, F is Faraday's constant, R is the gas constant, and T is the absolute temperature. Note that Equation 2.4 illustrates an explicit first-order dependence on inverse temperature, but the exchange-current density also generally is observed to have an Arrhenius temperature dependence. It is worth noting that nonlinear (Butler–Volmer) current-voltage relations were tried in place of Equation 2.3, but did not make a substantial impact on simulation results [97]; the linear form was therefore retained because it made convergence of the model faster.

During the squarewave excitation tests, the period and amplitude of the signal were chosen such that the overall charge state did not vary more than a few percent. Owing to the small variation, one can assume that the perturbation in SOC induced by the input signal induces a more or less linear response in equilibrium potential, so that

$$U = U_0 + k_U q + V_{\text{hys}} \cdot \text{sgn}(i_{\text{k}}). \tag{2.5}$$

This can be justified by looking at the range of charge states that these experiments traverse through in the POCV data in Figure 2.8. Here q is the local SOC in the volume element; k_U expresses the gradient of the OCP with respect to SOC at the average SOC, and U_0 is the OCP at the average SOC. Note that the assumption of a linearized equilibrium-voltage response is justified on a global level, but may lead to some errors on a local level, because some domains of the electrode may experience much wider swings in SOC than others. This issue did not appear to impact the effectiveness of the parameterization substantially, however.

The LFP chemistry is also known to exhibit equilibrium-voltage hysteresis. Depending on how the battery has reached a certain SOC (*via* charge or discharge), the corresponding voltage may differ. Figure 2.8 presents pseudo-OCP data for the A123 20 Ah LFP battery, obtained by charging and discharging at a C-rate of C/25. In the range of SOC that we are presently concerned with, the two curves are offset from each other by a fixed amount (the inset in Figure 2.8 shows a zoomed in view of the relevant region for these thermography experiments). The offset

in charge and discharge in this region is 0.04 V. To account for this in a simple manner, the offset was split evenly; 0.02 V is added to the OCP during charge and 0.02 V is subtracted from the OCP during discharge. This is represented by the $V_{\text{hys}} \cdot \text{sgn}(i_{\text{k}})$ term of Equation 2.5.

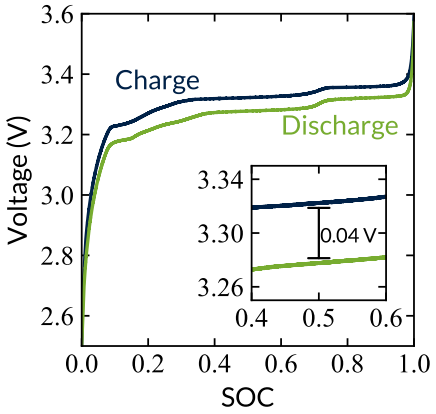


Figure 2.8: Pseudo-OCP curves for A123 20 Ah cell at 25 °C, generated by galvanostatic cycling at C/25

The local SOC q on which U depends is dimensionless, and is bounded between 0 and 1. It relates to the local kinetic current i_{k} and the maximum capacity density of the electrode Q_{max} through

$$\frac{\partial q}{\partial t} = \frac{a_V i_{\text{k}}}{Q_{\text{max}}} \tag{2.6}$$

Finally, following Newman and Tobias, Ohm's law is adopted in each phase to relate the local current densities to the gradients of potential,

$$\vec{\nabla}\Phi_{\text{sol}} = -\rho_{\text{sol}}\vec{i}_{\text{sol}}, \tag{2.7}$$

$$\vec{\nabla}\Phi_{\text{liq}} = -\rho_{\text{liq}}\vec{i}_{\text{liq}}, \tag{2.8}$$

where ρ_i is the resistivity of phase i. Equations 2.1 to 2.8 comprise a general statement of the model used to describe electrode domains in this work. The overall computational cost is much lower than models that include mass diffusion effects, allowing iterative 3-D simulations to be implemented for model parameterization.

2.3.2 General Energy Balance

Both the Newman–Tobias model and the Dualfoil model operate under isothermal conditions. So, a local energy balance was coupled to electrical governing Equations 2.1 to 2.8. The general form of this balance for a single, stationary, isobaric, multicomponent phase is [98]

$$C_{p,\text{eff}}\frac{\partial T}{\partial t} = -\vec{\nabla}\cdot\left(-k_{\text{eff}}\vec{\nabla}T + \sum_i \bar{H}_i\vec{J}_i + \vec{q}^{(x)}\right) + \sum_i \bar{H}_i(\vec{\nabla}\cdot\vec{J}_i - R_i), \tag{2.9}$$

where $C_{p,\text{eff}}$ is the volumetric constant-pressure heat capacity, k_{eff} is the thermal conductivity, and $\vec{q}^{(x)}$ is the Dufour energy flux density; $\overline{H_i}$, $\vec{J}_i$, and R_i are the partial molar enthalpy, molar flux density relative to the mass-average velocity, and homogeneous generation rate of species i, respectively.

Neglecting the Dufour flux [11, 12, 91] and applying the thermodynamic definition of the partial molar enthalpy through:

$\sum_i \bar{H}_i R_i$	Partial molar enthalpy of species i $\bar{H}_i = \mu_i + T\bar{S}_i [=] \frac{\mathrm{J}}{\mathrm{mol}}$
$\downarrow$	
$= \sum_i \left(\mu_i + T\bar{S}_i\right) R_i$	Production rate of species i $R_i = s_i r [=] \frac{\mathrm{mol}}{\mathrm{m}^3 \cdot \mathrm{s}}$
$\downarrow$	
$= r \sum_i \left(s_i \mu_i + T s_i \bar{S}_i\right)$	Total reaction rate $r = \frac{a_V i_k}{nF} [=] \frac{1}{\mathrm{m}^3 \cdot \mathrm{s}}$
$\downarrow$	
$= \frac{a_V i_k}{nF} \sum_i s_i \mu_i + T \frac{a_V \sum_i s_i \bar{S}_i}{nF} i_k$	Overpotential $\eta_s = \frac{1}{nF} \sum_i s_i \mu_i = \Phi_l - \Phi_s [=]$ V
$\downarrow$	
$= -\eta_s a_V i_k + T \frac{a_V \sum_i s_i \bar{S}_i}{nF} i_k$	Partial molar entropy change of reaction $\Delta \bar{S}_{\mathrm{rxn}} = \sum_i s_i \bar{S}_i [=] \frac{\mathrm{J}}{\mathrm{mol} \cdot \mathrm{K}}$
$\downarrow$	
$= -\eta_s a_V i_k + \frac{a_V T \Delta \bar{S}_{\mathrm{rxn}}}{nF} i_k$	Local reaction rate at interface $i_k = \frac{i_0 nF}{RT} \eta_s [=] \frac{\mathrm{A}}{\mathrm{m}^2}$
$\downarrow$	
$= -\frac{a_V RT}{i_0 nF} i_k^2 + \frac{a_V T \Delta \bar{S}_{\mathrm{rxn}}}{nF} i_k$	Irreversible + Reversible heating terms

In this derivation, the partial molar enthalpy term from the general energy balance was transformed into expressions that were more experimentally relevant, specifically in terms of the kinetic current because i_k is related to the rate of the electrochemical reaction. Legendre transformations were used to start off the derivation. Followed by assuming a linear relationship between the kinetic current and overpotential. And finally recognizing that $\sum_i s_i \bar{S}_i$ is equal to the change in entropy of reaction. Next, Faraday's law and Ohm's law simplify Equation 2.9 to

$$C_{p,\mathrm{eff}} \frac{\partial T}{\partial t} = \nabla \cdot (k_{\mathrm{eff}} \nabla T) + \frac{1}{\rho_{\mathrm{sol}}} ||\vec{\nabla} \Phi_{\mathrm{sol}}||^2 + \frac{1}{\rho_{\mathrm{liq}}} ||\vec{\nabla} \Phi_{\mathrm{liq}}||^2 + \rho_{\mathrm{k}} i_{\mathrm{k}}^2 - \frac{a_V T \Delta \overline{S}_{\mathrm{rxn}}}{nF} i_{\mathrm{k}} \quad (2.10)$$

where $\Delta\overline{S}_{\text{rxn}}$ is the local reaction entropy. The right side of Equation 2.10 accounts for thermal conduction and contains four heat-generation terms, including joule heats associated with each phase in the porous electrode, joule heating associated with interfacial charge transfer, and reversible heat generation associated with reaction entropy. Use of Equation 2.10 assumes that the solid and liquid phases within a volume element of a porous electrode are in local thermal equilibrium; the heat capacity and thermal conductivity that appear should be interpreted as effective properties of the mixed phases.

In accordance with the experimental setup, a convective boundary condition is used at the external surfaces of the cell,

$$h(T - T_\infty) = -k_{\text{eff}}\vec{\nabla}T \cdot \vec{n}. \tag{2.11}$$

Here h is an interfacial heat-transfer coefficient and $\vec{n}$ is a unit vector normal to the surface pointing outward.

The ionic conductivity and exchange current density were assumed to change with temperature linearly and exponentially, respectively:

$$\kappa_{\text{liq}}(T) = \kappa_{\text{liq}}^{\infty} + \alpha_{\kappa_{\text{liq}}}(T - T_\infty), \tag{2.12}$$

$$i_0(T) = i_0^{\infty} \exp\left[-\frac{E_{i_0}}{R}\left(\frac{1}{T} - \frac{1}{T_\infty}\right)\right]. \tag{2.13}$$

Here $\kappa_{\text{liq}}^{\infty}$ and i_0^{∞} are the properties at ambient temperature, and E_{i_0} is the activation energy for the exchange current density.

Equations 2.1 to 2.8 combine with Equation 2.10 to simulate the coupling between electric and thermal phenomena in a porous electrode. Note that even this ostensibly 'simple' formulation of the electrothermal porous-electrode transport model and its associated boundary conditions contains many parameters. It is already difficult to see what properties affect the system response, and in what ways.

2.4 COMSOL Multiphysics and model implementation

2.4.1 Non-dimensionalization

Newman and Tobias [80] provided a compact set of dimensionless parameters that control the charge distribution and reaction distribution within a porous electrode at steady state. In this section, their dimensional analysis is expanded to analyze the transient thermal response. Dimensional analysis of the equation system reveals that the physics is governed by the control parameters

$$\mathrm{I} = \frac{i_{\mathrm{app}}}{i_0 a_V \delta} = i_{\mathrm{app}} \frac{\rho_{\mathrm{k}}}{a_V^2 \delta} \frac{nF}{RT_\infty}, \quad \text{and} \quad \mathrm{Bi} = \frac{h\delta_{\mathrm{T}}}{k_{\mathrm{eff}}}, \tag{2.14}$$

and the material properties:

$$\mathrm{P_{sol}} = \frac{\rho_{\mathrm{sol}}}{\rho_{\mathrm{k},\infty}} a_V^2 \delta^2, \mathrm{P_{liq,\infty}} = \frac{\rho_{\mathrm{liq},\infty}}{\rho_{\mathrm{k},\infty}} a_V^2 \delta^2, \mathrm{P_{cc}} = \frac{\rho_{\mathrm{cc}}}{\rho_{\mathrm{k},\infty}} a_V^2 \delta^2,$$
$$H = \frac{n^2 F^2 \rho_{\mathrm{k},\infty} h}{R^2 T_\infty a_V^2 \delta_{\mathrm{T}}}, \sigma = \frac{\Delta \overline{S}_{\mathrm{rxn}}}{R}, K_U = \frac{nF}{RT_\infty} k_U,$$
$$\text{and } \bar{Q}_{\max} = \frac{Q_{\max}}{C_{p,\mathrm{eff}}} \frac{R}{nF}. \tag{2.15}$$

The control parameters I and Bi are dimensionless applied current and Biot number, respectively. Material characteristics are embodied by, $\mathrm{P_{sol}}$, $\mathrm{P_{liq}}$, and $\mathrm{P_{cc}}$, which are the ratios of the porous-electrode solid, porous-electrode liquid, and current-collector resistivities to kinetic resistivity, respectively. The thermal parameter H expresses the ratio between the rate of heat dissipation and the characteristic rate of heat generation by the electrochemical reaction. σ is the dimensionless entropy of reaction, K_U is the dimensionless OCP gradient, and $\bar{Q}_{\max}$ expresses the relative magnitudes of charge capacity and heat capacity.

The control parameter and material properties determine relationships between the dimensionless positions ξ_x, ξ_y, and ξ_z, dimensionless time τ, the solid- and liquid-phase voltages ϕ_{sol} and ϕ_{liq}, current collector voltage ϕ_{cc}, the dimensionless surface overpotential ι_{k}, and the temperature distribution θ. The independent variables are defined as

$$\xi_x = \frac{x}{\delta}, \xi_y = \frac{y}{L_y}, \xi_z = \frac{z}{L_z}, \quad \text{and} \quad \tau = \frac{ht}{C_{p,\text{eff}}\delta_\text{T}} \tag{2.16}$$

and the dependent variables are

$$\phi_\text{sol} = \frac{nF\Phi_\text{sol}}{RT_\infty}, \phi_\text{liq} = \frac{nF\Phi_\text{liq}}{RT_\infty}, \phi_\text{cc} = \frac{nF\Phi_\text{cc}}{RT_\infty}, \iota_\text{k} = \frac{\rho_{\text{k},\infty} i_k}{a_V}\frac{nF}{RT_\infty}, \quad \text{and} \quad \theta = \frac{T}{T_\infty}. \tag{2.17}$$

Here x is the direction normal to the stacked electrodes; y and z are directions in the plane of the electrode. δ, δ_T, L_y, and L_z are the electrode thickness, total thickness, width of the battery, and length of the battery, respectively.

Incorporating the dimensionless quantities in Equations 2.14 to 2.17 and defining the dimensionless gradient operator $\vec{\nabla}^*$ as

$$\vec{\nabla}^* = \vec{e}_x\frac{\partial}{\partial\xi_x} + \vec{e}_y\frac{\delta}{L_y}\frac{\partial}{\partial\xi_y} + \vec{e}_z\frac{\delta}{L_z}\frac{\partial}{\partial\xi_z}, \tag{2.18}$$

where $\vec{e}$ are the unit vectors in each dimension. Governing Equations 2.1 to 2.8 become

$$\nabla^{*2}\phi_\text{sol} = \iota_\text{k}\text{P}_\text{sol}, \tag{2.19}$$

which describes the solid phase of the porous electrodes,

$$\nabla^{*2}\phi_\text{liq} - \frac{d\ln\tilde{\rho}_\text{liq}}{d\theta}\left(\vec{\nabla}^*\theta\cdot\vec{\nabla}^*\phi_\text{liq}\right) = -\iota_\text{k}\text{P}_{\text{liq},\infty}\tilde{\rho}_\text{liq}, \tag{2.20}$$

which describes the liquid phase, and

$$\nabla^{*2}\phi_\text{cc} = 0, \tag{2.21}$$

which describes the current collector. To decrease computational cost several governing equations were combined analytically. To get Equations. 2.19 and 2.20, Equations. 2.1 and 2.2 were inserted into Equations. 2.7 and 2.8 and then nondimensionalized. Laplace's equation can be used to describe the voltage in the current collectors, which comprise only a single phase, whose parameters are independent of temperature.

At the top of the tabs, the applied electric current gives the following flux boundary condition:

$$-\vec{\nabla}^*\phi_\text{cc}\cdot\vec{n} = \text{P}_\text{cc}\text{I}. \tag{2.22}$$

The superscript cc represents the current collector. The change of local SOC was also nondimensionalized to

$$\frac{\partial q}{\partial \tau} = \frac{1}{\bar{Q}_{\max} H} \iota_k. \tag{2.23}$$

Energy equation Equation 2.10 takes the dimensionless forms

$$\frac{\partial \theta}{\partial \tau} = \frac{1}{\mathrm{Bi}} \left(\nabla^{*2} \theta \right) + \frac{1}{H} \left\{ \frac{1}{\mathrm{P_{sol}}} ||\vec{\nabla}^* \phi_{\mathrm{sol}}||^2 + \frac{1}{\mathrm{P_{liq,\infty}} \tilde{\rho}_{\mathrm{liq}}} ||\vec{\nabla}^* \phi_{\mathrm{liq}}||^2 + \tilde{\rho}_{\mathrm{k}} \iota_k^2 + \sigma \theta \iota_{\mathrm{k}} \right\} \tag{2.24}$$

$$\hat{C}_{p,\mathrm{cc}} \frac{\partial \theta}{\partial \tau} = \hat{k}_{\mathrm{cc}} \frac{1}{\mathrm{Bi}} (\nabla^{*2} \theta) + \frac{1}{H} \frac{1}{\mathrm{P_{cc}}} ||\vec{\nabla}^* \phi_{\mathrm{cc}}||^2 \tag{2.25}$$

in the porous electrode and current collector, respectively. Note that in the current collector, the generation term includes only joule heating. The temperature dependences of the parameters κ_{liq} and i_0 were also represented in the dimensional analysis section through properties $\tilde{\rho}_{\mathrm{liq}}$ and $\tilde{\rho}_{\mathrm{k}}$ (recall that $\rho_{\mathrm{k}} = a_V RT/i_0 nF$). This added thermal effect on the parameters is necessary to explain the gradual decrease in voltage envelope during cycling: in all experiments, it was found that the maximum variation of voltage ΔV_{T} decreased over time as the system evolved toward its periodic steady state, and this decrease correlated precisely with the average temperature. Parameters $\tilde{\rho}_{\mathrm{liq}}$ and $\tilde{\rho}_{\mathrm{k}}$ represent the ratio between the respective resistivities evaluated at local temperature T and T_∞, *i.e.* $\tilde{\rho}_{\mathrm{liq}} = \dfrac{\rho_{\mathrm{liq}}}{\rho_{\mathrm{liq},\infty}}$ and $\tilde{\rho}_{\mathrm{k}} = \dfrac{\rho_{\mathrm{k}}}{\rho_{\mathrm{k},\infty}}$. Also, since the thermal properties in the current collector differ from the active materials in the cell, $\hat{C}_{p,\mathrm{cc}}$ and $\hat{k}_{\mathrm{cc}}$ are introduced to represent the ratio between the respective parameter values in the current collector and those in the porous electrode. Finally, the convective boundary condition at all the external surfaces, Equation 2.11, nondimensionalizes to

$$\mathrm{Bi}(\theta - 1) = -\vec{\nabla}^* \theta \cdot \vec{n}. \tag{2.26}$$

2.4.2 Scaling laws for multilayer cells

The number of consecutive electrochemical-cell-sandwich layers in the cell was estimated as $N = 40$, based on the thickness of an unwound electrode measured with calipers (note that because the current collectors are coated on both sides, the number of 1/2 anode - cathode - 1/2 anode repeat units is therefore 20). To reduce the computational burden, only one layer of electrodes and current collectors with thickness 40 times larger than the actual thickness was simulated ($\delta_1 = \delta_N \times N$). The simulation was simplified by the following scaling argument: the N-layer cell has N times the total surface area of one layer, the current density of an N-layer cell is $\frac{1}{N}$ of that in a one-layer cell; the thickness of a layer in an N-layer cell is $\frac{1}{N}$ of the one-layer cell's thickness, however, so $\delta_N = \frac{\delta_1}{N}$. Thus, the constancy of the current parameter defined in Equation 2.14 implies that the ratio between kinetic resistivity and the square of surface-to-volume ratio does not change if the number of layers is rescaled, because

$$\begin{aligned} \mathrm{I}_1 &= \mathrm{I}_N \\ \frac{i_{\mathrm{app},1}\rho_{\mathrm{k},1}}{\delta_1 a_{V,1}^2} &= \frac{i_{\mathrm{app},N}\rho_{\mathrm{k},N}}{\delta_N a_{V,N}^2} \\ \left(\frac{\rho_{\mathrm{k}}}{a_V^2}\right)_1 &= \left(\frac{\rho_{\mathrm{k}}}{a_V^2}\right)_N \end{aligned} \tag{2.27}$$

Using this conclusion, it can be shown that to make the dimensionless numbers $\mathrm{P}_{\mathrm{sol}}$, $\mathrm{P}_{\mathrm{liq}}$, and P_{cc} in equation 2.15 invariant between one-layer and N-layer cells, the respective resistivities in the one-layer cell need to be multiplied by a factor of N^2:

$$\begin{aligned} \mathrm{P}_{\mathrm{sol},1} &= \mathrm{P}_{\mathrm{sol},N} \\ \left(\frac{a_V^2}{\rho_k}\right)_1 \rho_{\mathrm{sol},1}\delta_1^2 &= \left(\frac{a_V^2}{\rho_k}\right)_N \rho_{\mathrm{sol},N}\delta_N^2 \\ \rho_{\mathrm{sol},1}N^2 &= \rho_{\mathrm{sol},N}. \end{aligned} \tag{2.28}$$

Other parameters, including thermal conductivity, heat transfer coefficient, reaction entropy, OCP gradient and heat capacity do not need to change to leave the

dimensionless numbers I, Bi, σ, K_U, and τ invariant. This analysis with the other dimensionless parameters is shown below:

$$\begin{aligned} \sigma_{\mathrm{N}} &= \sigma_1 \\ \frac{\Delta \bar{S}^N_{\mathrm{rxn}}}{R} &= \frac{\Delta \bar{S}^1_{\mathrm{rxn}}}{R} \\ \Delta \bar{S}^N_{\mathrm{rxn}} &= \Delta \bar{S}^1_{\mathrm{rxn}}, \end{aligned} \tag{2.29}$$

$$\begin{aligned} H_N &= H_1 \\ \left(\frac{n^2F^2}{R^2T_\infty}\right)\left(\frac{\rho_{\mathrm{k},\infty}}{a_V^2}\right)_N \frac{h^N}{\delta^N_{\mathrm{T}}} &= \left(\frac{n^2F^2}{R^2T_\infty}\right)\left(\frac{\rho_{\mathrm{k},\infty}}{a_V^2}\right)_1 \frac{h^1}{\delta^1_{\mathrm{T}}} \\ h^{\mathrm{N}} &= h^1, \end{aligned} \tag{2.30}$$

$$\begin{aligned} \mathrm{Bi}^N &= \mathrm{Bi}^1 \\ \frac{h^{\mathrm{N}}\delta^N_{\mathrm{T}}}{k^N_{\mathrm{eff}}} &= \frac{h^1\delta^1_{\mathrm{T}}}{k^1_{\mathrm{eff}}} \\ k^N_{\mathrm{eff}} &= k^1_{\mathrm{eff}}. \end{aligned} \tag{2.31}$$

The cell capacity $Q_{\max}$, whether or not it is the multilayer or single layer equivalent will be set to have the same capacity, which allows us to make the next conclusion in regards to $C_{p,\mathrm{eff}}$:

$$\begin{aligned} \bar{Q}^N_{\max} &= \bar{Q}^1_{\max} \\ \frac{Q^N_{\max}}{C^N_{p,\mathrm{eff}}}\frac{R}{nF} &= \frac{Q^1_{\max}}{C^1_{p,\mathrm{eff}}}\frac{R}{nF} \\ C^N_{p,\mathrm{eff}} &= C^1_{p,\mathrm{eff}}, \end{aligned} \tag{2.32}$$

and finally,

$$\begin{aligned} K^N_U &= K^1_U \\ \left(\frac{nF}{RT_\infty}\right)k^N_U &= \left(\frac{nF}{RT_\infty}\right)k^1_U \\ k^N_U &= k^1_U. \end{aligned} \tag{2.33}$$

2.4.3 Model implementation and parameter estimation

COMSOL Multiphysics software was used to implement finite-element numerical analysis. The generic partial-differential-equation solver in COMSOL was used to implement the model equations stated above. Fitting parameters were determined by varying key dimensional material properties, such as $\Delta\bar{S}_{\mathrm{rxn}}$ to vary σ, ρ_{sol} to vary $\mathrm{P}_{\mathrm{sol}}$, and so on. Geometric paramters and solid-phase conductivities were taken from measurements or literature [56, 81, 85, 99–102].

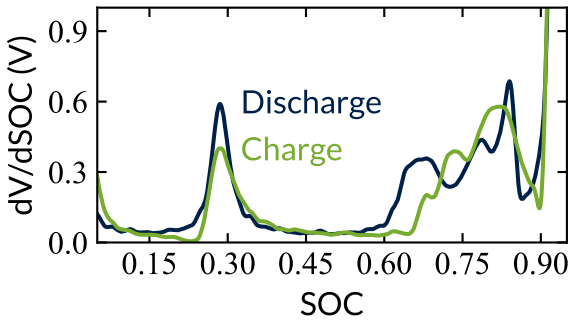


Figure 2.9: A plot of $\frac{dV}{dSOC}$ for the pseudo-OCP curves from Figure 2.8, used for k_U estimation

The OCP of the cathode (LFP) is effectively linear with a low rate of change across multiple wide ranges of SOC [85]. The gradient of the OCP with respect to SOC (k_U) was estimated by taking the derivative of measured pseudo-OCP data from our specific type of cell at the average SOC of interest. This calculation was done on both the charge and discharge steps and the absolute values are plotted in Figure 2.9. Pseudo-OCP data was obtained by charging the cell from 0% to 100% SOC by following a CCCV protocol with an end condition of 0.2 A (C/100), followed by a rest of an hour, and then discharging the cell to 0% SOC at a slow C-rate of C/25 with a Maccor battery tester. Note that 100% SOC was defined as the state at an OCP of 3.6 V, and 0% was defined as the state with an OCP of 2.5 V. Pseudo-OCP measurement was performed within a Binder thermal chamber held at 25 °C.

Since the Biot number for this experimental configuration is small (~ 0.01) the time constant for the thermal response strongly depends on the heat transfer

coefficient h, rather than the effective thermal conductivity of the cell. The Biot number is defined as $\frac{hL_{\mathrm{C}}}{k}$, for this system, free convection in air yields h values between 1 and 10 $\frac{\mathrm{W}}{\mathrm{m^2K}}$, while the characteristic lenght of this battery is ~ 0.001 m, and a through-plane conductivity value of 1 $\frac{\mathrm{W}}{\mathrm{m\ K}}$ was used from Maleki *et al.* [103]. Thus, the time constant of the average-temperature relaxation yields the heat transfer coefficient, rather than producing information about the thermal diffusivity. In order to find optimal values of other thermal and electrochemical parameters, nonlinear least squares optimization was performed by fitting the periodic steady state data (from $\sim$ 2000 s onwards) including cell voltage, minimum, maximum, and average temperatures for the 4c100s squarewave. The least squares routine in MATLAB (LSQNONLIN) was applied by integrating MATLAB's scripting environment with COMSOL Multiphysics' simulations via LiveLink for MATLAB. The cost function used for nonlinear least squares was taken to be

$$\min_{p} \left[\sum_{i=1}^{N_t} \left(\frac{T^{\mathrm{m}}_{\mathrm{max},i} - T^{\mathrm{exp}}_{\mathrm{max},i}}{T^{\mathrm{m}}_{\mathrm{max},i}} \right)^2 + \left(\frac{T^{\mathrm{m}}_{\mathrm{avg},i} - T^{\mathrm{exp}}_{\mathrm{avg},i}}{T^{\mathrm{m}}_{\mathrm{avg},i}} \right)^2 + \left(\frac{T^{\mathrm{m}}_{\mathrm{min},i} - T^{\mathrm{exp}}_{\mathrm{min},i}}{T^{\mathrm{m}}_{\mathrm{min},i}} \right)^2 + \left(\frac{V^{\mathrm{m}}_{\mathrm{cell},i} - V^{\mathrm{exp}}_{\mathrm{cell},i}}{V^{\mathrm{m}}_{\mathrm{cell},i}} \right)^2 \right] : p^l \leq p \leq p^u \tag{2.34}$$

where superscripts m and exp represent the model and the experimental results, and p^{l} and p^{u} are the lower and upper bounds for the parameters, respectively; N_t represents the number of time steps simulated. Obtained parameter sets were checked to see if any particular values were far from being realistic. Occasionally the LSQNONLIN algorithm will converge on to a set of values where one parameter is far out of range of what is realistic while other parameters made up for its problems. In such cases, initial conditions were adjusted to so that the outlier optimizes to a more plausible value.

The reported average temperature is a surface average, which was evaluated in simulations by integrating the temperature distribution across the whole surface, then dividing by the surface area. In experiments, the surface average was evaluated by summing every pixel's temperature and dividing by the number of pixels.

Experimentally, it was observed that the locations of the maximum and minimum temperatures did not change with time after a relatively early relaxation period. To simplify the work associated with experimental data processing, the locations of the maximum and minimum spots were fixed; only those small areas of the images were probed to evaluate the maximum and minimum temperatures. A spot size of five pixels by pixels (corresponding to ~ 88 mm^2) on the battery surface was ultimately used to gather thermal data around the hot and cold spots.

As previously mentioned, the number of layers in the cell was estimated to be 40. However, our implementation of scaling within the model allows this to be represented by one layer with 40 times the true thickness. This is justified as long as the Biot number is low (so the internal temperature of the cell is relatively uniform in the direction perpendicular to the largest faces of the battery), and other parameters are scaled to reflect the geometric adjustment. The single layers that represent the cathode and anode are also the same in this implementation for simplicity's sake. Therefore the numbers represent the effective values of the listed parameters. To further simplify the problem, a separator domain has not been explicitly included in the model equations. The consequences of this choice will be discussed in the following results section.

The copper bars that were used to connect the battery to the power supply were also simulated within the COMSOL model, by including them in the 3-D geometry. This was necessary because the bars act as a heat sink, which removes some of the heat generated within the small metal tabs. An enlarged 3-D representation of the geometry and the spatial mesh that was used for simulations is shown in Figure 2.10. In the schematics, the through-plane thickness has been multiplied by ten to ease visualization of the relative thicknesses of the different simulation domains. The COMSOL file and MATLAB codes used to solve the model and implement the optimization are available on GitHub [104].

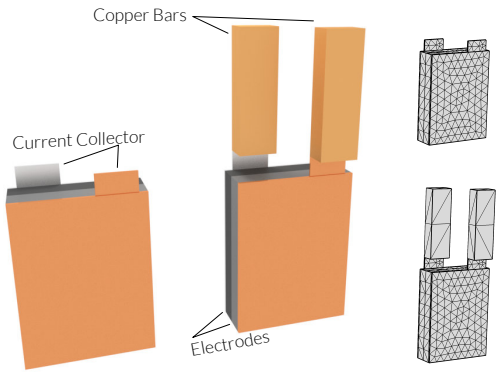
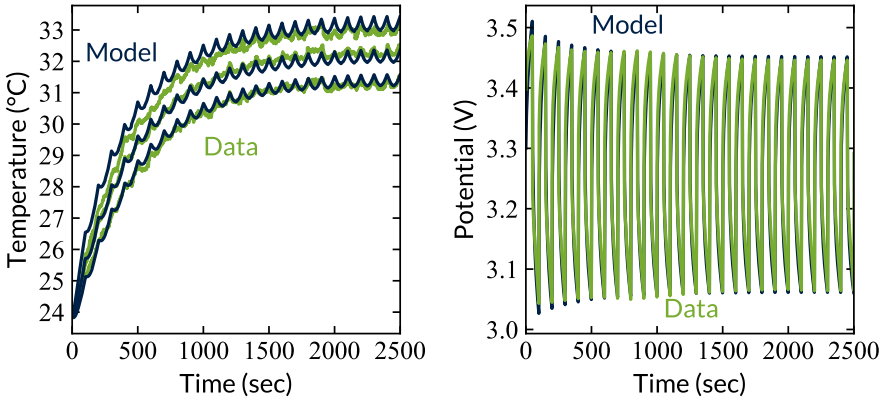


Figure 2.10: Geometry (left,colored) and mesh (right) that were implemented in COMSOL for the simulations. The copper bars were added to more closely mimic the experimental setup.

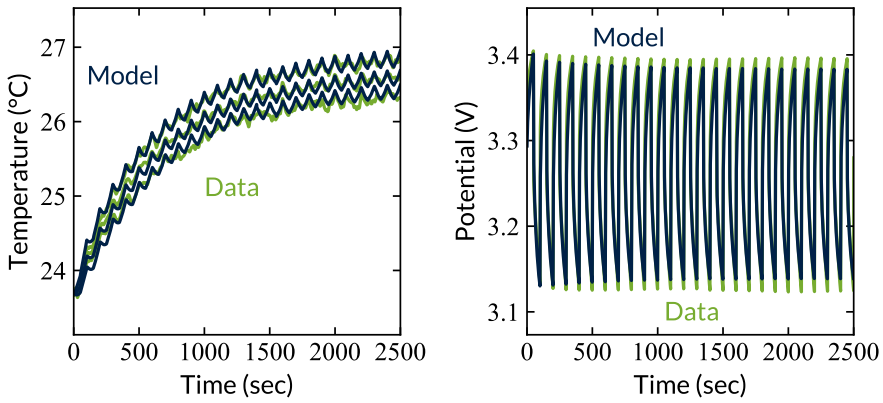
2.5 Results and discussion

Figure 2.11 compares the model output with the experimental results from three different excitation tests of the A123 prismatic cell. The first test and also the chosen experiment for fitting was the 4c100s squarewave, which is shown as the first set of plots in the figure. The parameter sets shown in Table 2.1 was for 30%, 50%, and 70% SOC. By using the extracted parameter set as new inputs for the COMSOL simulation, the model was then used to predict the behavior under other control conditions. Minor adjustments were made to reflect changes in ambient and operating conditions: for instance, material properties $\kappa_{\text{liq}}^{\infty}$ and i_0^{∞} were adjusted to represent the values at the ambient temperatures in which experiments were performed. With these corrections, the model was then validated by comparing the model output with two different experiments, one with a different C-rate and similar period (2c100s), and one with the same C-rate and a different period (4c50s). The results of these two validations tests are shown in Figures 2.11b and 2.11c. Using 4c100s as the fitting dataset yielded the best qualitative matches when the parameters were used to simulate the 2c100s and 4c50s experiments. Attempts to extract different parameters using the 2c100s and 4c50s datasets yielded results that were objectively worse when attempting to simulate the remaining experiments.

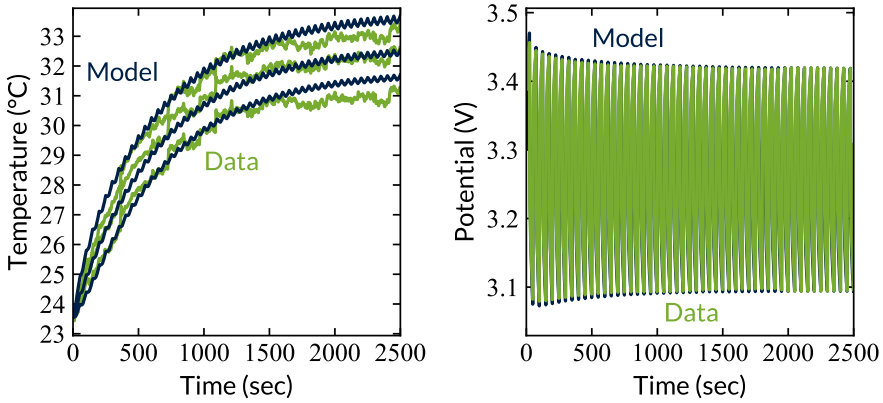
The simulation matches the thermal response as well as the electrical response. The match supports the assertion that a simple thermoelectrochemical model



(a)



(b)



(c)

Figure 2.11: Comparison of model output and experimental data for three different excitation tests of the LFP cell for (a) 4c100s, (b) 2c100s, and (c) 4c50s input signals. The plots in (a) were the result of data fitting, while (b) and (c) were validation tests obtained by using the parameter set from (a).

Table 2.1: Parameter values for fitting the 4c100s squarewave data. The modified values were implemented to recreate a reasonable reaction distribution in the porous electrode after simplifying its geometry.

Parameters	**30%**	**50%**	**70%**	**Literature/Measured Value**
h(W m^2 K)	12.5	10.6	10.4	3-20 [56, 105]
$C_{p,\text{eff}}$ (J m^{-3} K^{-1})	2.32×10^6	2.04×10^6	2.09×10^6	1×10^6 - 3.5×10^6 [57, 81]
$\Delta\bar{S}_{\text{rxn}}$ (mV K^{-1})	-0.14	0.08	0.10	$\lvert 0.01 - 1\rvert$ [91, 106]
i_0 (A m^{-2}) at 25 °C	i_0^{∞}(A m^{-2}) = 14.31	11.99	11.89	0.01-50[82]
	E_{i_0}(KJ mol^{-1}) = 30.81	30.61	28.75	0.1-1 [82]
κ_e(S m^{-1})	κ_e^{∞}(S m^{-1}) = 0.022	0.019	0.022	0.1-1 [85, 102]
	α_{κ_e}(S m^{-1}K^{-1}) = 0.002	0.002	0.003	
k_{eff}(W m^{-1}K^{-1})	54.4	72.0	60.1	5-380 [81]
k_U(V)	0.36	0.22	0.17	30% : 0.33-0.40 50% : 0.03-0.035 70% : 0.21-0.31

Table 2.2: A123 20 Ah electrode and current collector fixed parameters used in the model.

Parameters	**Electrodes**	**Current collectors**
thickness(mm)	2.7	0.4
width(mm)	150	48
height(mm)	200	25
a_V(m^{-1})	10^7	N/A
k_{eff} (W m^{-1} K^{-1})	-	380
κ_{sol} (S m^{-1})	50	10^7

based on Newman-Tobias theory with linear kinetics suffices to model the whole pouch cell. Fixed parameters are listed in Table 2.2, while the fitted and corrected parameters are listed in Table 2.1. For a_V, the value is only applicable to the electrodes and not to the metal current collectors. For k_{eff}, only the metal outer layers take the fixed values, while the electrodes' conductivity is optimized. Most parameter values fall within the range reported in literature. A notable exception is k_{liq}^{∞}, whose extracted value is $\sim$ 0.02 S m^{-1}, while typically reported values are 0.1-1.0 S m^{-1}. This discrepancy likely owes to the fact that a separator layer was not explicitly included, which should decrease the expected value to the effective conductivity observed. In Chapter 3, this characterization approach was tested on another battery chemistry, and the shortcomings in that system along with the ones here, provides insight towards determining what physics might be necessary to account for this ionic conductiviy value.

The parameterization was also implemented for a few data sets centered around 50% and 70% SOC; corresponding data are also reported in Table 2.1. Most parameters again matched literature values well, with the exception of $\kappa_{\text{liq}}^{\infty}$. For 30% SOC, the k_U value of 0.36 V is close to the measured value at 30% ($\sim$0.33 V on charge and $\sim$ 0.40 V on discharge). In the 50% SOC scenario, the extracted k_U value was 0.22 V, however, *vs.* the measured value of $\sim$0.035 V on charge and discharge. This could imply that the current model cannot accommodate for chemistries with large plateaus in their OCP curves without the inclusion of extra physics. Nevertheless, five out of the seven model parameters did not change

significantly across the three different charge states used as reference points. As expected, the remaining two, k_U and $\Delta\bar{S}_{\mathrm{rxn}}$, whose values derive from derivatives of the OCP, do change with mean SOC.

2.6 Conclusions

A thermo-electrochemical model that modifies the isothermal Newman-Tobias model to account for a local thermal energy balance was developed and used to match experimental temperature-distributions as well as the voltage data for a 20 Ah LFP pouch cell from A123. Despite the many simplifications to the model, what remained after streamlining was sufficient to simulate pouch cell behaviors under this experimental protocol. This model in particular showing that the coupling between temperature and SOC were key contributors to the way that voltage developed and diffusion was not yet necessary.

Dimensional analysis showed that seven dimensionless variables control the output of a 3-D simulation of a squarewave-current excitation test, and that the simulation can be simplified to model a cell containing many planar layers with a single-layer simulation by rescaling certain model parameters, so long as the Biot number is low. The nonuniform temperature distribution on the cell surface owes to the fact that cells have been designed for ease of wiring, with both tabs on the same edge of the cell, rather than to achieve a uniform internal current distribution. The nonuniformity of temperature is useful, however, because it can be gauged to obtain estimates of internal material properties. Using an iterative procedure based on a numerically computed goal-seeking algorithm, material properties were estimated for an A123 20 Ah LFP battery. The extracted ionic conductivity value was on the lower range of values typically reported in literature and the k_{U} value being overpredicted in certain test cases could indicate a missing source of resistance that both increases the voltage envelope and the heat generated.

It was also shown that the model had extrapolative capability; best-fit parameters obtained from a simulation fit at a high C-rate could be used to predict the outputs at a different lower C-rate or at a different frequency. This inverse modelling approach

allowed for the estimation of seven key parameters using a single experimental dataset in a nondestructive way, suitable for cell diagnostics and second life screening.

3

State of Health Tracking using Lock-in Thermography

3.1 Introduction

Degradation tracking is important in determining the end of life for a cell. State of health (SOH) is most commonly defined as the remaining capacity of a cell as a percentage of the capacity when the cell was new. There are a variety of different processes that occur as a result of how a battery is used and the environmental conditions it was used in [37, 107]. Birkl *et al.* summarized how triggers such as high/low temperature operation or storage, overcharge, undercharge, and mechanical stresses can cause various mechanisms to occur in the electrodes, electrolytes, and current collectors, which ultimately culminate as a measurable capacity fade or a power fade [45]. With the standard current and voltage measurements that go along with the cell during operation, some conclusions regarding what degradation mode is occurring can be drawn using a technique such as differential voltage analysis (DVA) [41, 42]. While it is possible to use this technique on a full cell by making certain assumptions about the individual electrodes, it is more definitive if there are half-cell experiments to compare to compare against. Half-cell measurements generally have to come from a post mortem analysis, where electrodes are salvaged from a deconstructed full cell.

By incorporating another external measurement, such as a cell temperature – or even a temperature distribution, it might be possible to provide further insight into the state of health of a battery. The previous chapter demonstrated the capability of the streamlined electrochemical/thermal model for non-destructive property estimation from lock-in thermography of large-format LFP cells. A few parameters, such as the reaction entropy, $\Delta\bar{S}_{\text{rxn}}$, and the slope of the linearized OCV curve, k_U, are sensitive to changes in the battery's open-circuit equilibrium state – that is to say, its average SOC. A large majority of the extracted parameters, however, do not seem to be affected by the change in baseline SOC. So, a potential application of the LIT analysis technique laid out in the prior chapter is to see if the parameter vector can be monitored to give a finer-grained assessment of battery health than the typical coarse SOH metric. Hereafter, the term "SOH" will be used to refer to a more holistic property vector that accounts for the state of materials and interfaces within the battery, as well as for its capacity.

Although there are no degradation mechanisms built into the model, the inverse modelling approach captures the effective values of parameters at a given state of the battery. Since degradation processes tend to occur over timescales much slower than a typical battery cycle, or indeed, an LIT experiment, it is possible to apply parameter extraction throughout a battery's lifetime and attribute changes in the observed parameter sets to changes in a battery's health.

With decreasing SOH, there should be changes in the voltage and temperature responses that result from the squarewave-current input signal. For example, one might expect an increase in the size of the voltage envelope due to changes in electrical parameters like κ_{e} and i_0. Recall, the voltage envelope is in reference to squarewave experiment's voltage data where the peak and valley values of the voltage get progressively closer together after each successive squarewave. Measurements of a battery cell's internal resistances has been used alongside capacity loss to determine the health state of a battery in a more sophisticated way [43, 108]. However, this can also be done through other methods like direct current internal resistance (DCIR)

tests [46, 50, 109]. DC resistance is typically measured by applying a pulse current of a chosen magnitude for 10 seconds and then using Ohm's law,

$$R_{\mathrm{DC}} = \frac{V_{10s} - V_{0s}}{I}, \tag{3.1}$$

to calculate the resistance [51, 52].

Adding in the thermal signatures of cell degradation could give us a clearer picture of SOH, because a battery's performance highly depends on the thermal stability of the individual components and how they were assembled [96]. For example, Maleki *et al.* [103] studied changes in thermal conductivity when a cell is cycled 500 times in a high temperature environment. They did see changes in the thermal conductivity of their silicon anode cells, but less so in cells with transition metal oxide cathodes and graphitic anodes. The larger volume expansions of silicon anodes changing the laminar structure in the electrode stack seems to be the source of the modified through-plane thermal conductivity. Another change in the thermal response as a battery ages would be an overall increase in the average surface temperature from the LIT experiment because internal resistances typically increase monotonically over a battery's cycling history [67, 108]. If degradation protocols can physically alter a battery, and these changes can induce a modified thermal response, it can potentially be used to gauge battery SOH. If packs are being disassembled before being recycled or incinerated, cell diagnostics as an intermediate step could allow for some cells to be reused or repurposed. Through inverse modelling, changes in the shape of the surface-temperature distribution may be able to more finely resolve where the resistance changes are greatest (*e.g.* at interfaces, in the electrolyte, or in the solid phase).

3.2 Experimental

3.2.1 Experimental Apparatus Design Update

The LFP cells that were used to validate the electrochemical/thermal model in Chapter 2 are known to have better cycling capability and safety than their transition metal counterparts [106, 110, 111]. These advantages come at the expense of energy

Table 3.1: Kokam SLPB75106205 specifications

Parameter	Value
Manufacturer Identifier	SLPB75106205
Cathode	NMC
Width	205 mm
Height	106 mm
Thickness	7.5 mm
Upper voltage cut-off	4.2 V
Nominal voltage	3.7 V
Lower voltage cut-off	2.7 V
Nominal capacity	16 Ah
Max continuous discharge current	80 A
Max continuous charge current	16 A

density, because LFP cathodes have lower nominal voltage compared to other chemistries, such as lithium cobalt oxide (LCO) and nickel manganeses cobalt oxide (NMC). For a study tracking degradation, therefore, it was deemed more appropriate to use a cell chemistry that would degrade faster than LFP – an approach that would have the further advantage that it could be used to test whether the model used for parameter estimation is chemistry agnostic. Kokam 16 Ah NMC cells were chosen for the experiments that follow. Besides the different cathode chemistry, the Kokam cells' dimensions also differ, which should affect how the temperature distribution develops over time. As well as the different lengths in different directions, the tab placement differs, which affects the current distribution in the cell, and consequentially the locations within the cell that see more current throughput. Specifications of these Kokam cells are outlined in Table 3.1 and a size comparison between A123 and Kokam cells can be seen in Figure 3.3a.

A new cell holder had to be designed and fabricated such that it could hold the new battery and can also accept the connections from the existing power supply. Acrylic frames (6 mm thick) were once again cut out of sheets to hold the battery and an overhang piece was acetone-welded to the bottom of the frame to support the battery's weight. Another extra piece was cut and welded to the top part of the frame to prevent accidental short-circuits by physically blocking contact between the positive and negative terminals. Nylon plates were once again used to enclose

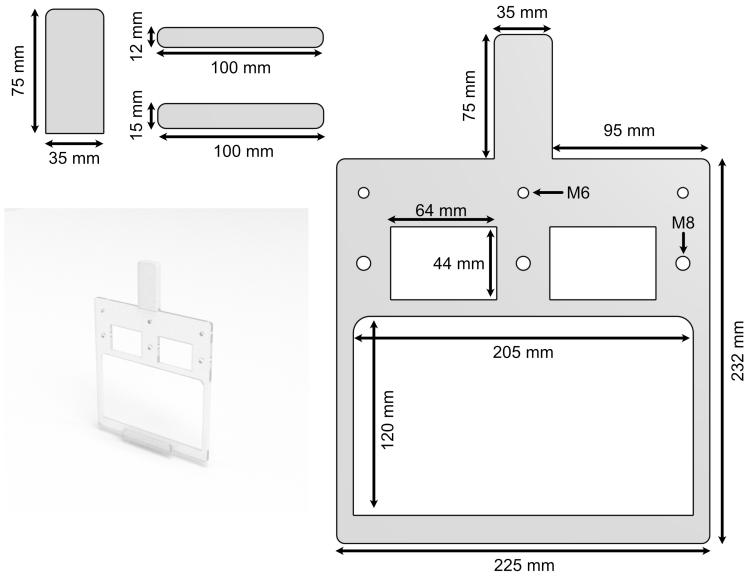


Figure 3.1: Acrylic frame drawing with render for Kokam 16 Ah pouch cells

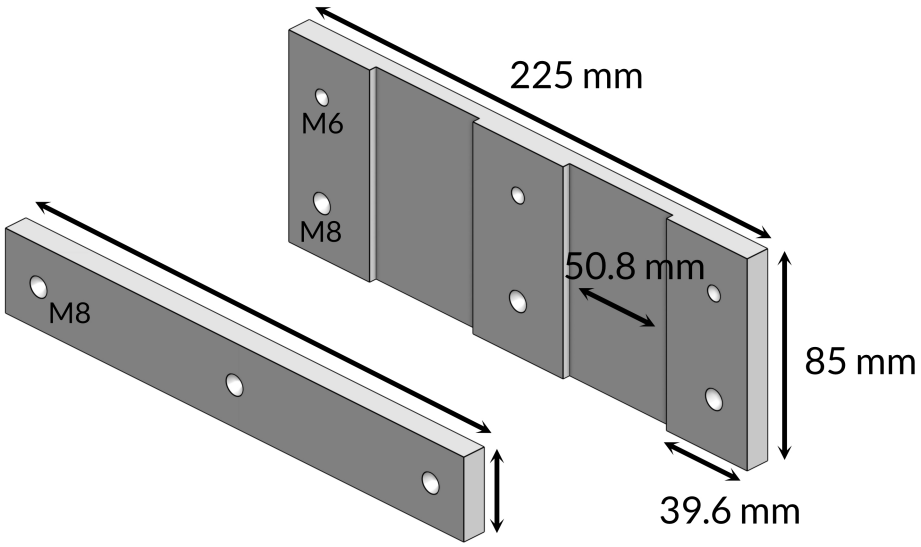
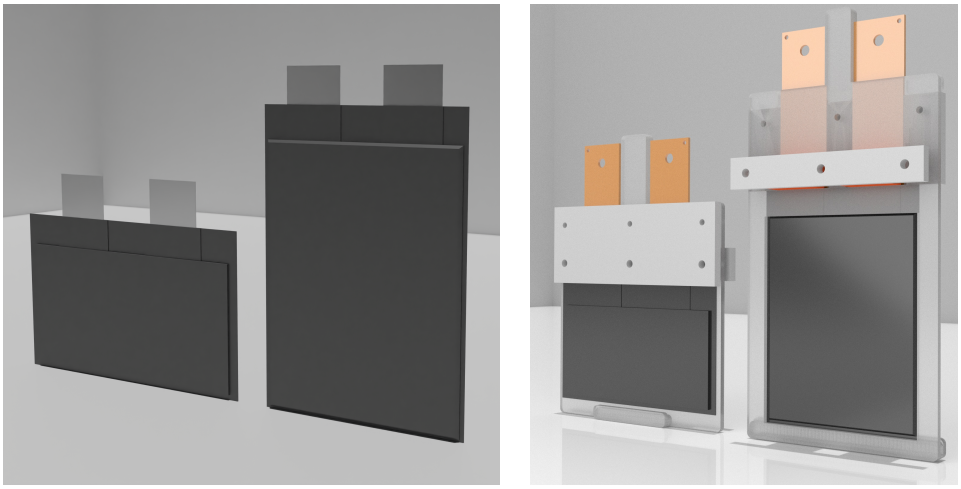


Figure 3.2: Nylon frame drawing for Kokam 16 Ah pouch cells

the copper bars that act as the connection point between the battery tester and the cells. The tabs of the battery were then pressed into the copper bars using silicone rubber pads glued to another nylon plate. Qualitatively, this is similar to what is depicted in Figures 2.2 and 2.3. Updated dimensions to fit the Kokam cells are presented in Figures 3.1 and 3.2. A comparison of the two different cell holders is presented in Figure 3.3b, where the left picture shows the Kokam cell in the holder, and the right shows the A123 cell.



(a) (b)

Figure 3.3: Complete cell holders for Kokam 16 Ah cells (left) and A123 20 Ah cells (right)

3.2.2 Matte Paint Effects

In the previous experimental section in Chapter 2, a layer of a matte paint was sprayed onto the surface of the battery to help deal with reflections and also create a surface with uniform emissivity. Before doing the next batch of experiments, it made sense to determine whether the layer of paint was completely necessary. In practice, if cells were to be assessed for second-life applications *via* LIT diagnostics, application of a layer of paint could be considered destructive. So, as a test, the squarewave experiment was done on a unpainted battery and then again on the same battery after a layer of paint was applied.

The result was that, in the same experimental rig, in the unpainted case, the IR camera can be clearly seen as a reflection on the surface of the battery. This can be seen in Figure 3.4, inside of the black square that highlights the battery active material area. We knew this would be the case as the layer of paint was initially used to prevent activities within the lab inducing reflections and disrupting the measurements of the IR camera. Orienting the camera into a portrait mode and moving it to the right does remove the camera reflection from view, but does not prevent interference from anything passing by, which would be a common occurrence in a busy lab.

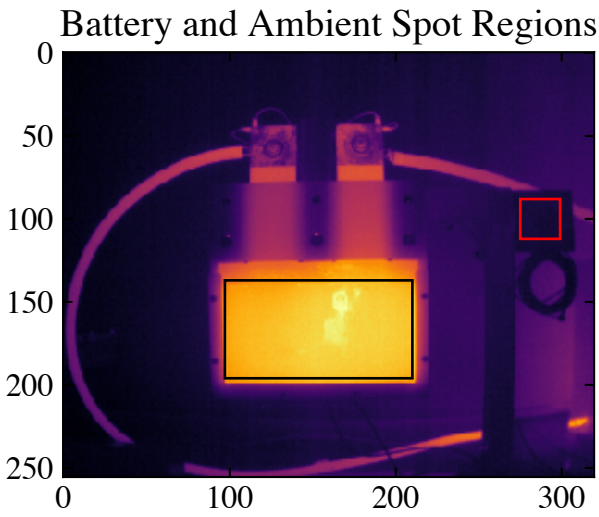
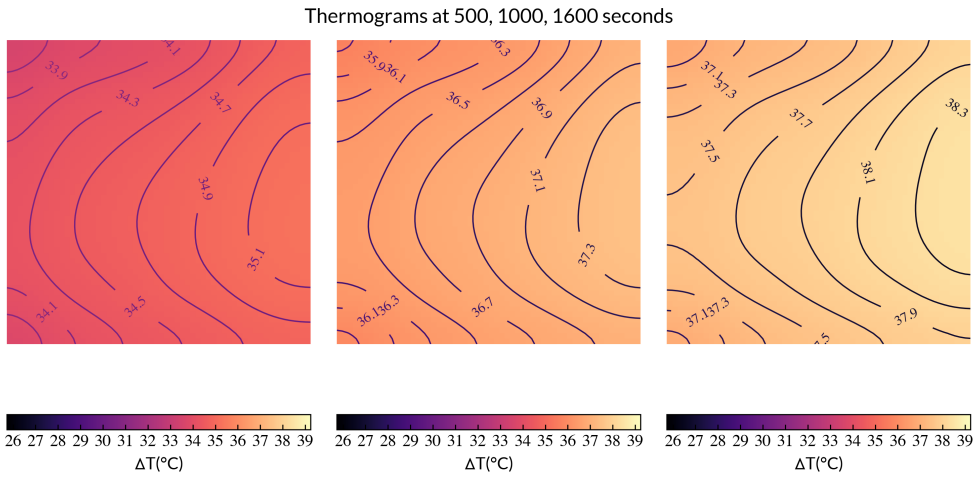


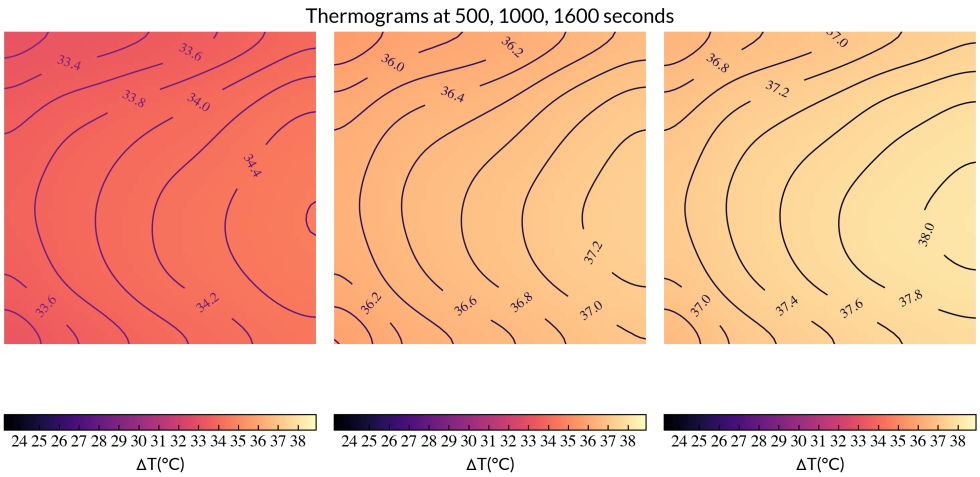
Figure 3.4: Thermogram of a Kokam cell without a layer of matte paint.

Nevertheless, the dataset from the unpainted battery was put through the same data processing steps outlined in the previous chapter, but was restricted to the portions of the battery surface that did not contain the camera reflection. In Figure 3.5a, we see the processed thermogram showing the temperature distributions of the unpainted battery at 500, 800, and 1600 seconds after applying a 5C amplitude and 100 s period squarewave. A layer of spray paint was then applied to that battery and then the experiment was repeated. Figure 3.5b shows the thermograms at the same time steps as the no-paint case. There is a small offset in the absolute temperature values, which could be caused by different ambient conditions (colder/hotter) because the two experiments were done on different days. The shapes of the contours are effectively the same at various stages of the experiment, and would therefore be expected to yield similar thermal properties from inverse modelling with the streamlined model.

With a high enough resolution sensor, and restricted placement options for the camera, reflections could be avoided. And with sufficient pixel resolution concentrated on the battery, the off-center placement would still provide adequate amounts of data where this thermographic analysis is possible. For the sake of convenience, a layer of paint was applied to all batteries analyzed here.



(a)



(b)

Figure 3.5: Thermograms of a Kokam cell with (a) no spray paint applied and (b) a layer spray paint applied, at various times during a squarewave excitation experiment.

3.2.3 Thermal Characterization of Pristine Kokam Cells

The degraded cells used for this analysis had to go through their degradation cycling procedure for about half a year. While this was happening, two pristine cells from the same manufactured batch (as assessed by the similarity in their serial numbers) were chosen to undergo lock-in thermography analysis based on a squarewave current input, as described in Chapter 2, to determine the parameter set of a new Kokam cell. The resulting thermograms were compared to determine if there were any noticeable differences between the thermal response of the cells. Figure 3.6 shows a

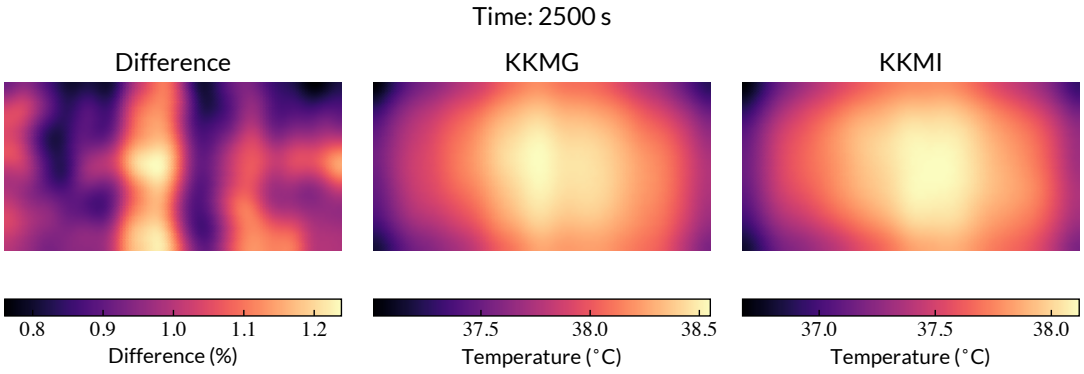


Figure 3.6: Series of thermograms showing two pristine cells (labelled KKMG and KKMI) undergoing a 5c100s experiment after 2500 seconds.

series of images that present the difference between two pristine cells undergoing the same 5C amplitude and 100 s period (abbreviated as 5c100s) squarewave experiment, followed by the thermograms of the two individual cells. At some locations there is about a 1% difference between the two thermograms at 2500 seconds, but the average variation across the entire distribution is less than half a percent. Even though there is an area where it seems like one cell is significantly hotter, this difference is within 0.15 degrees; the hotter area also moves around when stepping through the images frame-by-frame, suggesting that difference arises from random error.

In short, a qualitative comparison of the thermograms suggests that there is no significant difference between the thermal behaviors of these two fresh cells. The analysis method from the previous chapter (Section 2.4.3) relies on fitting the processed temperature data and the voltage data. To quantify how little of a difference there is, both thermal videos were processed into the $T_{\max}$, T_{avg}, and $T_{\min}$ datasets that serve as the goal for the fitting algorithm.

The processing procedure has also been updated. Instead of manually choosing where the hot spot is in the IR video, hot-spot identification is now automated by tracking the location of the maximum temperature at every time step after approximately the first three minutes (before which the temperature sensitivity is not sufficient to identify a particular hot spot). The list of these locations was then averaged to determine where to fix the hot spot location for inverse modelling.

Table 3.2: Extracted parameter sets for fresh cells, KKMG and KKMI at 50% SOC.

	KKMG	KKMI	Diff. (%)
$C_{p,\text{eff}}$ (J m^{-3} K^{-1}	3.503	3.495	0.22
k_{eff} (W m^{-1}K^{-1})	1.497	1.479	1.20
h (W m^2 K)	19.473	20.269	4.09
k_U (V)	0.47	0.45	3.34
κ_{liq} (S m^{-1}) at 25 °C	32.680	31.352	4.06
α_{κ_e} (S m^{-1}K^{-1})	31.086	30.857	0.74
i_0 (A m^{-2}) at 25 °C	0.879	0.921	4.78
E_{i_0}(KJ mol^{-1})	17.035	17.287	1.48
$\Delta\bar{S}_{\text{rxn}}$ (mV K^{-1})	0.065	0.076	16.92

This procedure change also allowed for a more systematic way of identifying where the hot spot preferred to develop.

Thermography results yielded from the altered data processing procedure are presented in Figure 3.7. The voltage curves look very similar, and the temperatures appear to be separated by a small offset. A portion of this offset is due to the ambient temperature being slightly different. The percent difference between T_{max}, T_{avg}, T_{min}, and V is shown in Figure 3.8. The hot spot, cold spot, and surface average temperatures start off differing by about 3% from each other, but gradually settle to a difference between 0.75% and 1.25% at periodic steady state. The voltage is also within ± 1% through the entire range, excepting a few outliers during the fast current flip from +80 A to −80 A and *vice versa*. The outliers could owe to a datapoint being acquired slightly out of phase, because the data acquisition device is separate from the device supplying power to run the input signal.

Both the KKMI and KKMG data were used as targets for the simulation output of our streamlined electrochemical/thermal model. The extracted parameter sets of these two new cells were assessed to see how similar they are. The results of these two optimizations are shown in Table 3.2.

All the parameters are within a few percent of each other, which enforces the hypothesis that since the IR video are very similar, the parameter sets extracted from the streamlined model will ultimately have to be similar and can serve as a baseline for the comparison to the degraded cells in the next subsection. $\Delta\bar{S}_{\text{rxn}}$,

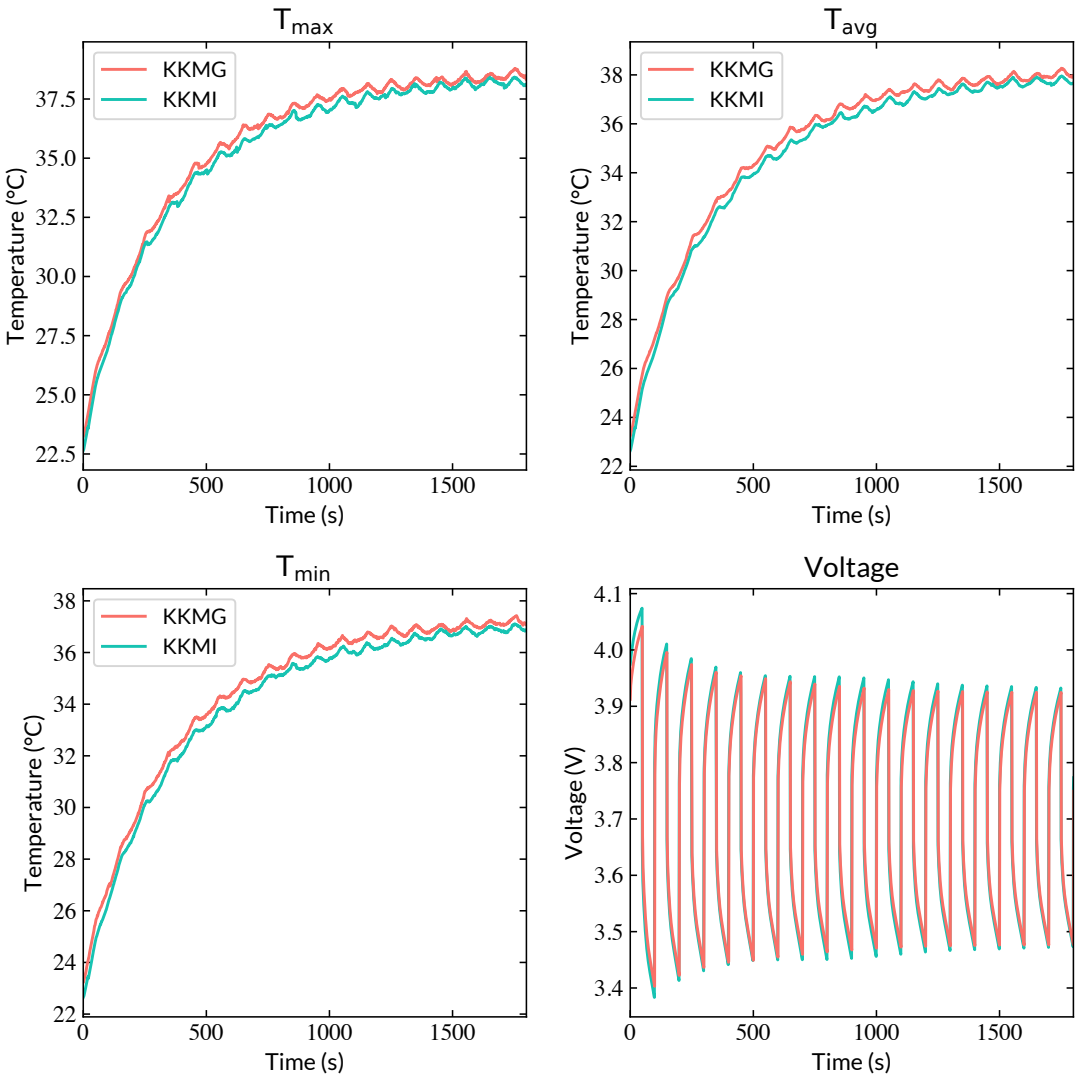


Figure 3.7: Processed $T_{\max}$, T_{avg}, $T_{\min}$, and V data for cells KKMG (red) and KKMI (green).

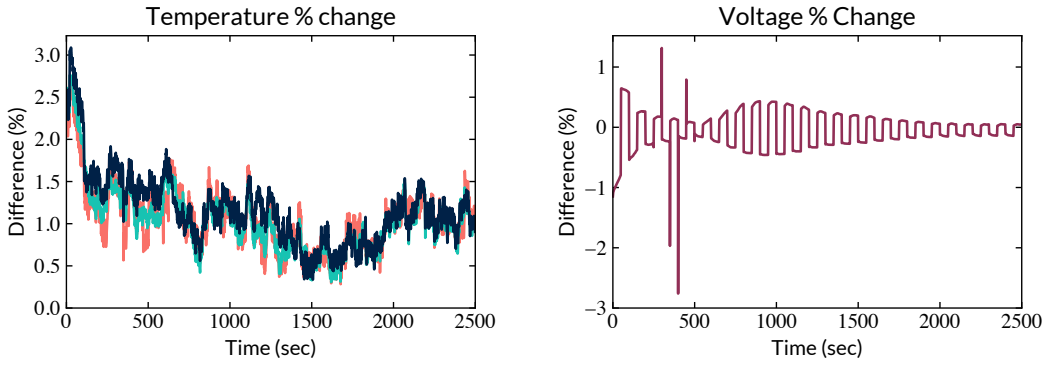


Figure 3.8: Percent change between KKMG and KKMI for the four datasets used to run the parameter extraction.

however, appears to have a large discrepancy between the two extracted parameter values. This is likely an effect of the high sensitivity of the IR camera. In particular, noise at local peaks and valleys in the transient temperature can cause the fitting algorithm to artificially adjust to match randomly occurring spikes or drops. To address this problem the fitting procedure was updated to do an initial fitting only for $\Delta\bar{S}_{\text{rxn}}$, and then comparing the amplitude of the temperature fluctuations in the data and in the simulation output. The resulting value was then fixed for that particular SOC and no longer a part of the list of parameters that get optimized. Having a baseline for the differences between two similar batteries will allow for a better comparison when degraded cells are put through this analysis and comparisons are made between those extracted parameter sets.

3.2.4 Degradation conditions

According to the typical definition, SOH only describes how healthy a cell is based on its current capacity in reference to its capacity when it was pristine. Many degradation mechanisms in lithium-ion cells are not directly detectable *via* regular voltage and current measurements, but they all manifest themselves in a loss of capacity. Whether it is the breaking of electrode materials from mechanical fatigue or loss of active lithium to side reactions, for example, degradation can always be seen as a loss of charge/discharge capacity. Determining which mechanisms are occuring, and their relative contributions to the overall loss of capacity, currently require further analysis through methods such as DVA and/or ICA [42, 44, 45]. Both methods would also require reference half cells to be made by cutting open the cells to salvage active materials to make coin cells with.

To test whether or not the streamlined electrochemical/thermal model can track health degradation through its parameter extraction capability, two cells were chosen to go through extended cycling in various ambient conditions until their discharge capacities were decreased. One cell was cycled inside of a thermal chamber set to 25 °C. The cycling procedure was to charge the cell to 100% SOC by following a CCCV protocol until it reached 4.19 V and the current decayed to a value of 0.16 A

Table 3.3: Degradation overview of the Kokam cells chosen for this study

	KKMB	KKMF
Chamber Temperature (°C)	25	10
Initial Capacity (Ah)	16.82	16.90
End Capacity (Ah)	15.71	15.50
Percent Loss (%)	6.6	8.3
Cycles (#)	1252	875

(C/100); the battery was then discharged until the lower voltage value hit 2.71 V. The constant current portion of the CCCV charge and the discharge were done at 40 A (2.5C based on the cell's nominal capacity), the maximum applicable current of a single parallelizable channel consisting of 8 individual Maccor channels.

The applied charging current was higher than the manufacturer recommended value of 16 A, but precautions were taken by keeping track of cell temperatures and disabling current if the cell got close to 45 °C. The voltage limits as outlined in Table 3.1 were also adjusted to a smaller window as a safety factor. The safety rails were never reached: even under the stressed cycling conditions, both batteries lasted for hundreds of cycles before losing 5% of their discharge capacity. The procedure was repeated for 30-40 cycles and then a capacity check was performed by charging the cell to 100% SOC, following the same CCCV protocol as above and then discharging at a slow C-rate of 0.64 A (C/25). This entire procedure was repeated until the capacity-check capacity reached 95% of the pristine capacity or lower. The second cell went through the same degradation procedure, but the cycling portion was done in an environmental chamber at 10 °C; the capacity check, however, was still done at 25 °C. The initial and degraded capacities are summarized in Table 3.3 and the capacity fade with respect to cycle number data is plotted in Figure 3.9.

Logging the POCV data while performing these intermittent capacity checks allows the usage of DVA to see potential trends in the degradation. We can use these trends to gauge what lock-in thermography can bring to the table, or see if LIT can arrive at similar conclusions in a more efficient manner, since doing DVA requires pseudo open circuit voltage (POCV) data, which can take over 24 hours to acquire.

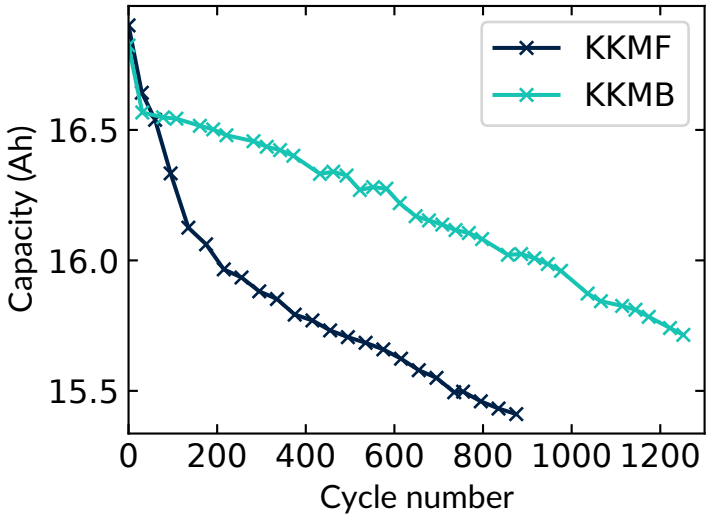
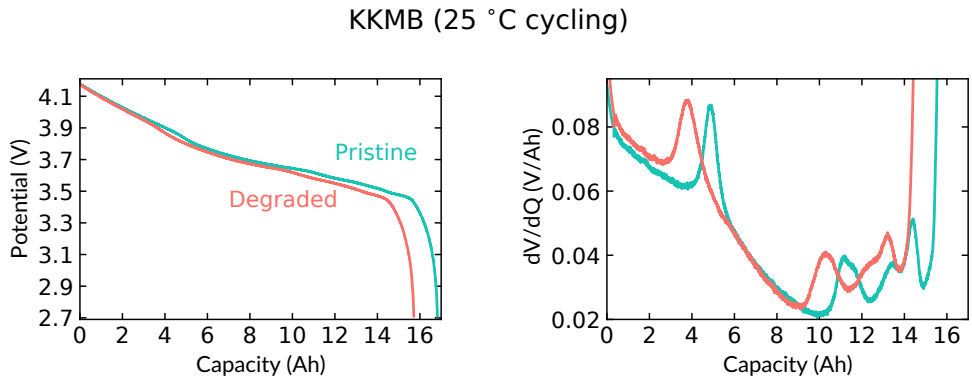
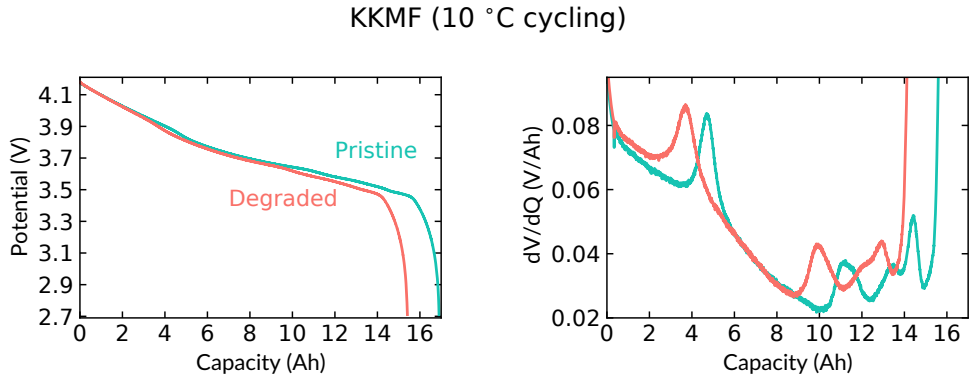


Figure 3.9: Capacity *vs.* cycle number plots for cells KKMB and KKMF. Capacity checks were performed by discharging the battery from full at a C-rate of C/25 to a lower voltage limit of 2.71 V.

In Figures 3.10a and 3.10b, the plots on the left show the POCV data for the corresponding cell in its pristine state in green and the degraded state in red. Without explicit half-cell information, peaks cannot be definitively associated with their corresponding electrodes. But by comparing to literature, it is possible that all noticeable peaks in this plot could be associated to the anode because NMC's DVA analysis could end up having no obvious features [112]. Following analysis from Raj and Keil *et al.* [46, 113], the capacity associated to loss of negative active material is approximately 12 Ah for both health states of both batteries and is approximated by the distance between the leftmost peak to the fully discharged state. While the capacity associated with electrode balancing is the remaining capacity and has a difference of 1 Ah between the pristine state and the degraded state for both batteries. This change in balancing capacity implies that loss of lithium inventory is the major contributor to the capacity loss of this cell [114]. This loss of usable lithium could be due to a variety of side reactions, including solid electrolyte interphase (SEI) growth, lithium plating, or electrolyte decomposition.



(a)



(b)

Figure 3.10: Initial and final POCV curves, and DVA for cells (a) KKMB [25°C cycling] and (b) KKMF [10°C cycling].

3.2.5 Characterizing Degraded Kokam Cells Using Lock-in Thermography

Parameter sets collected for the pristine KKMG cell include 30%, 50%, and 60% SOCs, so the degraded KKMF and KKMB cells will also undergo the same experimental procedure by performing three different types of squarewaves centered around the mean for the three listed SOCs. One squarewave will be high C-rate and low frequency, the second will be low C-rate and low frequncy, and the final one will be high C-rate and high frequency. Results are highlighted in Figure 3.11.

Cell KKMG, KKMB, and KKMF, will now be referred to as the pristine cell, the ambient degraded cell, and the cold degraded cell, respectively. The specific identifiers are no longer necessary as no more comparisons will be made within each of these degradation states. Figure 3.11 shows the change in temperature as the

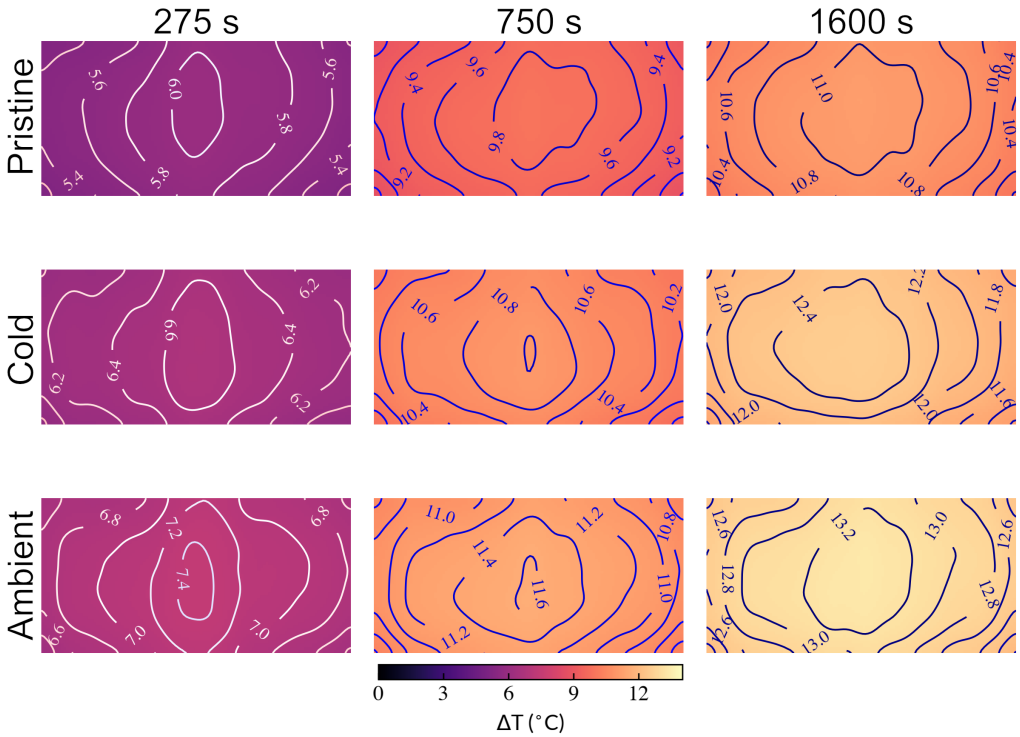


Figure 3.11: ΔT thermograms of a pristine Kokam cell *vs.* cells degraded in a cold 10° C ambient and in a standard 25° C ambient. The three chosen time frames, 275, 750, and 1600 seconds were chosen to represent the initial, middle, and final stages of the squarewave experiment.

experiment progressed: the first column is at 275 seconds, the second column is at 750 seconds, and the final column is at 1600 seconds. For reference, at the time that each of these three experiments were conducted, the temperature in the room was at approximately 23 °C. At every stage of the experiment, the temperature profiles show that the ambient degraded cell has a higher increase in cell temperature across the surface, followed by the cell that was cold degraded.

Both the cold and ambient degraded cells have a slightly different 2D temperature distribution compared to the pristine cell. It seems that heat is preferentially flowing towards the left rather than the right (the left tab in these thermograms is the tab that is connected to the anode). This change in temperature behavior is more apparent when visualized as a difference compared to the pristine cell.

The first row of Figure 3.12 shows the percent change in the temperature distribution of the cold degraded cell when compared to its pristine equivalent,

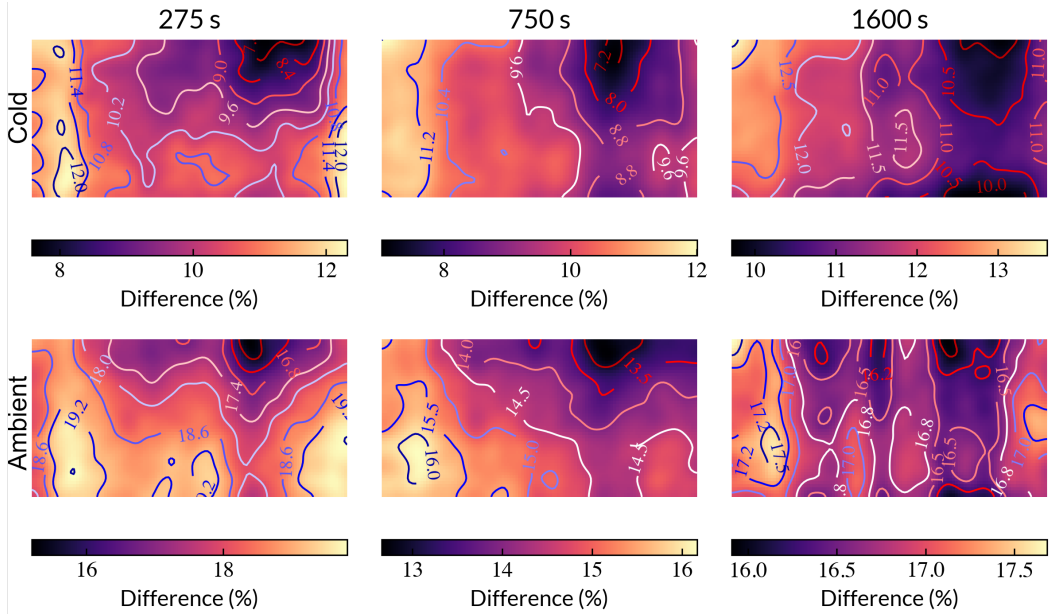


Figure 3.12: Percent change at various time steps comparing the temperature distributions for the pristine cell and the two degraded cells.

the second row is the same but in comparison with the cell that is degraded in standard ambient conditions. This comparison was made at the same time steps that were used in the previous figure and is represented in each column. So, across all three time points of the experiment, the left side of the battery is heating up more when compared to the results in Figure 3.6. The magnitude of the change has increased from approximately 1% to 10 - 20%, in addition within each thermogram, the variation range has increased from about 0.4% to between 3 - 6%, depending on time of the experiment. Some assumptions can already be made based on everything that is known so far. Based off of the DVA analysis, the loss of capacity in both the degraded cells is most likely due to loss of lithium inventory (LLI). This loss is generally attributed to the formation of the solid electrolyte interphase (SEI) layer over time and lithium metal plating. Both of which are more likely to occur on the graphitic anode.

Worth noting is that the hot spot is still determined to be in the center of the battery for all three cells according to the procedure outlined in the previous section. Visual confirmation of a distinct change in the 2D thermal behavior means that there should be a difference in the extracted parameter sets when comparing to

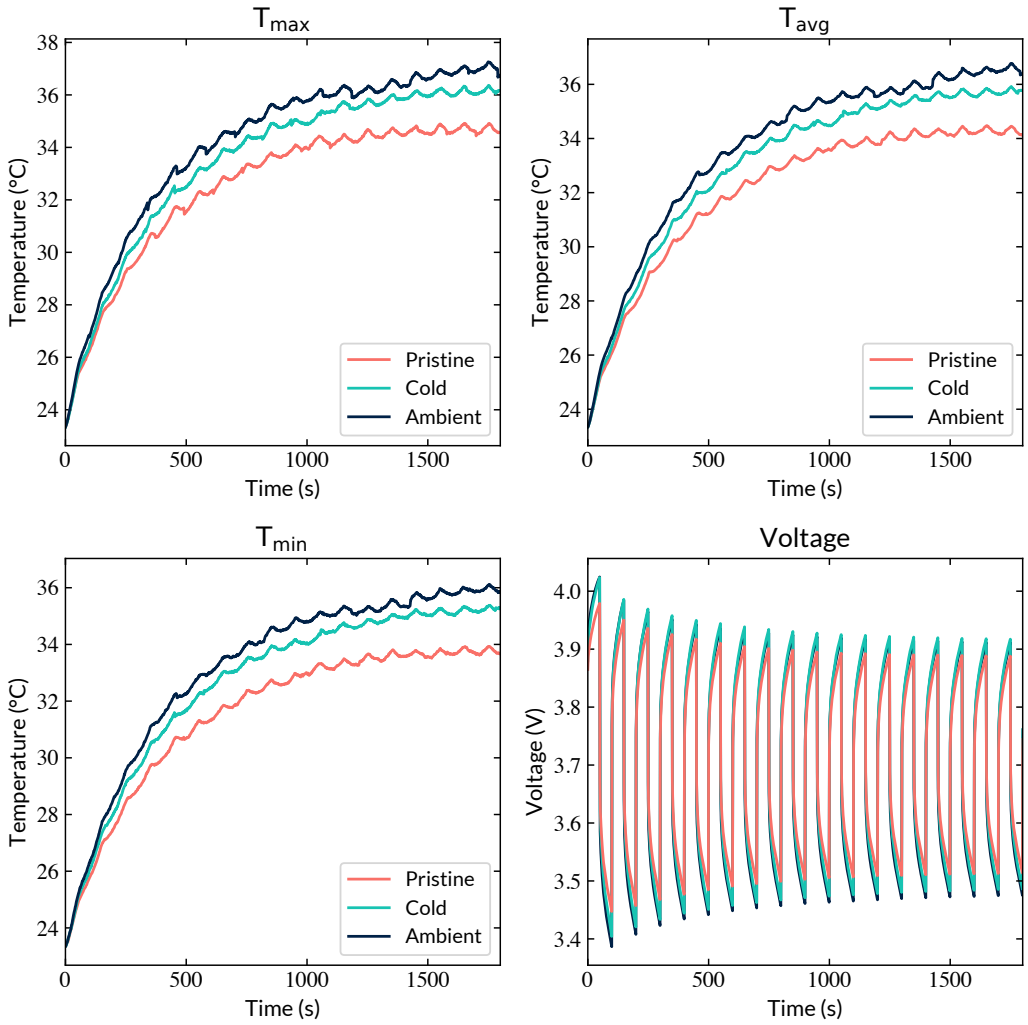


Figure 3.13: $T_{\max}$, T_{avg}, $T_{\min}$, and V data sets for the pristine, cold degraded, and ambient degraded cells.

the parameters obtained in Section 3.2.3. The streamlined electrochemical/thermal model takes the processed $T_{\max}$, T_{avg}, $T_{\min}$, and V time-series data as its input. After processing the IR video and the electrochemical data into the optimization targets for the model, the results are shown in Figure 3.13. Analyzing this result prior to optimization can give us an idea of what parameter changes to expect and also guides intuition of what the initial guesses should be. From this figure, one can see that there is a noticeable increase in steady-state cell temperature in all three temperature signals, and there is also a noticeable increase in the size of the overall voltage envelope. The increase in temperatures means that there is a now a higher

heat generation, which can potentially come from a few sources. One would be the increase in overall resistance in the cell, which is corroborated by the increased size of the voltage envelope. There are several resistances in the streamlined model, so this is something that can be deconvoluted later on. Unfortunately, the model would not be able to optimize for the change in the 2D distribution due to this degradation, which would be an interesting task for a future project. But even so, changes in how and how much heat is generated and conducted even without this level of locality can be revealed in changes in thermal property values in the model, reflected by parameters such as k_{eff} and $C_{p,\text{eff}}$.

Before proceeding with the optimization, DCIR was calculated using the data that was already obtained and Equation 3.1. The experimental procedure for the thermographic analysis involves using a squarewave-current input signal: the first half of a period is essentially the same procedure as the DC resistance check. With a pulse current of 64 A, the pristine cell had a calculated R_{DC} of 3.5 mΩ, the cold degraded cell and ambient degraded cell had values of 4.4 and 4.1 mΩ.

3.3 Results and discussion

3.3.1 Modeling and optimization

Transitioning to a different cell manufacturer for this study required some changes in the COMSOL model to better represent the change in chemistry and geometry. The geometry of the Kokam cell has a wider aspect ratio compared to the portrait orientation of the A123 cell. Cell dimensions were updated based on actual measurements taken from a disassembled pouch cell. Individual layers were counted and measured, and some of these results are compiled in Table 3.4. The geometry change also resulted in a change in the current distribution within the cell. In order to better match the shape of the temperature distribution, a separator region was added as another element that can conduct and hold heat. This also added an extra source of resistance, so that the κ_{liq} parameter does not need to absorb all the resistive changes in the system, as it did in Chapter 2.

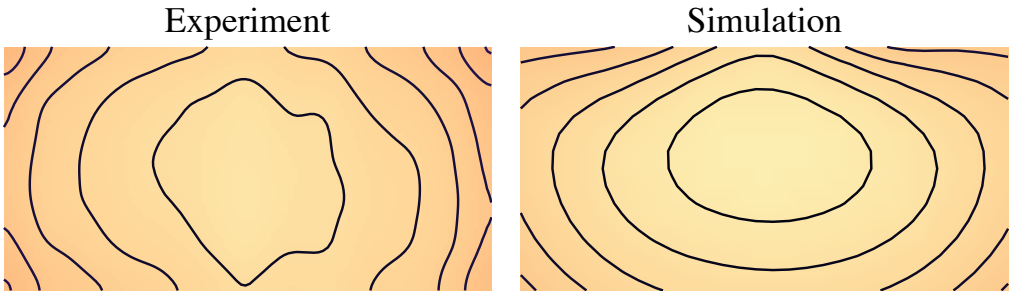


Figure 3.14: Experimental thermogram for Kokam cell undergoing squarewave testing (left) compared to simulated thermogram under the same conditions (right).

As a result of the A123 study, it has been shown that the non-uniformity in temperature is due mostly to the current distribution, which is heavily dependent on cell geometry. In that study, although the simulation temperature distribution matched the experimental output in the vertical direction, the horizontal distribution needed another parameter as tuning the available parameters was not enough to generate this effect. Instead of producing thermograms that looked qualitatively like Figure 2.1, the A123 simulation output generated thermograms that looked like horizontal bands with only a slight curvature. The change from the tall aspect ratio of the A123 LFP cell to the wide aspect ratio of the Kokam NMC cell, was enough to change the current distribution such that simulations better matched the experimental thermal behavior. Figure 3.14 shows the temperature distribution from the IR camera after 1600 seconds of squarewave cycling on the left, and the simulated output at the same time step on the right. Notice that it is still not great because the innermost contour in the experiment resembles a vertically oriented oval, while the simulation is more circular. So the outer shapes matching might be due to edge effects, while the center contour, seems to be impeded by something that prevents heat from spreading horizontally.

The last change to the COMSOL model was that the linear temperature dependence of κ_{liq} from the A123 study was changed to an Arrhenius dependence (Equation 3.2). A linear dependence is a good approximation and therefore substitution for using an Arrhenius dependence within the range of temperatures

that are used in these experiments. However, the voltage signal in this model for this chemistry is very sensitive to small changes in this parameter, particularly in the beginning stages of the experiment. These two parameters are the major contributors to the rate of decrease in the size of the voltage envelope as the experiment progresses. Although this change did not significantly increase the simulation time, it did help the LSQNONLIN algorithm lock the κ_{liq} and $\alpha_{\kappa_{\text{liq}}}$ parameters into stable values faster.

$$\kappa_{\text{liq}}(T) = \exp\left[-\frac{\alpha_{\kappa_{\text{liq}}}}{R}\left(\frac{1}{T} - \frac{1}{T_\infty}\right)\right] \tag{3.2}$$

Outside of COMSOL, the cost functions that the non-linear least squares algorithm was aiming to minimize were also updated. The algorithm was optimizing an error calculation of $\left(V^{\text{m}}_{\text{cell},i} - V^{\text{exp}}_{\text{cell},i}\right) / \left(V^{\text{m}}_{\text{cell},i}\right)$ for the voltage. Although it worked well in general, in this system, it caused the voltage fitting to consistently overpredict the shape of the voltage envelope in order to match the curvature of the polarization, which the model can not replicate well for reasons that will be discussed in a later section. To combat this, an extra function was added to the residual calculation. In MATLAB, the functions findpeaks() and islocalmin() were utilized to find the peaks and valleys of the voltage signal in both the experimental data and the simulation output. The sum of all these errors were then weighted more heavily to compensate for the low number of sampled values (2 datapoints per squarewave period). The minimum temperature residual's weighting was lowered to keep a balance between the temperature and voltage residuals. The minimum temperature residual calculation was adjusted because finding the average temperature and the maximum temperature of the cell were arguably more important. Equation 3.3 was added to generate the fittings in the next section:

$$\min_p \left[2N_{\text{periods}} \times \sum_{i=1}^{N_t} \left(\frac{V^{\text{m}}_{\text{peak},i} - V^{\text{expt}}_{\text{peak},i}}{V^{\text{m}}_{\text{peak},i}}\right)^2 + \left(\frac{V^{\text{m}}_{\text{val},i} - V^{\text{expt}}_{\text{val},i}}{V^{\text{m}}_{\text{val},i}}\right)^2\right] : p^l \leq p \leq p^u. \tag{3.3}$$

Table 3.4: Kokam fixed parameters used in optimization

Parameters	Cathode	Anode	Current collectors	Separator
N_{layers}	50	50	50	50
total thickness (mm)	2	1	0.6875	1
width (mm)	200	200	200	200
height (mm)	100	100	100	100
a_{V} (m^{-1})	1×10^7	1×10^7	-	-
k_{eff} ($\text{W m}^{-1}\text{K}^{-1}$)	fit	fit	40	fit
κ_{sol} (S m^{-1})	50	50	1.5×10^7	-

3.3.2 Fitting and Validation results

Three different squarewaves and three different baseline SOCs were chosen to characterize the two degraded cells for comparison to their pristine counterparts. At each SOC, experiments were run with a high C-rate and low frequency squarewave for model training, and with two modified squarewaves that either had a lowered C-rate or an increased frequency. The modified squarewaves were used to validate the model, which in turn determined the model's predictive capabilities.

The fitting results that determined the parameters that were shown in Table 3.2 are shown in Figure 3.15. The parameter set obtained from the fitting results in the top row were used to simulate two other operating conditions, shown in the second and third rows. All of these data were gathered at a mean SOC of 50%. The two other SOCs' results are highlighted in Figures 3.16 and 3.17. At all three SOCs, the fitting results are quite good, which should be obvious, but it seems that when using the extracted parameter set to predict other operating conditions, there is a trend of a slight underprediction in the voltage signal for the low C-rate validation. This is worse in the 30% scenario, where the validation experiment was done at 2C compared, to the other SOCs where the low C-rate validation was done at 3C. Although this trend was also present in the A123 study as shown in Figure 2.11b, it is more significant in the NMC system. The high-frequency result seems to be accurate, indicating that as long as the C-rate remains relatively high, the model is capable of accurately simulating this cell. That is, it is still possible to draw

something useful from these extracted parameters, knowing that they are effective values that describe a certain cell state with a known limit on operating conditions.

With that said, the extracted parameter sets at every SOC for the three cells in this study are outlined in Tables 3.6 to 3.8. All parameters except one fall within the range of values that were reported in literature or obtained from experiments. Similar to the LFP system, it is κ_{liq} that falls out of the range of values typically reported in literature. Previously, it was possible to explain this phenomenon with conductivity being an effective value and absorbing the changes caused by geometric characteristics such as porosity and tortuosity. But for the NMC system, even with these considerations, this value is considerably lower than the low end of values reported in literature [85, 102, 115–118].

Keeping that in mind, the goal is to see if there are relative changes in parameters that can be tracked across battery health states. The thermal parameters h, $C_{p,\text{eff}}$, and their ratio to each other remained within the variation seen in the pristine comparison. Continuing through the table of parameters, k_{eff} is the first parameter that has a noticeable change between the pristine cell and the two degraded cells. In the previous section, the two pristine cells had values within 1% of each other, but in this comparison, the thermal conductivity has increased between 7.5% to 15% depending on the SOC and which degraded cell was being compared. Despite not perfectly mimicking the 2D temperature distribution, changes in the thermograms that resulted in the processed maximum, average, and minimum temperatures can be observed in this parameter. A higher thermal conductivity should signify a more uniform temperature distribution because the battery can better conduct heat away from the hot spot to other regions of the battery. However, this increased thermal conductivity did not signify that the temperature distribution was more uniform, instead; referring back to Figures 3.11 and 3.12, it can be seen that there is a change in global behavior such that the left side of the degraded cells is noticeably hotter.

Interestingly, $\Delta\bar{S}_{\text{rxn}}$ remained constant. Recall that SOC was set based on a renormalized capacity, so even though the capacity had decreased, being at a particular SOC should mean that both electrodes remain at a similar level of

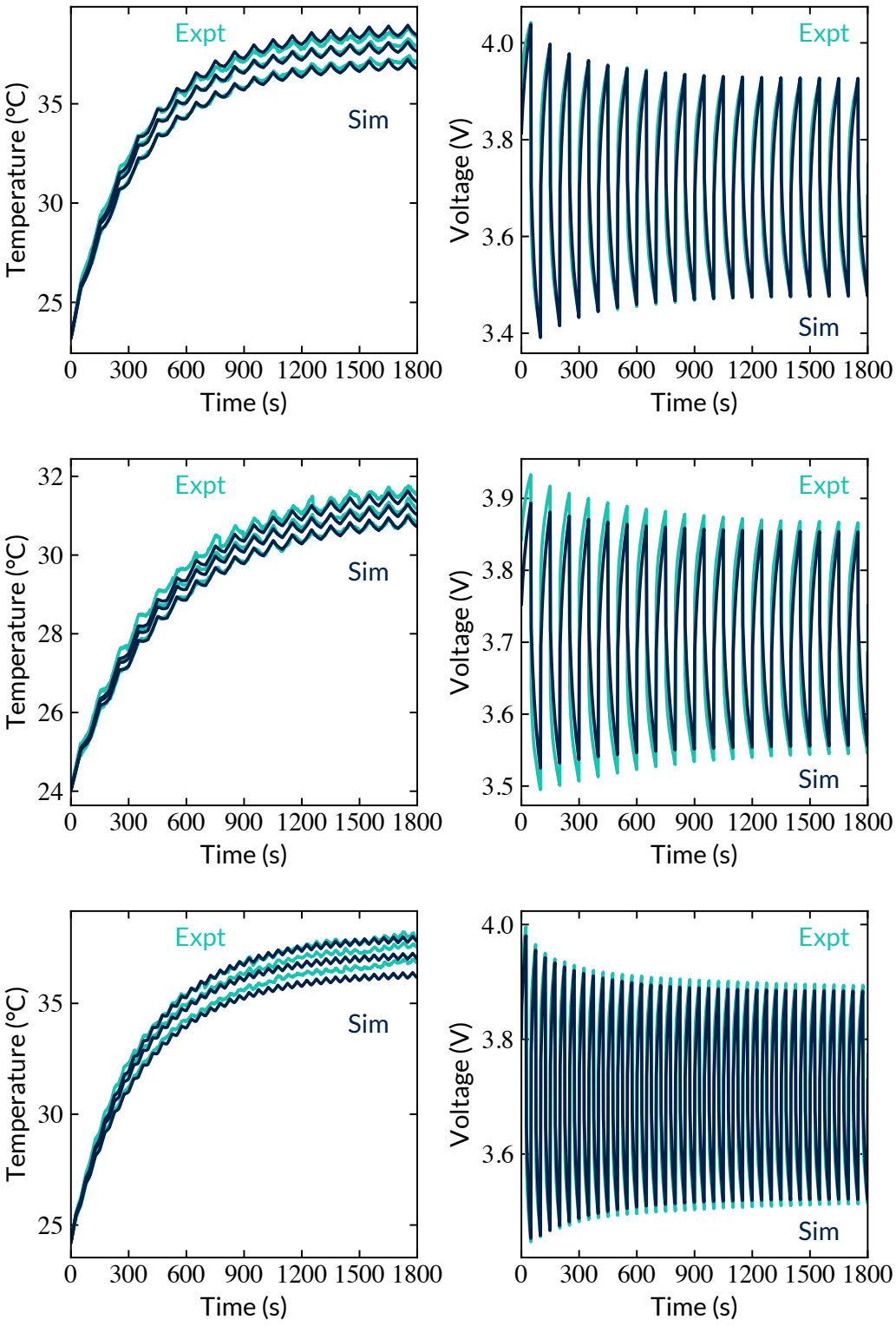


Figure 3.15: Pristine cell (KKMG) fitting results for a 5c100s squarewave in the top row, followed by 3c100s and 5c50s validations at a mean SOC of 50%.

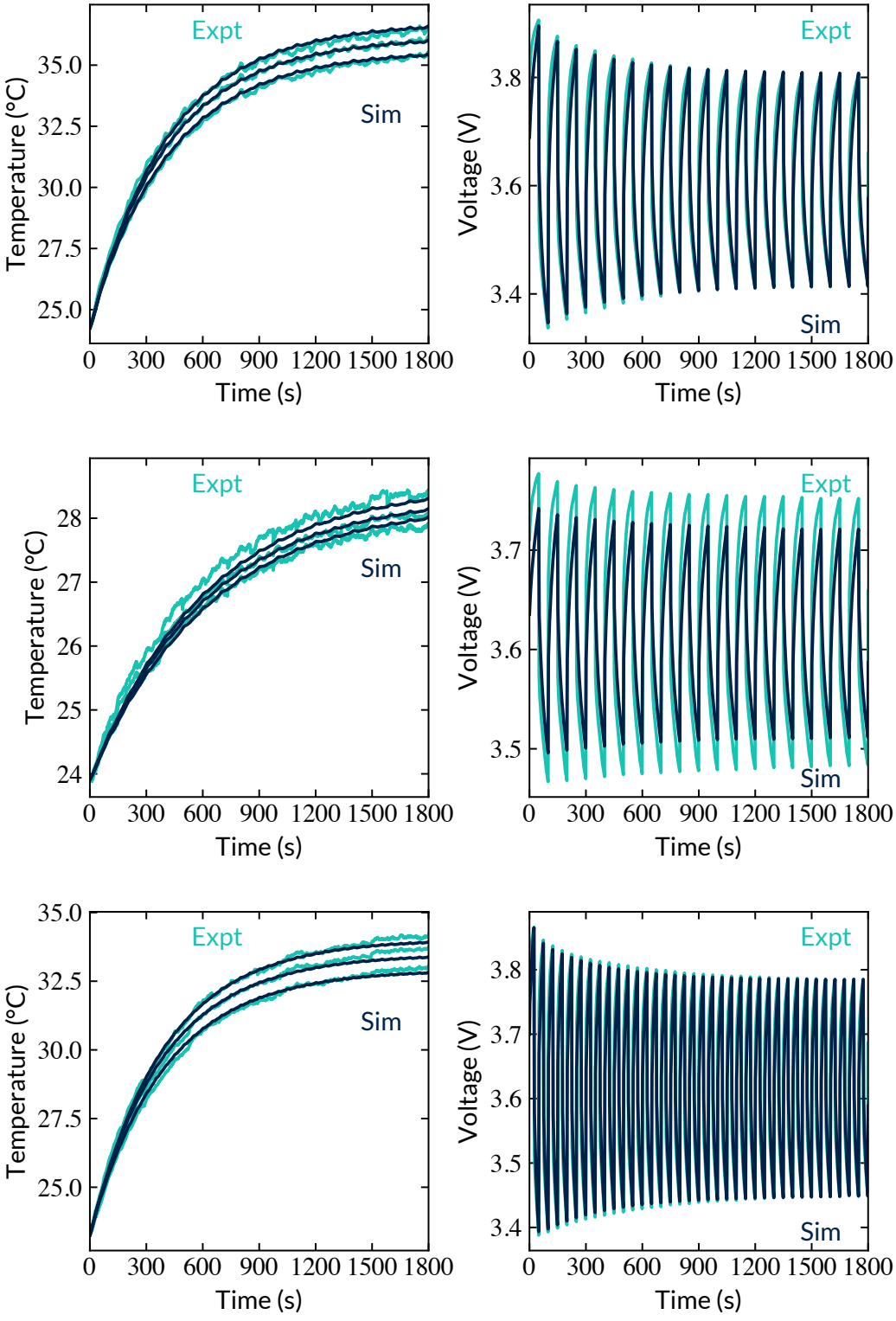


Figure 3.16: Pristine cell (KKMG) fitting results for a 4c100s squarewave in the top row, followed by 2c100s and 4c50s validations at a mean SOC of 30%.

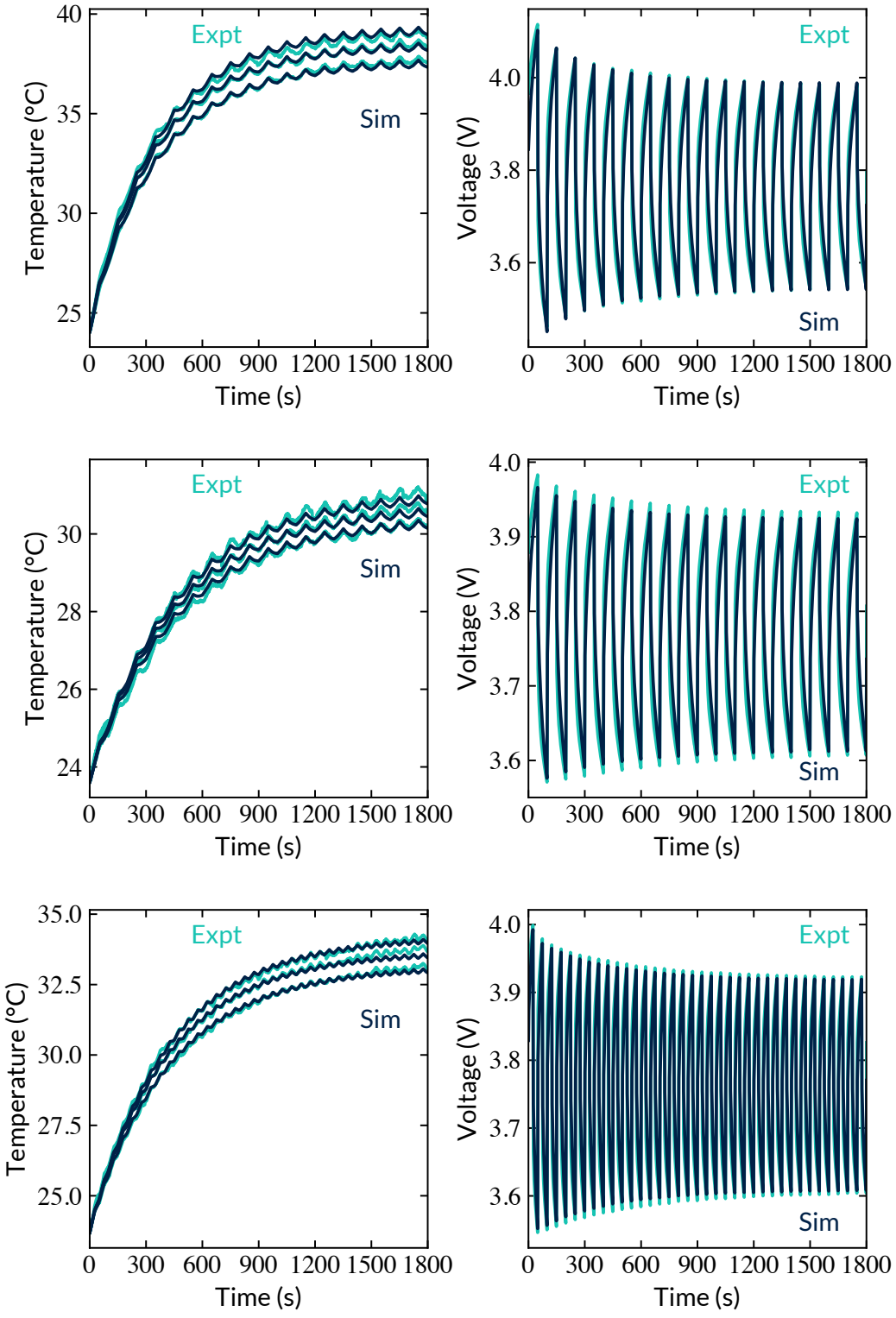


Figure 3.17: Pristine cell (KKMG) fitting results for a 5c100s squarewave in the top row, followed by 3c100s and 4c50s validations at a mean SOC of 60%.

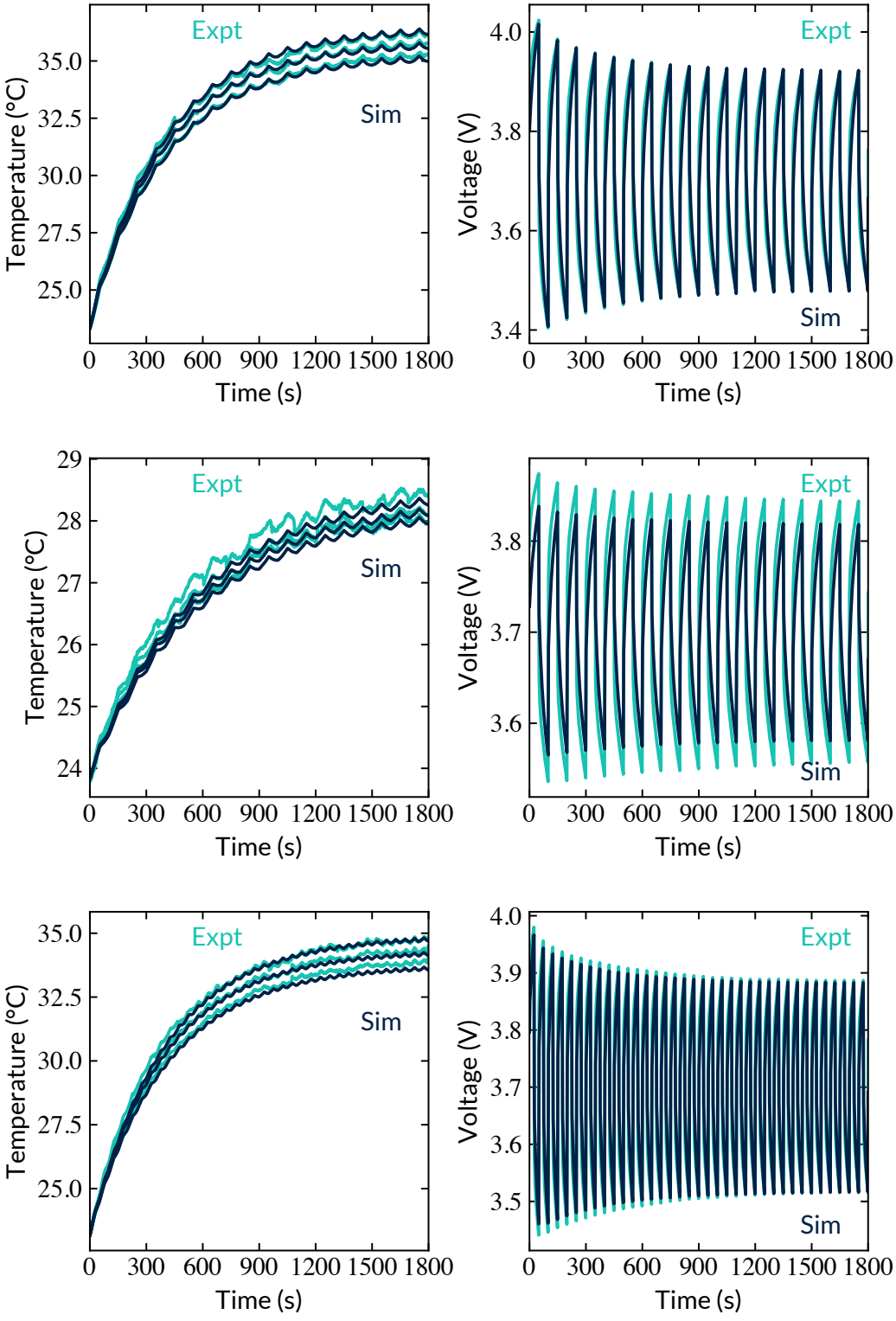


Figure 3.18: Cold degraded cell fitting results for a 4c100s squarewave in the top row, followed by 2c100s and 4c50s validations at a mean SOC of 50%.

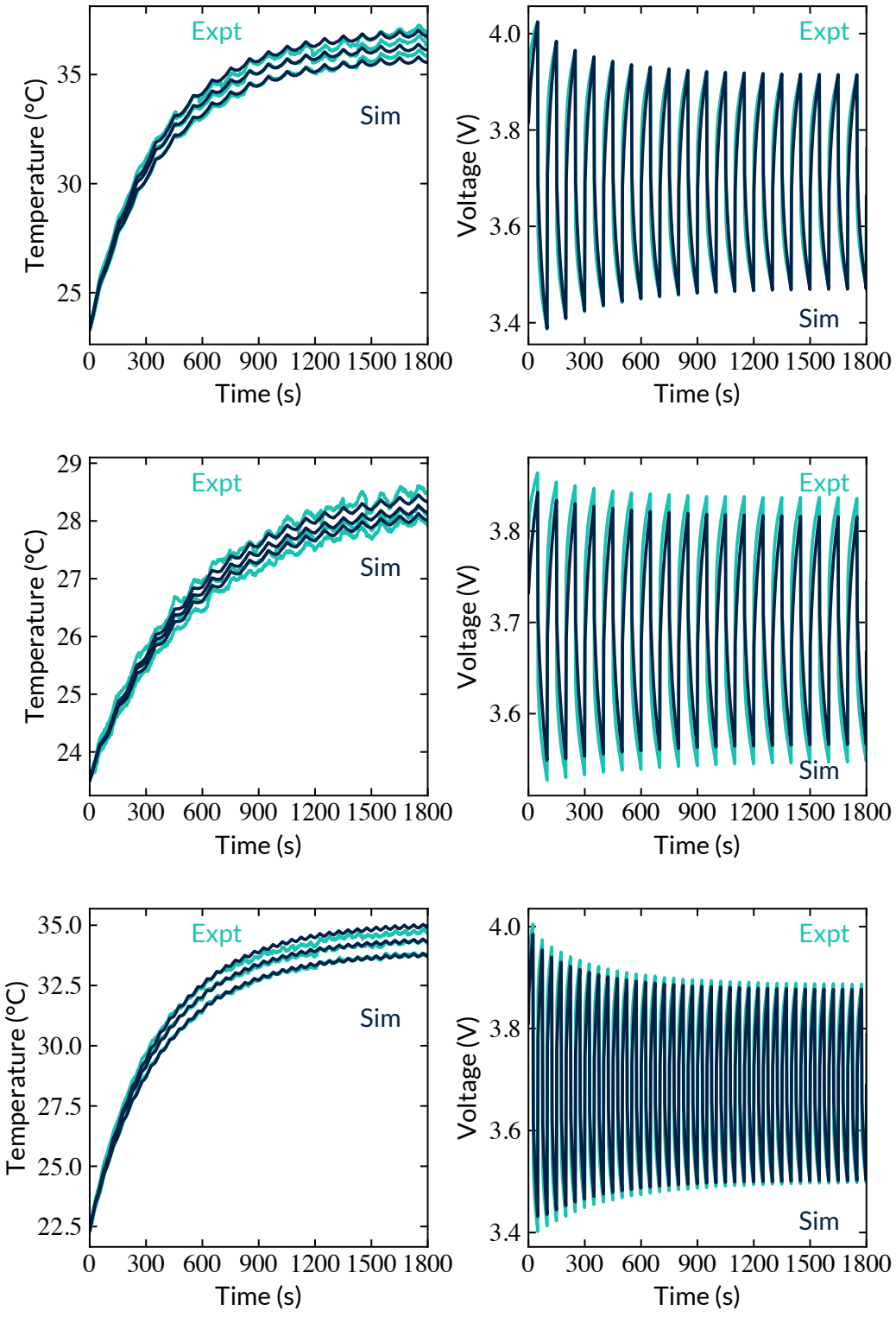


Figure 3.19: Ambient degraded cell fitting results for a 4c100s squarewave in the top row, followed by 2c100s and 4c50s validations at a mean SOC of 50%.

lithiation, so long as there is no relative difference in the degradation rates of the individual electrodes. The similar drift of both half-cell potentials was confirmed in the DVA analysis from the previous section.

Small changes can be observed in i_0^{∞} and E_{i_0}: although the general trend is a decrease with degradation, it is still within the variation observed between two new cells. With $\kappa_{\text{liq}}^{\infty}$ and the associated $\alpha_{\kappa_{\text{liq}}}$, there are more significant changes. There is a ∼15% decrease in $\kappa_{\text{liq}}^{\infty}$ when compared to the cold degraded cell, and up to a 25% drop when compared to the ambient degraded cell.

The OCP slope parameter k_U was calculated by examining pseudo-OCP measurements at C/25 in the small SOC range that the squarewave input signal traverses; in that small range the OCV behavior is approximately linear, and a slope was calculated between the two SOC extrema and reported in the parameter tables. Even though those values are known, k_U was still left to freely change in the data-fitting procedure, and the obtained values were within 10% of the calculated value in all cases. There does not appear to be a significant change in this parameter between pristine and degraded states.

The parameters that did display significant changes in the degraded cells were k_{eff} and $\kappa_{\text{liq}}^{\infty}$ and the results are compiled in Table 3.5. Ionic conductivity in particular showed a larger change in the cell that was degraded in standard ambient conditions. This might be seen as counter-intuitive, since one might expect the cell degraded under a harsher cold environment would experience greater changes. The discrepancy can be explained by the current throughput for both of these cells. Since the end condition of the degradation experiments was a capacity loss, under harsher conditions, this end condition would be triggered relatively faster. In this design of experiments, the cold degraded cell reached the end conditon in approximately a 400 less cycles as the one that was degraded under a 25 °C environment. Under these shallow degradation conditions (∼5 - 10% SOH loss), loss of lithium inventory is the primary degradation mechanism which would manifest as either lithium plating or SEI growth, both of which affect the graphitic anode [119–122], and would affect the ambient degraded cell more purely because of the

Table 3.5: Effective thermal conductivity (W m^{-1} K^{-1}) and ionic conductivity (S m^{-1}) changes at the three different tested SOCs for the pristine and degraded cell comparisons

k_{eff}	Pristine	10 °C	25 °C
30%	1.467	+7.5%	+11.2%
50%	1.497	+15.2%	+12.7%
60%	1.412	+10.9%	-2.4%

$\kappa_{\text{liq}}^{\infty}$	Pristine	10 °C	25 °C
30%	0.012	-16.7%	-25%
50%	0.013	-15.4%	-23.1%
60%	0.014	-14.3%	-21.4%

higher usage [123, 124]. The fact that these two phenomena involve the anode could also explain why Figure 3.12 shows such significant changes to the left side of the battery, as that is the tab at which all the anode layers are joined together.

3.4 Conclusions

The streamlined thermo-electrochemical model was adapted to simulate a new battery with a different battery chemistry (NMC/Graphite) and a different geometry. The model was able to match the experimental maximum, average, and minimum temperatures, as well as the voltage data for Kokam 16 Ah NMC pouch cells with appropriate parameter values. State-of-health tracking capabilities were tested by tracking the parameter sets that were extracted from the temperature and voltage fitting at different points in the cells' operating histories. Despite not having degradation mechanisms explicitly inserted into the model, there are noticeable changes in the extracted ionic and thermal conductivity parameters from degraded cells. There is a 7.5% to a 15% increase in thermal conductivity between the pristine cell and the two degraded cells. The increase in thermal conductivity parameter was the result of the change in how the cell is generating heat, specifically, in the degraded cell, the left side of the battery is significantly hotter than it was when compared to a battery in its pristine state. The left side tab is the negative terminal of the cell and it is where all the negative current collectors are welded together. Assuming the primary degradation mechanism to be loss of cyclable lithium, it would make sense that there are side reactions occuring on the negative electrode. There is also a 15 to 25% drop in the ionic conductivity parameter. When comparing the voltage data between the pristine and degraded states, the voltage

Table 3.6: Pristine Kokam cell parameters

Parameters	Units	30%	50%	60%	Literature/Measured Value
h	W m^2 K	17.094	19.473	18.582	3 - 25 [56, 105]
$C_{p,\text{eff}}$	J m^{-3} K^{-1}	3.445×10^6	3.503×10^6	3.531×10^6	2 - 3.5×10^6 [56, 57, 103]
k_{eff}	W m^{-1} K^{-1}	1.467	1.497	1.412	0.4 - 2.0 [56, 103]
ΔS_{rxn}	mV K^{-1}	-0.013	0.065	0.075	|0 - 0.3| [36, 90]
i_0^∞ at 25 °C	A m^{-2}	1.043	0.902	0.899	0.1 - 1.0 [117, 125]
E_{i_0}	KJ mol^{-1}	29.605	17.035	21.317	20 - 60 [117, 125, 126]
$\kappa_{\text{liq}}^\infty$ at 25 °C	S m^{-1}	0.012	0.013	0.014	0.1-1 [85, 102]
$\alpha_{\kappa_{\text{liq}}}$	KJ mol^{-1}	31.816	31.087	34.593	10 - 20 [117, 118]
					30%: 0.535
k_U	V	0.501	0.470	0.614	50%: 0.476
					60%: 0.677

Table 3.7: Cold degraded Kokam cell parameters

Parameters	Units	30%	50%	60%	Literature/Measured Value
h	W m^2 K	18.776	18.439	18.775	3-25 [56, 105]
$C_{p,\text{eff}}$	J m^{-3} K^{-1}	3.354×10^6	3.524×10^6	3.487×10^6	2 - 3.5×10^6 [56, 57, 103]
k_{eff}	W m^{-1} K^{-1}	1.577	1.725	1.566	0.4 - 2.0 [56, 103]
$\Delta\bar{S}_{\text{rxn}}$	mV K^{-1}	-0.013	-0.065	-0.075	|0 - 0.3| [36, 90]
i_0^∞ at 25 °C	A m^{-2}	1.169	0.871	0.844	0.1 - 1.0 [117, 125]
E_{i_0}	KJ mol^{-1}	34.243	19.802	21.698	20 - 60 [117, 125, 126]
$\kappa_{\text{liq}}^\infty$ at 25 °C	S m^{-1}	0.010	0.011	0.012	0.1-1 [85, 102]
$\alpha_{\kappa_{\text{liq}}}$	KJ mol^{-1}	23.934	29.293	34.495	10 - 20 [117, 118]
k_U	V	0.509	0.491	0.649	30%: 0.499 50%: 0.499 60%: 0.680

Table 3.8: Ambient degraded Kokam cell parameters

Parameters	Units	30%	50%	60%	Literature/Measured Value
h	W m^2 K	17.692	17.817	17.256	3-25 [56, 105]
$C_{p,\text{eff}}$	J m^{-3} K^{-1}	3.268×10^6	3.309×10^6	3.161×10^6	2 - 3.5×10^6 [56, 57, 103]
k_{eff}	W m^{-1} K^{-1}	1.636	1.687	1.377	0.4 - 2.0 [56, 103]
$\Delta\bar{S}_{\text{rxn}}$	mV K^{-1}	-0.013	-0.065	-0.075	|0 - 0.3| [36, 90]
i_0^∞ at 25 °C	A m^{-2}	1.017	0.790	0.697	0.1 - 1.0 [117, 125]
E_{i_0}	KJ mol^{-1}	35.274	24.188	35.435	20 - 60 [117, 125, 126]
$\kappa_{\text{liq}}^\infty$ at 25 °C	S m^{-1}	0.009	0.010	0.011	0.1-1 [85, 102]
$\alpha_{\kappa_{\text{liq}}}$	KJ mol^{-1}	23.124	24.745	27.748	10 - 20 [117, 118]
k_U	V	0.554	0.470	0.661	30%: 0.545 50%: 0.457 60%: 0.671

polarization is larger in both the charges and discharges as a result of squarewave cycling, creating a larger voltage envelope. This increase is a result of increased internal resistances and the decreased conductivity parameter is a reflection of that, it also corroborates with the higher average cell temperatures in the degraded cells.

Being able to detect these changes despite some deficiencies, such as the unrealistically low ionic conductivity value, means that the health state is best tracked by examining the parameters' relative changes, rather than their absolute values. It is likely that closer matches to experimental data and literature parameters could be attained by returning some of the phenomena that have been stripped out back into the streamlined model. The shortcomings in this model can be analyzed to determine the best choice for what should be added back in to achieve better accuracy while maintaining the computational speed of the parameterization process.

4

Electrochemical/Thermal/Mechanical Measurements

4.1 Introduction

Both the primary mechanisms of lithium insertion and removal and their secondary effect of heat generation can induce volume changes in electrodes that then propagate to larger length scales. Battery active materials such as NMC and graphite have layered crystalline structures, intercalation and deintercalation of lithium ions in to and out of these layers causes the distance between them to increase and decrease respectively [127]. The resulting heat from the electrical load used to drive intercalation can also cause all the components of the battery to go through a thermal expansion, although the amount of expansion varies between the different types of active and inactive materials within the battery cell. This chapter will discuss all the electrochemical, thermal, and mechanical processes that occur and how they affect each other.

Previous work has shown that measurements of mechanical stress and strain can serve as good indicators for important cell metrics, including SOC and SOH [21, 22, 128]. Measuring stress by using force sensors on cells compressed between endplates is a convenient way of measuring mechanical effects, but certain things such as the preloaded stress are extra control variables that need to be considered.

Measurements with endplates also aggregate the behavior across the entire cell into one measurement, removing locality. The work by Cannarella *et al.* and Samad *et al.* has shown that SOC generally tracks with the stress measured in their respective rigs. This is most likely due to stress being a direct measurement of the graphite lithiation state, due to the volume change mentioned before. Irreversible changes were used to characterize an altered health state, arising from things such as separator deformation and SEI formation. What these studies tell us is that despite however much compression was initially applied to the battery pack, the cells are consistently experiencing much higher levels of stress in operation, and it can have an effect on cycle life. Small amounts of compression is supposed to help with electrochemical performance, but there is an limit as these groups have shown, since excessive stresses can also promote detrimental side effects.

Going into strain measurements, the work of Bauer *et al.* and Mohtat *et al.* used linear variable differential transformer (LVDT) sensors to measure displacement by placing the tip of the sensor on a local area or attaching it to an endplate to generalize the whole surface to a single value [28, 32]. Features in the strain measurement were used in conjunction with voltage data to make parameter estimations with better confidence at shallower depths of discharge compared to the sole use of voltage data from similar experiments. Mohtat *et al.* was also the only group mentioned in this chapter that studied a LFP/graphite system. Showing the usefulness of a mechanical measurement by providing a clear expansion signal when, in this system, cell voltage would just be a plateau making SOC hard to estimate. It is worth noting that the endplate/LVDT sensor method of strain measurement does involve the application of a small pre-load, which comes from the spring in the LVDT sensor and also the endplate's weight. Which might have resulted in the work of Rieger *et al.*. They implemented a non-invasive strain measurement using a laser scanning rig, and also a 3D scanner to probe strain behaviors in lithium-ion pouch-cell batteries, displaying the capabilities of laser dilatometry for capturing non-uniformity in strain distributions [29, 59].

It is worth mentioning that in long term operation, pouch cells are placed under some amount of preloaded compression, which is supposed to promote better contact between the layers and prevent delamination. Wünsch *et al.* [129] studied the SOH of a battery in terms of impedance and remaining capacity for cells under different types of compression. This study showed reduced cycle life of cells that were allowed to freely expand and contract compared to the cells that some sort of compression applied. Experiments involving degradation over time would best be done with stress measurements as it would better emulate how these cells would be used in real-life applications. But for cell characterization, strain measurements would still be a valid method as it can be used to describe a current snapshot of the battery's state. It can also see larger signals for things such as gas formation [130].

Much of the past work on mechanical measurements has focused on cells operated at low ($<$ 1C) C-rates in order to make thermal effects negligible. At low C-rates, stress and strain measurements are often compared to techniques such as DVA and ICA. Much like the stress measurements in the next section, in all the previously mentioned works where temperature effects have been explored, the thermal response was studied in isolation by adjusting temperatures in an environmental chamber and waiting for the cell temperature to equilibrate before taking stress or strain measurements. The Rieger and Bauer groups used this method to calculate a thermal expansion coefficient. Based on their calculated thermal expansion coefficients and with their 1C current, the maximum surface cell temperature increase was $\sim$2.5 °C, which resulted in an expansion that was undetectable by their respective sensors, but also should only account for 1 to 2% of the total expansion that they observed. So, under these circumstances, it should be reasonable to neglect thermal effects.

In situations where higher C-rates are to be used, it will be important to be able to measure temperature, strain, and voltage simultaneously, as SOC and temperature effects can have varying impact on mechanical behavior. Being able to use higher rates would open up more diagnostic and capability testing, provided that we can somehow deconvolute the two effects. Stress measurements in experiments that involve the use of endplates for compression make coupled

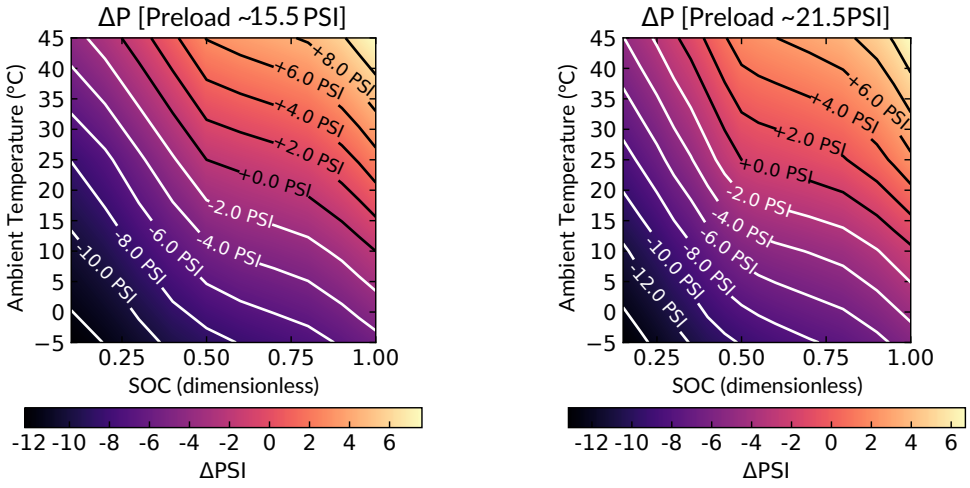
temperature measurements almost impossible to obtain. Non-contact methods like IR thermography are blocked by the endplates; moreover, the contact with endplates affects heat conduction, introducing noise in measurements. Although it is possible for thermocouples to be used, the sources typically used for preloading could cause the thermocouple joints to be crushed. Strain measurements can allow for use of thermocouples without the fear of rupture, but strain measurements involving contact sensors occupy surface area, limiting thermocouple placement options. So, an attempt at using the non-contact method of laser scanning will be implemented with the addition of an IR camera/sensor to capture thermal and mechanical phenomena in parallel. The novel testing protocols put forward here provide new insights into thermomechanical coupling, and can be used for rapid diagnostic tests.

4.2 Equilibrium stress measurements

Prior work has been done in trying to characterize the electrochemical/mechanical coupling in prismatic cells. An experimental set-up created in collaboration with colleagues at the University of Michigan was used for this experiment. Three prismatic cells from a Ford hybrid vehicle were placed in between two garolite end plates and bolted down with four force sensors on each corner. The four corners were then tightened to a point where all four sensors read the same assigned force, either 230 lb or 320 lb. The force used to compress the cells in the original pack was 230 lb and was recreated to emulate pack conditions to see its effects. 320 lb was used to see how a higher level of compression can affect the resulting stress evolution. The preload was applied while the batteries were at 50% SOC and in an environmental chamber set at 25 °C.

Stress effects were induced by either changing the cell SOC (by charging or discharging) or by changing the ambient temperature of the environmental chamber. In an attempt to remove path-dependent dynamical effects (*e.g.* C-rate at which SOC is changed and the heating rate of the thermal chamber), measurements were performed in open-circuit thermal equilibrium. For example, to change the SOC, the galvanostatic intermittent titration technique (GITT) was used, where a

constant current was applied to the cell for a fixed period of time, followed by a rest at open circuit; then, after a few hours, when the force sensors stabilized, the stress was recorded as the measurement for that SOC/temperature combination. Measurements were performed as follows: after the preload was applied, the cell was charged to 100% SOC and then discharged in steps of 5 to 10% until 10% SOC for the 230 lb pre-load experiment, and until 15% for the 320 lb pre-load experiment. The 100% SOC was always established at the reference temperature, 25 °C. The overall protocol (with SOC referenced to 25 °C) was repeated at ambient temperatures of, 45, 10, −5 °C, as well as 25 °C. Each full discharge at the various temperatures took about a week to complete, so for four temperatures, each experiment took about one month. Therefore, since there were two preloads, the entire experimental plan took two months to complete.



(a) **(b)**

Figure 4.1: Stress response of prismatic cells after applying a change in SOC or a change in ambient temperature. (a) Represents the stress response under a preloaded stress of 15.5 PSI and (b) represents the stress response under a preloaded stress of 21.5 PSI.

Each preload experiment can be summarized in the form of a contour plot, shown in Figure 4.1. Each contour line shows an increase in 2 PSI worth of pressure, the vertical spacing between each contour tells us how much of a temperature change is required to induce that 2 PSI worth of pressure, and the horizontal

spacing between contour lines presents the SOC change required to induce the same gauge stress. At close to ambient conditions with SOCs of less than 50%, one can cause a 2 PSI increase in pressure by increasing the temperature 5 °C or by increasing SOC by 10%. After going above 50% SOC, another 5 °C change will cause another 2 PSI increase, but will require a 20% SOC increase to do the same. This effect is even greater at colder temperatures.

The temperature observation is interesting because 5 °C is not a large change in ambient temperature, the northeast region of the United States can easily have temperatures that span 10 to 15 °C in a single day. The 2 to 4 PSI increase is a relatively small amount but over time could corroborate with the hypothesis of thermal cycling leading to mechanical fatigue. In the work of Cannarella *et al.*, a cell that was cycled under a "low" stack pressure was experiencing a 30 PSI change in pressure from doing full charge/discharge cycles. So a thermal cycle of 10 °C is causing the cell to experience something similar to what a 13% depth of discharge cycle would cause.

The jump in requiring a 20% SOC increase to induce an additional 2 PSI increase at 50% SOC is also interesting because it shows one of the stages of lithium insertion into the graphite anode. The large amount of charge necessary to induce a new change could indicate that lithium is intercalating into a new phase. Graphite anodes have distinct phases in their lithiation states that correspond to the plateaus in their OCV curve *vs.* a lithium metal reference. The contour lines have 2 places where their slope changes when moving horizontally, which could give insight into the balancing of the cell or which stage lithium prefers to be intercalated without having to harvest materials for half-cell testing.

From purely an SOC standpoint, the extreme low and high end of the battery charge state have the highest impact in stress evolution. And from a temperature standpoint, each degree increase at a higher temperature (>25 °C) nets a greater pressure increase than at lower temperatures. Increasing the preloaded stress does not appear to cause any change in trends; it just increases the overall magnitude of the stress response.

4.3 Experimental setup for laser dilatometry

4.3.1 Frame update

While using force sensors is an easy way of measuring of the mechanical consequences of charging and discharging the battery, it is a bit limiting in terms of how to incorporate temperature measurements. As mentioned before, neither thermocouple arrays nor infrared thermography are viable with the setup used to do the equilibrium stress measurements. Therefore, we explored modifications of the thermography experimental setup described in Chapters 2 and 3, as there are a variety of optical displacement sensors that can measure the distance of an object from the sensor. If two sensors are placed in front of and behind the battery, with the distance between them known, then the thickness of the battery can be calculated. To this end, two laser displacement sensors were purchased to facilitate non-invasive strain measurements. Details about the sensors are provided in the next subsection.

The unistrut frame from Chapter 2 unfortunately could not be used because it did not afford enough space to accommodate the displacement sensors. The frame was adapted to free up the area around the front and back surface of the battery. During the course of this, the frame for lock-in measurements of battery properties has gone through multiple iterations. The one that will be described below is the latest one and is capable of accommodating the collection of data from our IR camera and our custom built 2D laser scanner. Aluminum T-slot extrusions (Misumi-EC 6 series) were chosen because they are easy to assemble and connect to other auxiliary components. Figure 4.2 shows the number and length of T-slot extrusions that were used for the rigs and two views of the built frame to show how the pieces are connected. The vertical pieces are 350 mm long and most of the horizontals are 300 mm long. Since the cross-sectional dimensions of the extrusions are 30 mm by 30 mm, there needs to be a single piece that is 240 mm long to fit in between two other pieces. Cell holders from Figure 3.3 are attached to this frame by loading in spring nuts into the slots and bolted through the cell holders.

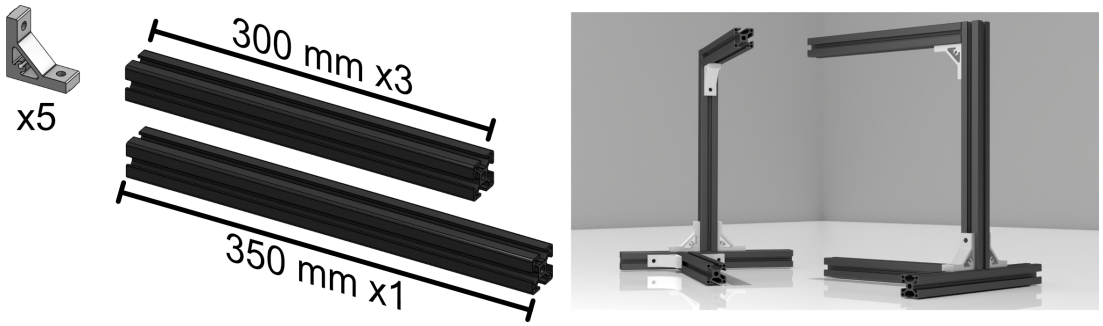


Figure 4.2: Updated T-slot frame to hold cell holders in an upright position with components and dimensions

4.3.2 Laser Profilers

Micro-Epsilon ScanControl profilers (LLT 2900-10/BL) were the displacement sensors chosen for this experimental study. These units have 1280 points per profile with a maximum measurement rate of 100 Hz. The sensor is also capable of detecting changes in distance as small as one micrometer. The profiler fires off a laser that is 9.6 to 10.4 mm wide depending on its distance to the target. For example, a 52.5 mm distance creates the 9.6 mm beam, and a 60.5 mm distance creates a 10.4 mm beam. The receiving optics takes the reflection and projects it on to their sensor and the intensity is converted into a distance using triangulation. To move the two-sensor array in a repeatable manner, the lasers were screwed in to a custom designed holder and bolted to a 2-axis CNC. The schematic drawings of the laser holders are shown in Figure 4.3. The adapter plate, arms, and laser mount were all made of aluminum. The vibration dampening foam are cut pieces of sorbothane from Thorlabs, Inc. The parts are assembled in a manner shown schematically in Figure 4.4b

Two motorized stages were used to make a 2-axis CNC. The horizontal stage is a belt driven stage with 400 mm of accessible distance while the vertical stage is a ball-screw driven stage with 300 mm of movement. The difference in linear actuators is due to a speed requirement on the horizontal axis and a supported weight requirement on the vertical axis. The belt-driven horizontal stage allows for a faster top speed with a small sacrifice in the precision of its movement due to backlash (because of the stretching of the belt). The vertical stage cannot be

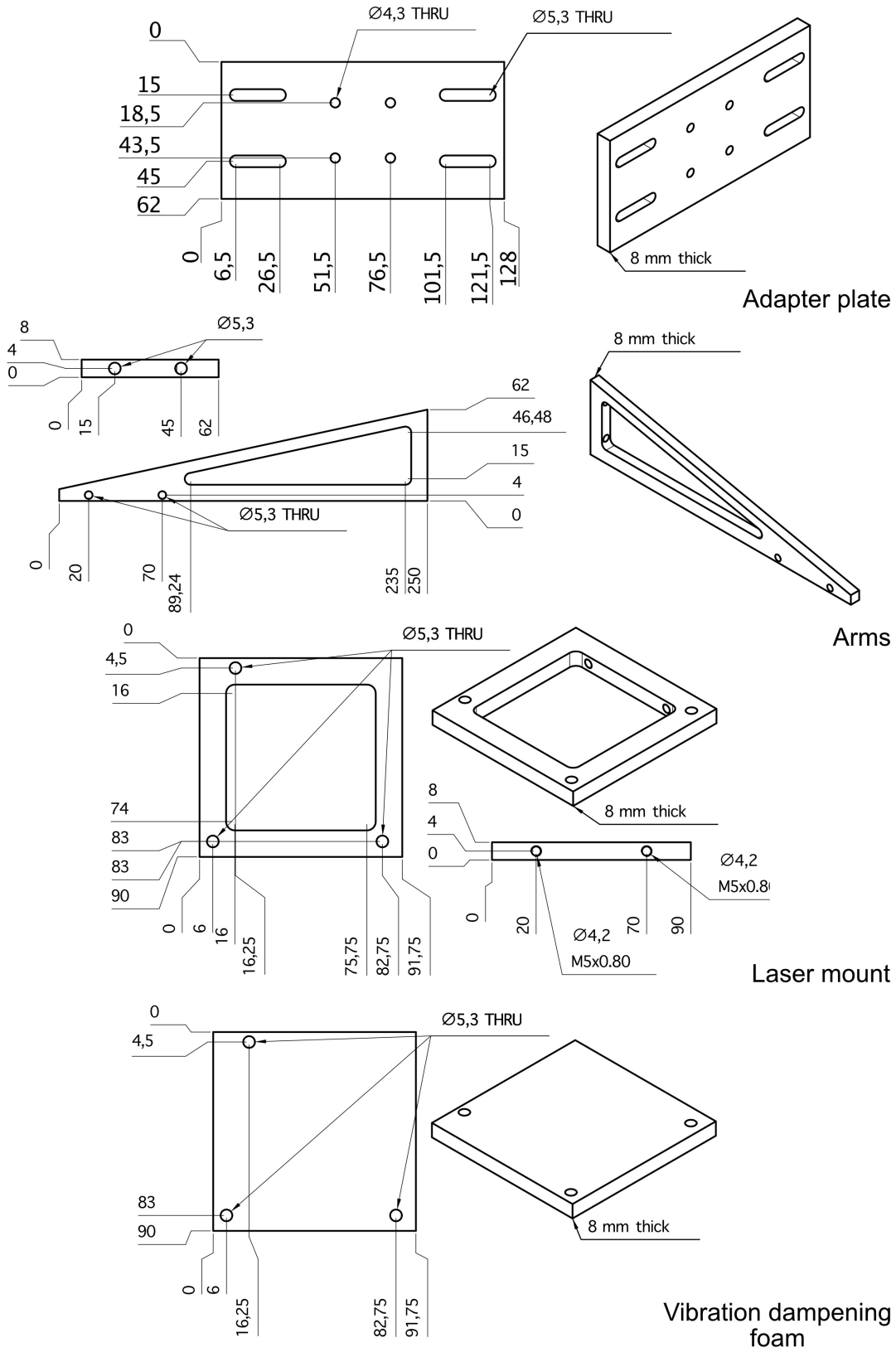
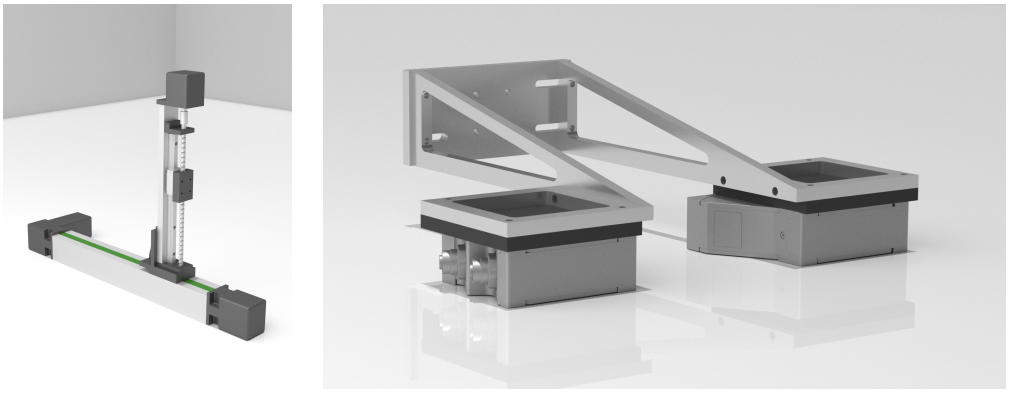


Figure 4.3: Drawings for various components used to assemble the holder used to carry the laser profilers



(a) **(b)**

Figure 4.4: (a) Belt and ball screw driven motorized stage configuration and (b) completed laser assembly. The four holes of the adapter plate are used to bolt the entire assembly in (b) to the vertical stage's platform.

belt-driven, as the weight of the laser assembly would pull the stage down when there is no current to seize the motor. Another piece of sorbothane foam was placed in between the horizontal and vertical stages with the aim of dampening vibrations that accompanied motion of the laser stages. The stages are controlled *via* custom firmware on a microcontroller (Sparkfun Redboard/Sparkfun Pro Micro) and two stepper motor drivers (Sparkfun Autodriver v13). The stepper motors are daisy chained together to eliminate the need for two microcontrollers to independently control each stage. The wiring diagram to achieve this is shown in Figure 4.5.

The distance per full step of the stepper motor was calibrated by moving the horizontal stage 100 steps back and forth 10 times and measuring the distance travelled. This was repeated for 200 and 300 step movements to get an average calibration that works across the entire stroke distance of the stage. The vertical stage was calibrated in the same way. Ultimately, the result was 1.416 steps per mm for the horizontal stage and 40.115 steps per mm for the vertical stage. Microstepping was also implemented to make the movements smoother, and both stages are set to 16 microsteps per full step. Custom firmware was written in the Arduino programming language and the stages were controlled through a dashboard coded in python using the plotly dash library.

An optical breadboard with sorbothane feet was used as the base for all components of the test rig. The complete set up is rendered into an image shown in Figure 4.6. The 2-axis stage set up was held in place using optical table clamps and the T-slot extrusion frame was directly bolted into the optical breadboard. The camera is off the breadboard due to minimum focus distance constraints, but it does not need to be on the board as the IR camera footage is not affected by general vibrations.

4.4 Scanning laser dilatometry with IR camera measurements

As a proof of concept, an experiment that would most likely generate the largest signal for the lasers would be a fast charge CCCV protocol. The mechanical information collected would be a combination of the intercalation effects plus the thermal expansion/contraction effects induced by the high amperage. Prior to doing such a test, the laser sensors' exposure times have to be calibrated. MicroEpsilon suggested targetting a sensor saturation of 80% to avoid missing out on data due to underexposure or overexposure. The painted side of the battery requires a longer exposure time for the lasers, due to the matte paint's characteristic of minimizing reflections. The front laser, which records distance from the painted side of the battery, typically requires an exposure time of 3.5 to 5 ms and the rear laser, which tracks the raw pouch material, requires an exposure time of 0.5 to 1 ms. Despite the longer exposure time of one of the lasers, the longer time was still fast enough to max out the laser's data-transfer rate (100 Hz).

For the experiment, a Kokam 16 Ah cell was discharged to empty by using a constant current discharge until a lower voltage limit of 2.71 V was reached. The cell was then rested for an hour before a 2C CCCV protocol was applied. As the battery started charging, the laser assembly was set to move back and forth across the surface of the battery, specifically the 1 cm (width of the profiler) strip at the top of the area on the face of the cell where active material is present underneath. Because the laser runs back and forth in front of the IR camera, the camera is set

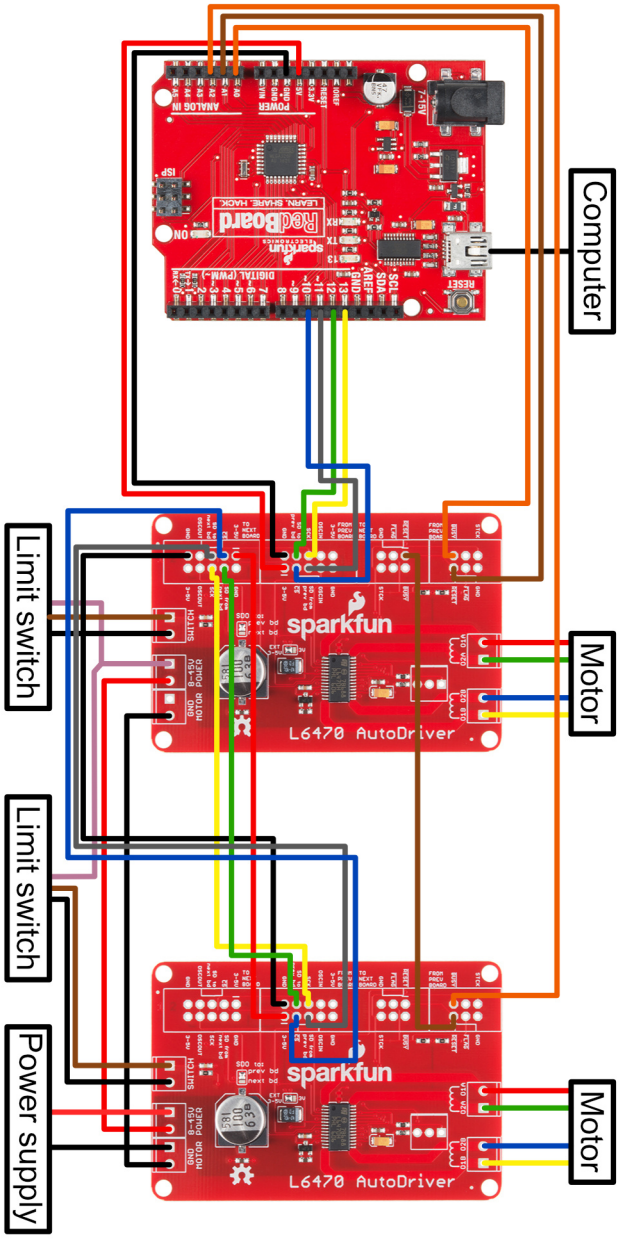


Figure 4.5: Hook up diagram between Sparkfun Redboard (microcontroller) and two Sparkfun Autodrivers (stepper motor drivers)

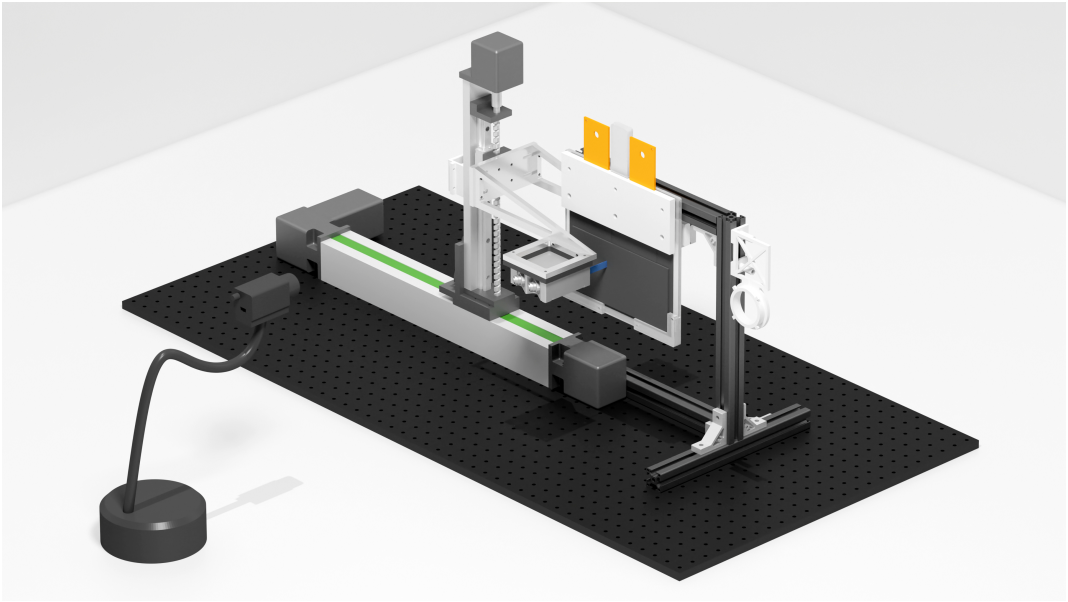


Figure 4.6: Render of assembled laser rig on motorized stages with IR camera.

to capture a single frame every time the laser assembly moves out of the way. So, laser data and camera measurements were alternately taken, but because time in between scans of each device are short, the data was linearly interpolated to match the timings between the power supply, the laser profilers, and the IR camera.

A sample scan from the laser dilatometers is shown in the top image of Figure 4.7. The scan is made up of individual 1 cm scans being collected by the sensor at a rate of 100 Hz and assembled into a single array to represent the surface of the battery. The data is quite noisy and some regular oscillations can be seen. The stage is moving quickly at a speed of approximately 200 mm per second, so a single scan across this battery takes approximately 1 second. The front and rear surfaces should not have any regularity or periodicity, so applying a fast fourier transform (FFT) to the data should reveal the frequencies associated for noise and vibrations to aid in designing the filters that will remove them

A single frame was averaged along the width of the beam to collapse the scan into a single profile and that profile was analyzed. The FFT was applied to every scan in this experiment and the frequencies that were captured were tallied. There are two frequency peaks that occurred in approximately half the scans at about 7 Hz and 23 Hz, and there is a 9 and 14 Hz signal that occurs at almost every scan.

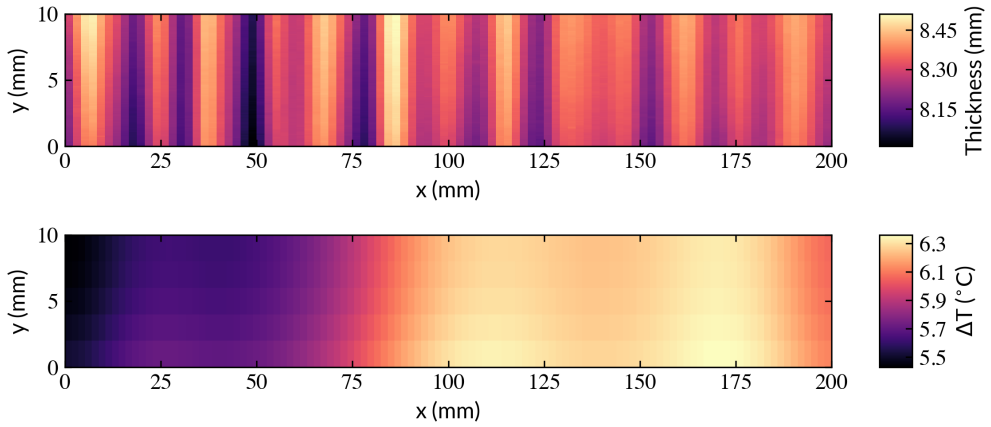


Figure 4.7: Sample dataset of the battery thickness (top) and sample dataset from the IR camera in the same area captured by the lasers (bottom).

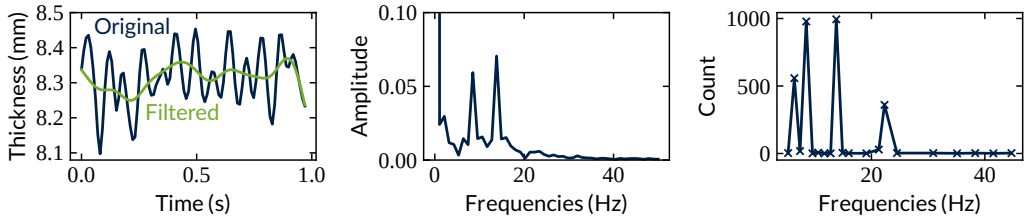


Figure 4.8: Single profile of battery thickness with filtered data (left), FFT output of the single profile (middle), and tallied occurrence of frequency signals in every scan of the 2C CCCV experiment (right).

The horizontal stage is moving at a speed of over 200 steps per second, so none of these should be related to stepper motors having distinct steps per movement. The relatively low frequency signals seem more likely to point towards the entire laser assembly shaking as it moves because it is two cantilevers. To smooth the data, each scan was put through a lowpass Butterworth filter and applied using zero phase filtering algorithm. The designed Butterworth filter was a 5th order filter and has a cutoff frequency that was set to 6.5 Hz, meaning only data with frequency signatures below 6.5 Hz are allowed through, while higher frequency data are attenuated. These results are summarized in Figure 4.8, and the effect of the filter is shown as the green line in the far-left plot. The resulting profile does look smoothed, so the same filtering processing was applied to each individual profile that makes up a single scan and to every scan that spans the length of the experiment.

A sample dilatometry scan is shown on the left side of Figure 4.9. After filtering, the data were arranged into horizontal and vertical bins to track local behaviors in the area covered by this scan. Separating the 200 mm by 10 mm strip into 3 horizontal regions (left, middle, and right) and tracking the average change in those areas yields the plot on the right of Figure 4.9. Each bin encompasses a rectangle with dimensions of 66.67 mm by 10 mm. The vertical dashed line in the right plot represents the transition of the experiment from its constant-current mode into the constant-voltage mode, where the current starts decreasing to hold the cell at its upper voltage limit. In Figure 4.10, the processing was changed by arranging the corresponding area into three horizontal strips. Each strip has a dimension of 200 mm by 3.33 mm. Tab locations where the battery makes contact with the power supply are shown for illustrative purposes and are not to scale. As a reminder, the total battery area for this cell is 200 mm by 100 mm, so the scan consists of 100% of its width, but only 10% of its height. The volume expansion maps are not to scale, the tabs are drawn in to help visualize where they are horizontally with respect to the active battery material area.

When separated into the horizontal strips, the average change in each region is nearly identical, with some separation occurring after an SOC of ∼85% had been reached. On the other hand, when separated into the left, middle, and right regions, a larger difference is observed between each region. In particular, the left side seems to have a slightly larger expansion. The data are still quite noisy, but the time-averaged expansion of the end section shows there is 8 micrometer greater expansion in the left-hand side *vs* the right, which is much greater than the sensitivity of the laser profilers (1 micrometer).

The noise issue in some of this analysis should have been expected from swinging a sensor with high sensitivity, so its use case may suit other types of experiments more. However, this experiment does show that when large SOC changes are involved, there is enough expansion ($\sim$ 140 μm) that a lower sensitivity laser with a larger beam could be utilized in combination with a smaller battery to simultaneously scan a larger portion of the battery, if not the entire battery, similar to the work of Rieger

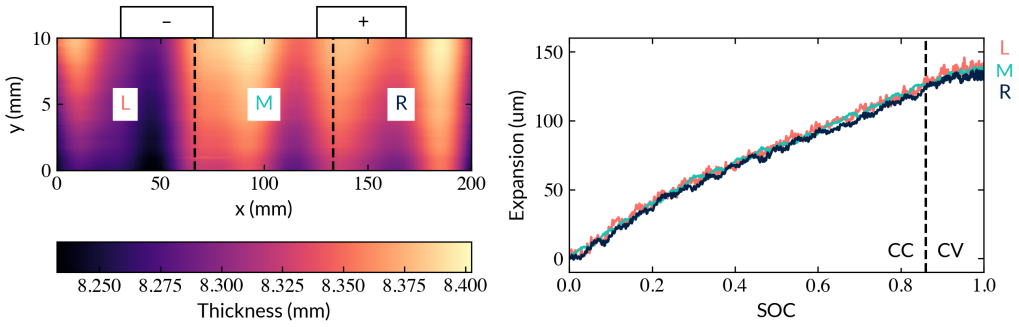


Figure 4.9: Filtered upper edge scan of a Kokam 16 Ah pouch cell showing cell thickness separated by dashed lines to represent the different horizontal areas for analysis (left). Average expansion of the areas highlights on the left plot as a function of SOC (right).

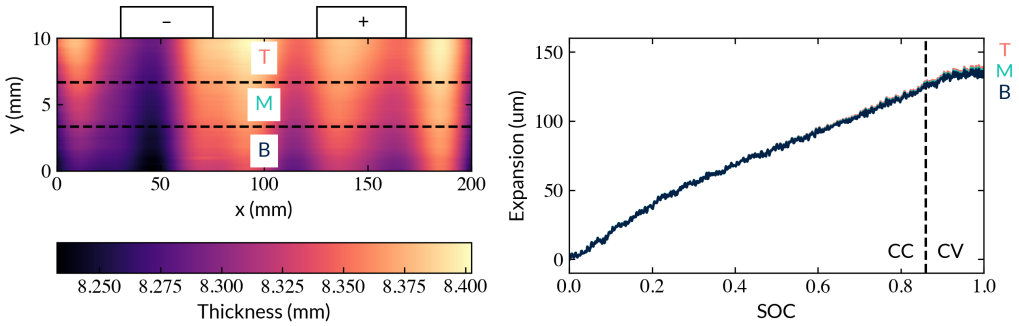


Figure 4.10: Filtered upper edge scan of a Kokam 16 Ah pouch cell showing cell thickness separated by dashed lines to represent the different vertical areas for analysis (left). Average expansion of the areas highlights on the left plot as a function of SOC (right).

et al. [59]. To make use of this set-up in its current iteration, a separate experiment was designed to characterize coupled thermo-electrochemical phenomena. One such phenomena is the convolution of SOC-related expansion and dynamical thermal expansion. It is worth noting that during the course of this experiment, there was a 6-7 degree increase in cell surface temperature during the constant-current portion of the experiment, accompanied by a steady drop once the constant voltage section began. This should have a measurable effect on the dilatometry measurements due to thermally induced volume change, but to an unknown extent.

4.5 Localized laser dilatometry with IR sensor measurements

Instead of moving the lasers at high speed around the surface of the battery, the next experiment concentrated on gathering data at a higher frequency at a fixed location with a squarewave input signal like Chapters 2 and 3. Higher frequency data acquisition was done by keeping the laser profilers focused on the same location, which unfortunately blocks the line of sight of the IR camera. An IR sensor was brought in to resolve this issue. An IR sensor operates in the same manner as an IR camera by providing contactless temperature measurements, but without minimum focus distance limitations. The main limitation of an IR sensor is the small spot size of its measured area. In this experiment a Calex PMU201 IR sensor was attached to the laser assembly with a custom designed holder that is made with laser-cut pieces of acrylic. This sensor has a sensitivity of 0.1 °C (compared to the 0.05 °C of the IR camera described earlier), but it is sufficient to detect the temperature oscillations induced by the 4C amplitude and 100 s period squarewave signal.

With the optics of this sensor, if pressed against the surface of the battery, the spot size of the sensor is a circular region with a diameter of 11.9 mm. The holder was designed such that it is at the same height as the laser profiler's beam and the lens element is at the same distance away from the battery as the laser source. With a separation distance of approximately 56 mm, the size of the IR sensor's measurement spot is a circle with 14.7 mm diameter. The acrylic pieces hold the IR sensor at a fixed 20 degree angle, so that the measurement is taken where the beam is, instead of immediately to the left of it. This slightly alters the measurement spot from a circular region to an oval shaped region. The dimensions of these acrylic pieces along with a render of the assembled holder are shown in Figure 4.11.

An experiment that was designed to probe some of the coupled electrochemical/mechanical/thermal phenomena was conducted. A squarewave with a 4C amplitude, and a 100 s period was applied to a Kokam 16 Ah pouch cell until a periodic steady state in temperature was reached; the current was then turned off, but the lasers and IR sensor kept on collecting data until the cell temperature

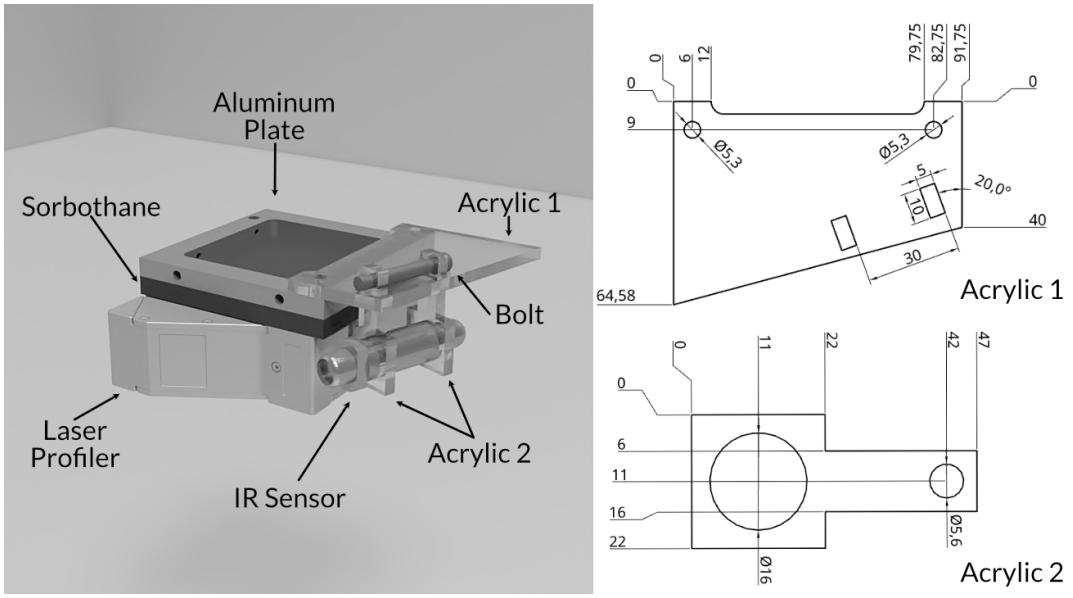


Figure 4.11: Detailed drawings of the acrylic IR sensor holder that is attached to the laser profilers.

reached ambient temperature again. The lasers and the IR sensor were aimed at the center of this large-format cell for the entirety of the experiment. The laser sensors were measured to be approximately 118 mm apart, so the thickness of the cell would be this fixed distance minus the measurement captured by the two individual lasers. The entire 10 mm laser profile was averaged to capture general behavior highlighted by the beam. This experiment's raw data is shown in Figure 4.12. Similar to the previous section there is a bit of noise in this measurement although it is a different kind of noise. This noise is inherent to the laser's readings, when previously it was mostly due to the motion of the motorized stages. Despite the noise, the periodicity of the battery thickness signal is obvious, so a similar FFT analysis was conducted. After applying the transform, there is a strong peak at the 0.01 Hz frequency corresponding to the 100 second period of the applied squarewave. The peak confirms that there is a signal in the noisy data and the noise can be filtered out. A lowpass 5^{th} order Butterworth filter with a cutoff frequency of 0.012 Hz was chosen to clean up the battery thickness signal, and it was applied both forwards and backwards on the data signal. This filtering process is zero-phase so that features occur at the same time in the filtered and unfiltered

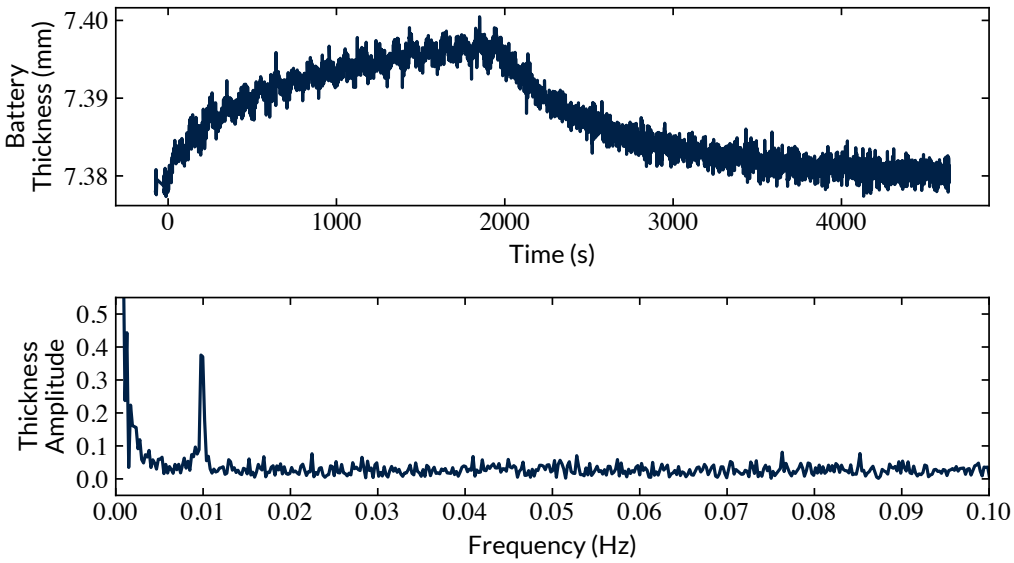


Figure 4.12: Calculated cell thickness (top) with FFT analysis of the data signal (bottom)

signals, which could be useful for distinguishing the various lag times between the current, voltage, expansion, and temperature signals.

The dilation data was converted into a volume change by multiplying the data with the area covered by the laser beam. The beam covers a length of 10 mm and has a thickness of 1 mm. On the left plot of Figure 4.13, the volume and temperature change data is plotted against time in the squarewave experiment. The SOC change induced by the 4c100s squarewave is 5.56% (from 47.22% to 52.78%) and the mean SOC for the duration of the experiment is at 50%. In the second half of the experiment, where volume expansion was measured as the battery cooled down, the resulting volume change arises almost entirely from thermal effects because the current has been turned off. On the right plot of Figure 4.13, where the volume expansion is plotted against the cell's surface temperature, the blue line represents the portion of the experiment where the current is off. The line follows a linear trend with a slope of 0.0125 mm^3 $°C^{-1}$, arriving at a value of 1.694 $\times 10^{-4}$ $°C^{-1}$ for the volumetric coefficient of thermal expansison.

The right plot of Figure 4.13 also shows that the main contributor to this volume change in this experiment is thermal. The deviation of the red curve

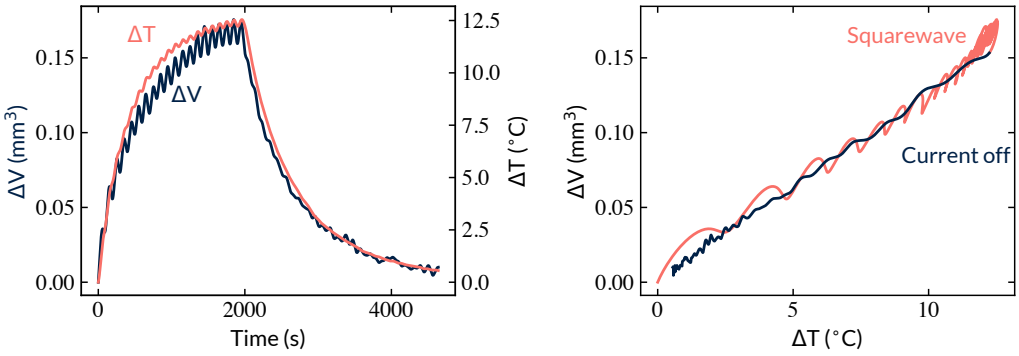


Figure 4.13: Volume change and temperature change *vs* time in the squarewave analysis experiment (left), and volume change *vs* temperature change (right).

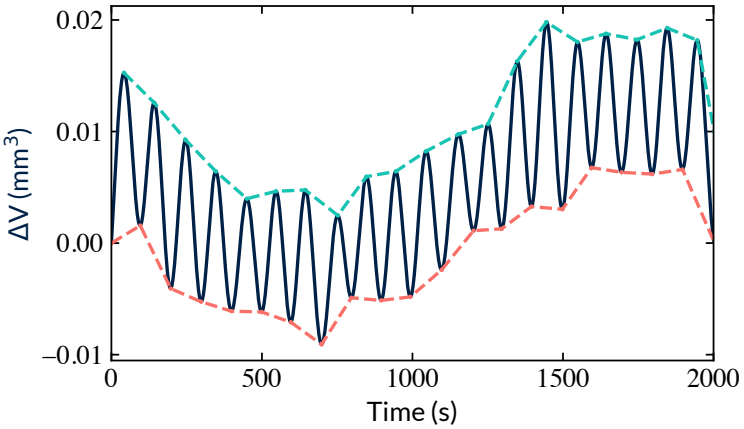


Figure 4.14: Center volume change of Kokam 16 Ah pouch cell with temperature effects removed

from the linearly trending blue curve is the measured volume change due to intercalation/deintercalation effects. By subtracting out the thermal effects from the filtered volume change data, the oscillations have amplitudes ranging from 0.0055 mm^3 to 0.0086 mm^3 as shown in Figure 4.14. So over a swing of 5.55% SOC, there is a volume change of 0.011 to 0.017 mm^3, with an average value of 0.013 mm^3. A 5.55% swing over the same SOC range from the previous CCCV experiment yielded a volume change of 0.06 mm^3. This is a much larger value compared to the one calculated from the squarewave experiment. The difference most likely arises from the fact that the CCCV experiment was scanning the top strip of the battery near the tabs, whereas the squarewave experiment was measuring the center of the

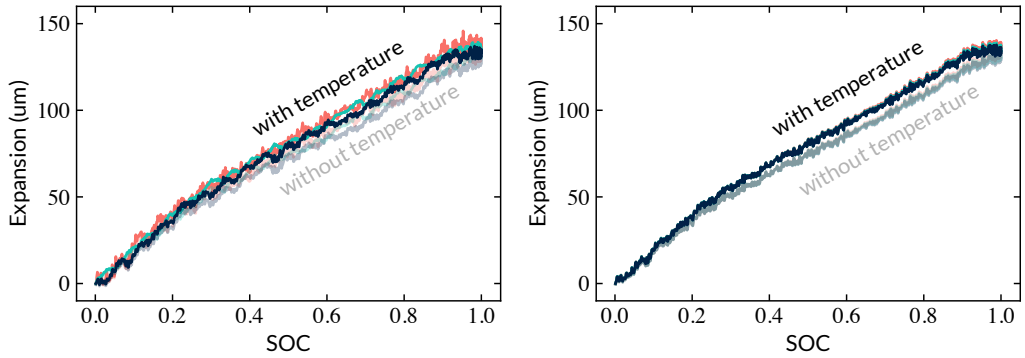


Figure 4.15: Data from Figure 4.9 and Figure 4.10 replotted with thermally induced volume change effects taken out.

large front face. From the previous experiment, it is most likely the case that the change occurs closer to the tabs first before reaching the lower parts, following the trend of how the current distribution looks in pouch cells with vertically oriented tabs. Since the squarewave experiment only oscillates in a small window of SOC values, most of the mechanical changes would be occuring further above where the measurements are currently taking place.

The thermally induced volume change contribution was then subtracted from the CCCV experiment from the previous section, resulting in the data shown in Figure 4.15. Without the temperature contribution due to the high-rate charge current, there is a slope change in the expansion *vs.* SOC plot: specifically, the slope decreases and the two sets of data start diverging from each other at about 25% SOC, and the slope increases at around 90% SOC. This further confirms that in the mid-range of a cell's available charge states, the SOC induced mechanical changes are less pronounced.

If we pass the two signals through a bandpass filter to remove the noise and the overarching time relaxation of the signal, only the periodic behavior of the data is shown. Looking at the data in this manner illustrates the time delay between the different datasets. Robinson *et al.*, showed that there is a large time delay for surface temperature readings when looked at in conjunction with the current source from thermal impedances [13]. It can be seen from these initial periods that the mechanical behavior tracks much better with the current input signal, while the

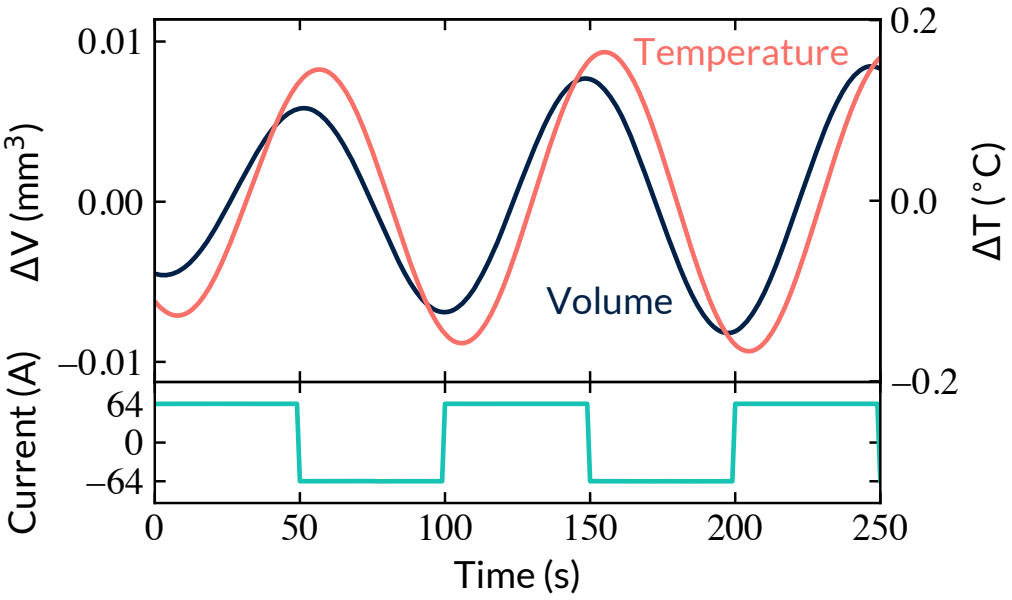


Figure 4.16: Bandpass output of the volume expansion and temperature data with the current input as a reference

temperature delay was as expected. On average, tracking the peaks for the duration of the experiment, the temperature signal lags behind the volume expansion signal by ∼6 seconds, but ranges between 3 and 10 seconds. This changing phase shift could be due to competing thermal and SOC effects. The lag in the thermal data in reference to the squarewave input signal is caused by the thermal impedances in the cell, and should remain fairly constant in this experiment. However the expansion data will be affected by both the local SOC and the cell temperature, causing them to interfere with each other. For example, in the early stages of the experiment, in the discharge portions of the squarewave, the volume should be contracting the moment lithium is being extracted, but the joule heating caused by the applied current will mask it with thermal expansion of the battery components. The volume expansion data looking like a sinusoid is also an artifact of the filtering, because the slowing down of the cell expansion is, in a way, anticipating a change in current, which it should not have the ability to do.

4.6 Conclusions

The mechanical changes in a battery are due in part to the intercalation and deintercalation mechanisms when in operation, but can also manifest without a current input when the cell changes temperature as a thermally induced volume change. So when operating protocols such as fast charge or discharges are used, overall effects seem to be dominated by intercalation effects. But with experimental protocols such as aggresive drive cycles or squarewave inputs, where SOC changes by small amounts, but temperature changes are greater, thermal effects will dominate.

Initially, equilibrium stress measurement experiments were conducted showing that in the middle of a cell's available charge states, thermally induced stress evolution can rival if not overtake the contributions from just changing SOC. This balance between the two effects changes when operating at the extreme low and high end of a cell's charge states. An experimental apparatus was later designed to simultaneously capture cell dilation and cell surface temperature. When fully charging a battery with a 2C CCCV charge profile there was an average of value 0.140 mm expansion across the 200 $\times$ 10 mm area right below the location of the connection tabs and an average cell temperature increase of 6.5 °C. A follow-up experiment was conducted where localized expansion and temperature measurements were taken while a 4C (64 A) squarewave input signal was applied to the battery. This resulted in a method in probing the SOC and temperature contributions to volume change in a single experiment. By analyzing the cooldown of the battery after the squarewave excitation a volumetric coefficient of thermal expansion was obtained and had a value of 1.694 $\times 10^{-4}$ $^{\circ}C^{-1}$ at the center of the battery.

5 Conclusions and future work

5.1 Summary

In chapter 2, a streamlined thermo-electrochemical model was developed in COMSOL and used to simulate the maximum, average, minimum temperature transients and the voltage behavior of a 20 Ah LFP pouch cell from A123. Dimensional analysis showed that seven dimensionless variables control the output of the 3-D simulation of a squarewave current-excitation test. Similar analysis shows that the complex layered structure of the full cell can be simulated as a single-layer sandwich by rescaling certain model parameters, as long as the Biot number is low. The non-uniform temperature distribution on the cell surface due to the tab design is useful because it can be gauged to obtain estimates for the internal material properties. Material property values were obtained by matching the simulation output to the experimental temperature distribution and voltage through an iterative goal-seeking algorithm. Once a parameter set was obtained, it was shown that the model can also predict outputs at a different C-rate or a different frequency, as long as the best-fit parameters were obtained from a high C-rate experiment.

In chapter 3, the streamlined model was adapted to simulate a 16 Ah NMC pouch cell from Kokam. The new battery has a different cell design and also a different chemistry. The model was shown to be chemistry agnostic and portrayed

the behavior of the new cell with appropriate parameters. SOH tracking capabilities were demonstrated by tracking the changes in the parameter sets when different temperature and voltage data was fed to the model. Despite not having any degradation mechanisms in the model, it is sensitive enough to respond to the different datasets and shows that certain parameters correlate with changes in SOH.

In this study, two cells were cycled in different ambient conditions until their SOH fell by a minimum of 5%. One cell was cycled in a 25 °C environmental chamber, while the other was cycled in a 10 °C chamber. Both cells were then compared to a pristine cell with a similar serial number. The 10 and 25 °C degraded cells lost 8.3% and 6.6% capacity, respectively, after triggering the end condition of the cycling procedure. The extracted parameter sets of these two cells had noticeable changes in the ionic and thermal conductivity values. There are varying degrees of changes, from 7.5% to a 15% increase in thermal conductivity across the two degraded cells and the SOCs at which the analysis was performed. These changes were accompanied by a 15 to 25% drop in the ionic conductivity parameter.

With the NMC system, the optimized parameters were unable to generate good fittings for the low C-rate validation tests. The model tended to underpredict the size of the enclosing voltage envelope during the squarewave experiment. Although this problem was also observed in the A123 system, the magnitude of the difference was much smaller, so it did not appear to be an issue. Given the behavior across the different experimental conditions, there is a promising possible solution that will be discussed in the next section.

In chapter 4, initial equilibrium stress experiments were conducted showing that in the middle of Ford's 5 Ah NMC cell's available charge states, thermally induced stress evolution can rival if not overtake the contributions from intercalation dependent stress. The balance between the two competing effects changes depending on the reference SOC and ambient temperature. At less than 50% SOC and at standard ambient conditions ($\sim$ 25 °C), it takes a 5 degree temperature swing to create the same stress effects as changing the battery SOC by 10%. At above

50% SOC, it takes a 20% swing in battery SOC to create the same stress response as a 5 degree change in ambient temperature.

Afterwards, an experimental apparatus was designed to simultaneously capture cell dilation and cell surface temperature. During a charging experiment where a battery was charged with a 2C CCCV charge profile, there was a mean dilation of 0.140 mm in the 200 × 10 mm area right below the location of the connection tabs. During the same experiment, the average surface cell temperature increased 6.5 °C during the CC portion of the experiment and started cooling down during the CV portion.

A follow-up experiment was conducted where localized expansion and temperature measurements were taken during a 4C squarewave current excitation. This resulted in a method in probing the SOC and temperature contributions to volume change in a single experiment. By analyzing the cooldown of the battery after the squarewave excitation a volumetric coefficient of thermal expansion was obtained and had a value of 1.694 $\times 10^{-4}$ $^{\circ}C^{-1}$ at the center of the battery. By looking at the squarewave portion with the previous result, the purely SOC induced volume change was obtained.

5.2 Future work

5.2.1 Streamlined electrochemical/thermal model

A consistent problem with the streamlined electrochemical/thermal model is that the extracted ionic conductivity is lower than even the low end of values reported in lithium-ion battery electrolyte literature. A second problem is the underprediction of voltage when simulating squarewaves with relatively low C-rates. Finally, the spatial temperature distribution cannot accurately simulate the horizontal asymmetry observed in experiments. The underprediction issue was less of a problem in the A123 LFP system, and the horizontal asymmetry was less of an issue in the Kokam NMC system. The difference in behavior could be explained by the general differences in cell design and battery components, but the overarching problems still exist.

The low ionic conductivity value is due to the parameter encompassing missing resistances in the model that are necessary to generate the ohmic and reaction heat. The second problem, the underprediction in the voltage envelope for the low C-rate validations, does not appear to be a problem in the higher C-rate validation where the squarewave period was adjusted. Forcing the fitted conductivity to an even lower value will not solve the problem as the value is already lower than expected, but this feature not occuring in the high frequency validation case could imply that there is a strong temperature dependence to this resistance. The high frequency squarewave does generate consistent amounts of heat as the low frequency squarewave, which makes sense as the two cases have similar current throughput on the cell, just applied in a different way. Finally, the last part is the horizontal asymmetry. The non-uniform nature of the battery's temperature distribution is due largely to the non-uniform current density. Even though this is captured in the model, there is no resistance against the lithium that prevents it from moving as quickly as it can, thus local SOC does not change by any significant amount. Discrepancies between the shape of the current distribution and temperature distribution would therefore have to be accounted for in the thermal parameters used in the model. But there are no physically reasonable changes that can be implemented to fix those discrepancies.

The missing phenomenon would therefore be a sort of resistance, one that affects local SOC, but also has a strong temperature dependence. One such feature is solid diffusion in the electrodes. This feature would introduce a large source of resistance that would balance out the low predicted value of $\kappa_{\text{liq}}^{\infty}$. It also has a strong temperature dependence as reported in the works by Ecker, Schmalstieg, and Chen [47, 117, 125]. Coincidentally the activation energy associated with solid diffusion of lithium was very similar to the extracted activation energy associated with the ionic conductivity in this particular model. Solid diffusion will affect the rate at which lithium is intercalated/deintercalated to and from the two electrodes creating the stronger local SOC effect that should be able to create the horizontal asymmetry that is currently missing.

5.2.2 Electrochemical/thermal/mechanical apparatus: experiments and upgrades

The two experiments that were executed in chapter 4 showed that there is a large difference in mechanical behavior when fully charging/discharging a battery, and when compared to an operational mode where small SOC swings were introduced and repetitively applied. In the small repeated perturbations, a 5.5% SOC swing centered around 50% SOC induced a 2 micrometer expansion and contraction, while in the full charge experiment, a 5.5% increase in SOC (also in the middle of its charge states) induced a 6 micrometer expansion. This could be due to various edge effects of the pouch as the full charge experiment was collecting data near the tabs, and the periodic squarewave was collecting data in the center of the active material area. The edges are where the excess pouch materials are rolled up and it would be easiest to unravel if forced to by the active materials expanding near it, while the center is well constrained.

If the above is true, then there are a few experiments that could be done to probe the system's behavior. The same periodic squarewave experiment should be tested on various locations away from the geometric center, but not too close to the edges. The squarewave portion can be used to check if different areas exhibit different amounts of SOC-induced volume expansion, and the cooldown portion is needed to confirm the coefficient of thermal expansion and see if it is consistent as long as edge effects are not in play.

A constant current discharge from 100% SOC to 0% SOC is not something a EV battery has to regularly endure. In various drive cycle tests, there are potentially many sections of aggressive acceleration/deceleration, regenerative braking, and coasting. The SOC changes are more erratic and might not even go through a large range of the available states [33, 131]. But the joule heating associated with all of those actions will still occur. It might be interesting to see the mechanical effects differ in these situations, where the thermally induced volume change will play a much larger part.

The experimental apparatus itself could also benefit from a redesign to further reduce vibrations. Upgrading the generic vibration dampening foam from RS components to the optical table grade sorbothane has helped, but the included 2-axis connector used to hold the vertical ball screw driven stage to the horizontal belt driven stage was not the best choice. Figure 4.4a, shows how it is currently held together, but the vertical stage should actually be inverted to keep the heavier motor held to the bottom instead of swinging in the air. This would require a redesign of the joint connecting the two stages. Also since the speed and travel requirements are more well understood and a proof-of-concept experiment was done, an upgrade to servo motors could be beneficial for reduced vibrations at higher speeds and more consistent torque application, despite the incresed cost and complexity to implement.

The inclusion of the IR sensor also reduced the requirements for speed on the stages. Previously the rig was designed for speed so that the lasers can be quickly moved out of the way for the IR camera to record the surface distribution. If it is not necessary to capture the entire temperature map simultaneously, and only where the lasers are currently measuring, then the speed can be tuned down to also decrease vibrations.

5.3 Conclusions

This dissertation aimed to explore non-invasive characterization techniques for large-format lithium-ion batteries. These techniques could be used to better understand the state of these batteries and their unique current distributions induced by their cell design. A comprehensive study of the health of used batteries can ease environmental concerns regarding battery packs and the cells that comprise them by recognizing potential second-life applications. The parameterization process during health screening could also provide direction for improved cell design, if for example, one wants to influence particular material property values, or change how heat is generated in the battery for better cooling.

In Chapter 2 and Chapter 3, despite the extreme simplifications to the classic Dualfoil model, the streamlined model was still able to accurately predict the

temperature and voltage behavior in response to a zero-mean squarewave for multiple chemistries. Of particular interest is the voltage relaxation within the individual squarewaves and in the shrinkage of the voltage envelope, a phenomenom usually associated with slow diffusion, was simulated by introducing a k_U parameter which was defined as the slope of the linearized OCV curve, and including temperature dependences for key parameters (κ_e and i_0). In Chapter 2, the goal was to develop a simplified model to predict electrochemical and thermal behaviors, the in-depth coupling between cell temperature and the SOC was key in predicting the overall voltage behavior without the need for diffusion in the system. This inverse modelling analysis provides a new method of determining multiple parameter estimations, when ordinarily, the seven obtained parameters would require seven different experiments. In Chapter 3, the thermography data showed preliminary signatures of anode side reactions as the mechanism that is responsible for the capacity loss. This was shown in the change in global thermal behavior in the cell prioritizing heating of the left (anode tabbed) side. And the

The model did what it was set out to do, predicting surface average, the hot spot, and the cold spot temperatures. But if matching the entire 2D temperature distribution is necessary, then the model does leave some things to be desired. The hot and cold spots lining up in the center of the cell in the vertical direction in the A123 system allowed this to be ignored without affecting the simulation results with respect to predicting $T_{max}, T_{avg}, T_{min}$. Quirks in the optimization and the ultimate parameter value extractions provide insight into what the missing phenomena is. Despite the voltage relaxation not needing the physics of diffusion, the lack of matching capability in the horizontal direction of the cell (perpendicular to the tabs) is speculated to be because of diffusion.

In Chapter 4, equilibrium measurements reveal a potential degradation pathway from thermal cycling where common temperature fluctuations in a day can induce a stress effect similar to shallow charge/discharge cycles if the battery is stored at its higher charge states. The contour plots reveal at lower SOCs, even large temperature swings can't induce much of a response from the force sensors, while

at the mid and high SOC states, temperature effects will dominate the stress response. This could imply that graphite's volume expansion is much more sensitive to temperature than the NMC. The CCCV experiment showed how the decrease in temperature from the CV portion of the experiment was masking what should've been a monotonic increase in volume from the battery being charged, confirming why research in this field is traditionally limited to low C-rates. But, similar to the lock-in thermography experiments, the experiments with periodic input signals (with relatively high C-rates), was able to deconvolute temperature and SOC effects in the volume expansion data after data processing with some filters. The phase lags between the expansion signal, the temperature signal, and the voltage allows for some speculation behind what mechanisms are occuring.

Appendices

A

Supplementary fitting results

A.1 Various temperature and voltage fittings for Kokam NMC cells

Extra fitting results from chapter 3, specficially the cold degraded and the ambient degraded cells at 30% and 60% SOC.

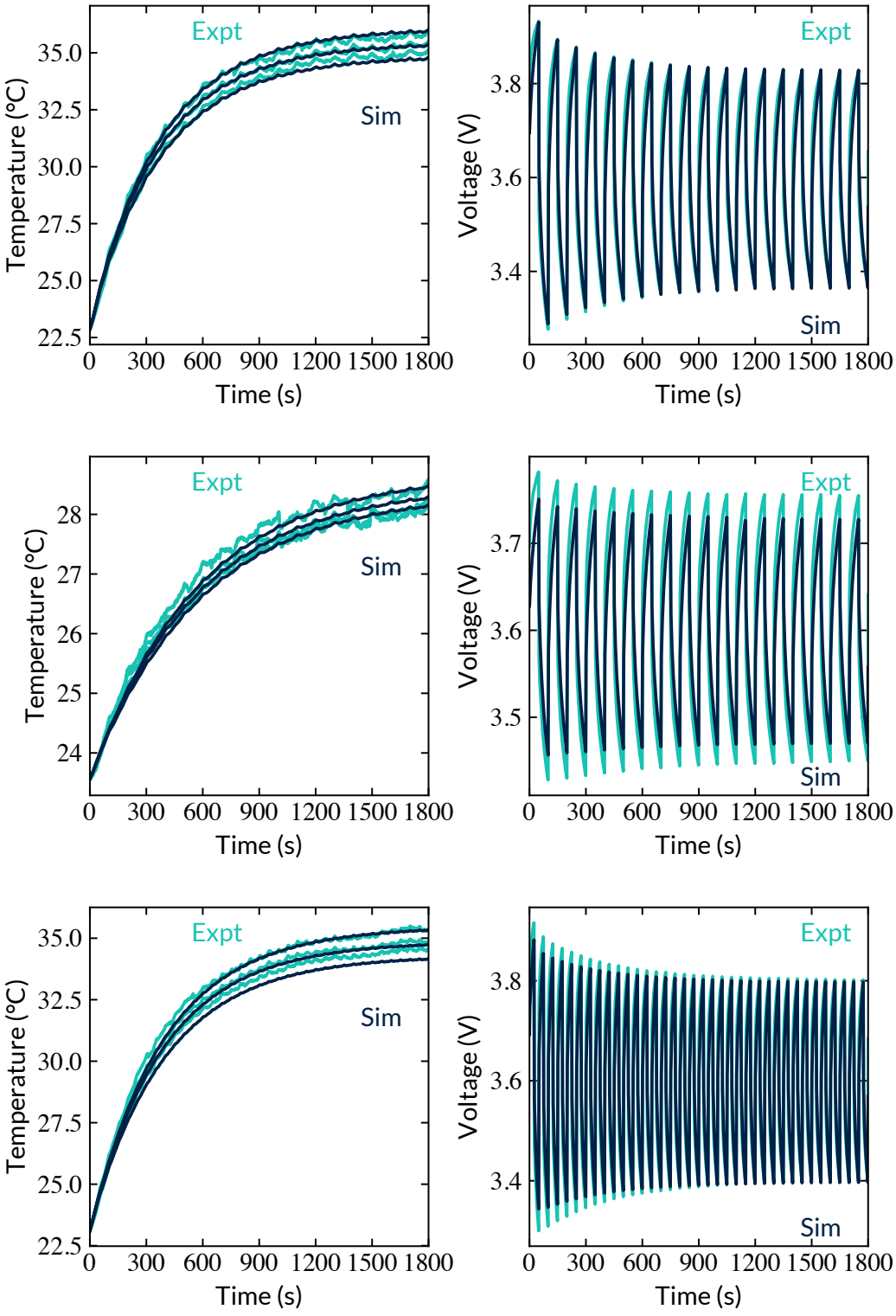


Figure A.1: Cold degraded cell fitting results for a 4c100s squarewave in the top row, followed by 2c100s and 4c50s validations at a mean SOC of 30%.

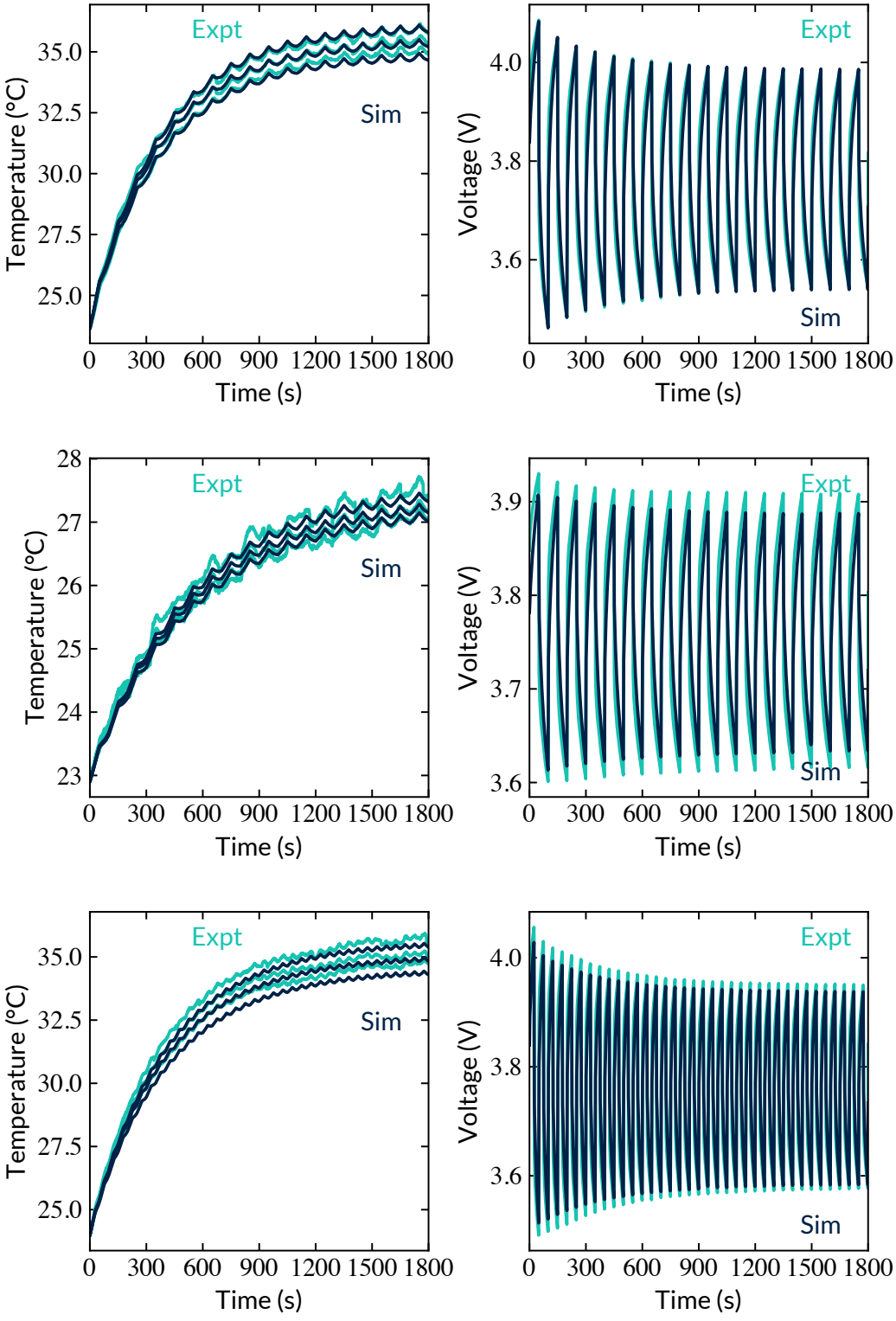


Figure A.2: Cold degraded cell fitting results for a 4c100s squarewave in the top row, followed by 2c100s and 4c50s validations at a mean SOC of 60%.

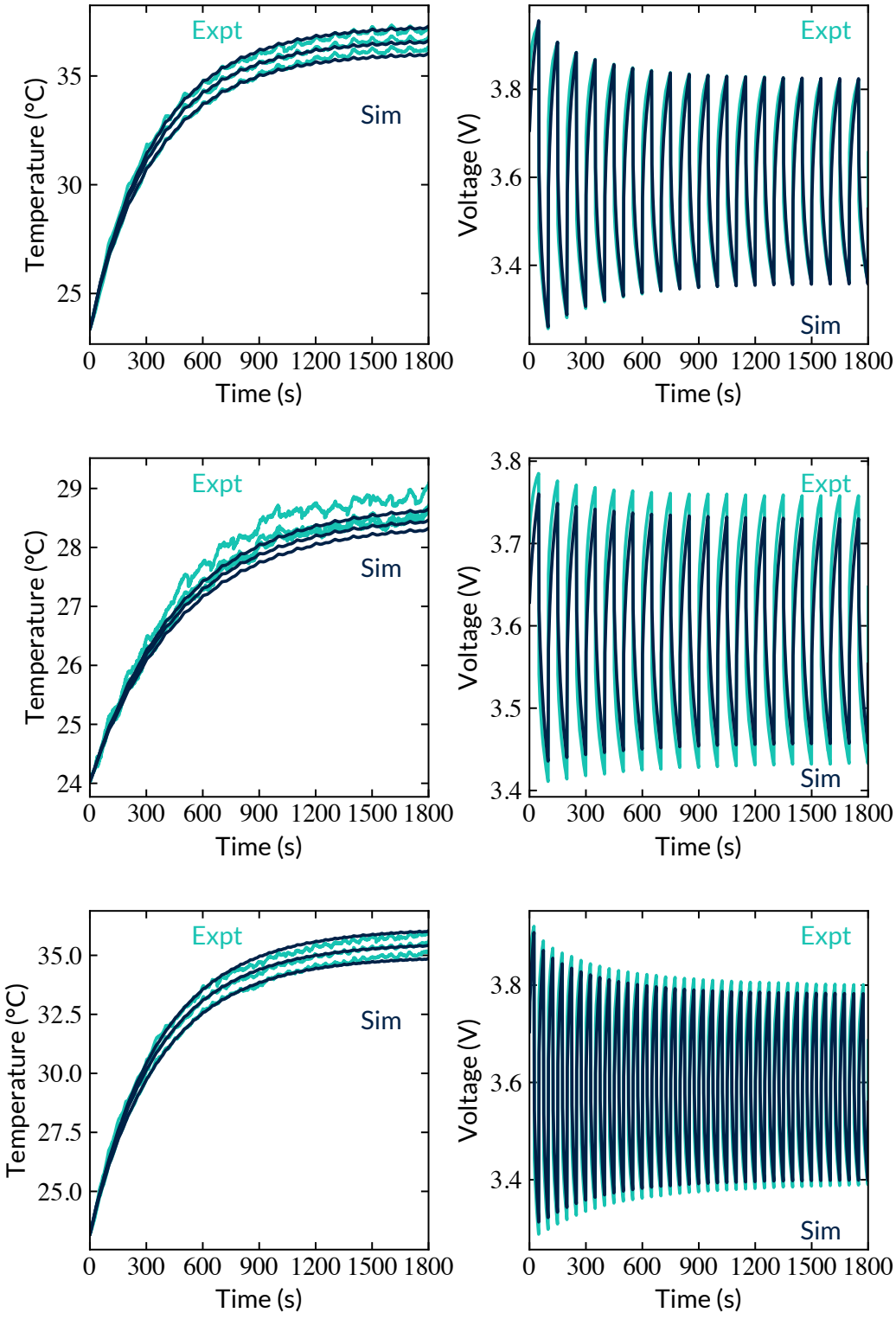


Figure A.3: Ambient degraded cell fitting results for a 4c100s squarewave in the top row, followed by 2c100s and 4c50s validations at a mean SOC of 30%.

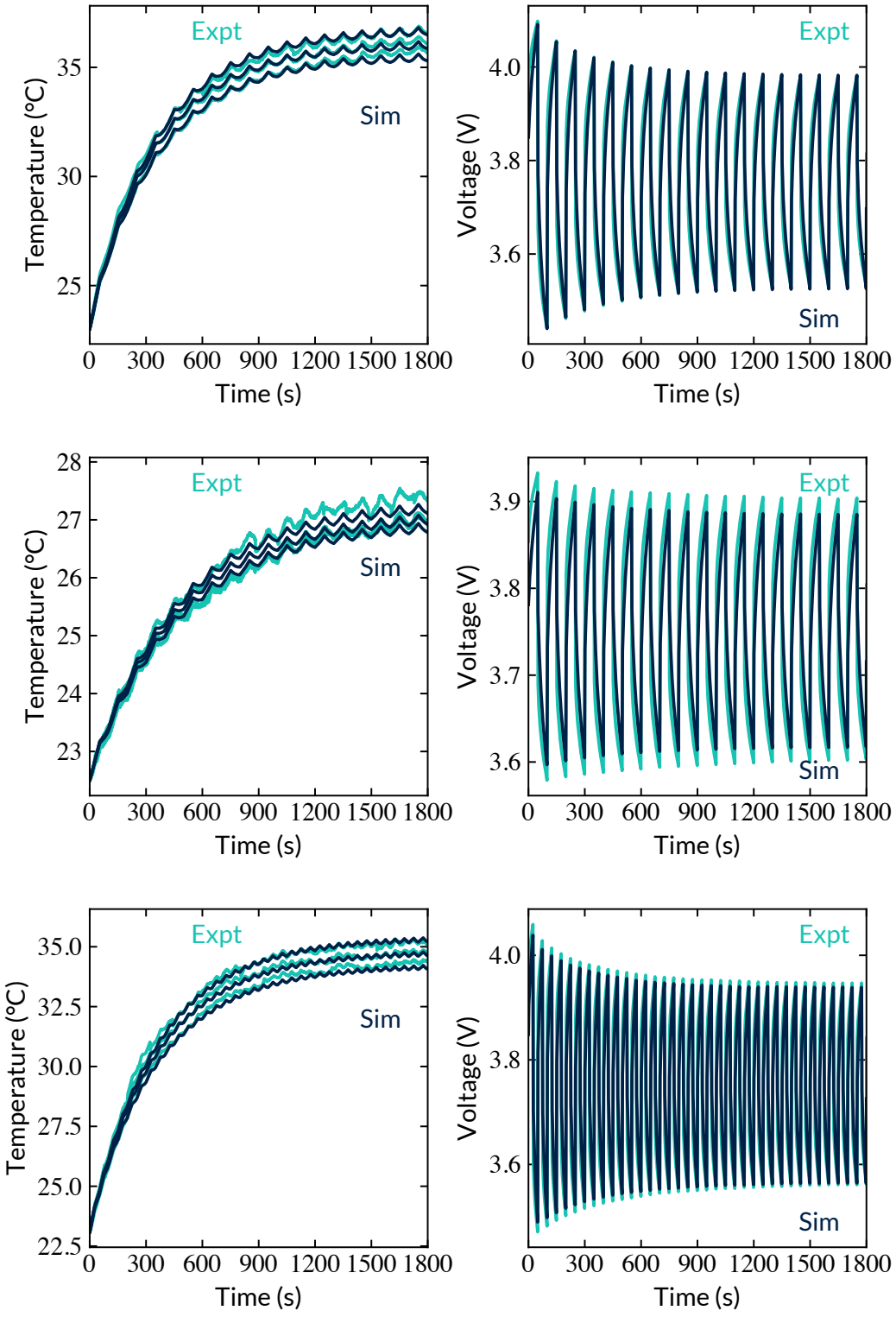


Figure A.4: Ambient degraded cell fitting results for a 4c100s squarewave in the top row, followed by 2c100s and 4c50s validations at a mean SOC of 60%.

References

[1] Kenza Maher and Rachid Yazami. "A Study of Lithium Ion Batteries Cycle Aging by Thermodynamics Techniques". In: *Journal of Power Sources* 247 (Feb. 1, 2014), pp. 527–533. DOI: 10.1016/j.jpowsour.2013.08.053.

[2] Jia Li et al. "Study of the Storage Performance of a Li-Ion Cell at Elevated Temperature". In: *Electrochimica Acta* 55.3 (Jan. 1, 2010), pp. 927–934. DOI: 10.1016/j.electacta.2009.09.077.

[3] Minggao Ouyang et al. "Low Temperature Aging Mechanism Identification and Lithium Deposition in a Large Format Lithium Iron Phosphate Battery for Different Charge Profiles". In: *Journal of Power Sources* 286 (July 15, 2015), pp. 309–320. DOI: 10.1016/j.jpowsour.2015.03.178.

[4] M K Domroese et al. "Thermal Conductor for High-Energy Electrochemical Cells". Pat. 2004.

[5] C Allison. "Heterogeneous Ohmic Contact for a Voltaic Cell". Pat. 2013.

[6] J. Full et al. "Comparing Technical Criteria of Various Lithium-Ion Battery Cell Formats for Deriving Respective Market Potentials". In: *2020 IEEE Electric Power and Energy Conference (EPEC)*. 2020 IEEE Electric Power and Energy Conference (EPEC). 9–Nov. 10, 2020, pp. 1–6. DOI: 10.1109/EPEC48502.2020.9320122.

[7] Ahmad A. Pesaran, Gi-Heon Kim, and Matt Keyser. *Integration Issues of Cells into Battery Packs for Plug-in and Hybrid Electric Vehicles*. National Renewable Energy Lab.(NREL), Golden, CO (United States), 2009.

[8] Rebecca E. Ciez and J. F. Whitacre. "Comparison between Cylindrical and Prismatic Lithium-Ion Cell Costs Using a Process Based Cost Model". In: *Journal of Power Sources* 340 (Feb. 1, 2017), pp. 273–281. DOI: 10.1016/j.jpowsour.2016.11.054.

[9] Apurba Sakti et al. "A Techno-Economic Analysis and Optimization of Li-Ion Batteries for Light-Duty Passenger Vehicle Electrification". In: *Journal of Power Sources* 273 (Jan. 1, 2015), pp. 966–980. DOI: 10.1016/j.jpowsour.2014.09.078.

[10] David L. Wood, Jianlin Li, and Claus Daniel. "Prospects for Reducing the Processing Cost of Lithium Ion Batteries". In: *Journal of Power Sources* 275 (Feb. 1, 2015), pp. 234–242. DOI: 10.1016/j.jpowsour.2014.11.019.

[11] Karen E Thomas and John Newman. "Thermal Modeling of Porous Insertion Electrodes". In: *Journal of The Electrochemical Society* 150.2 (2003), A176–A192. DOI: 10.1149/1.1531194.

[12] Karen E Thomas and John Newman. “Heats of Mixing and of Entropy in Porous Insertion Electrodes”. In: *Journal of Power Sources* 119–121.0 (2003), pp. 844–849. DOI: 10.1016/S0378-7753(03)00283-0.

[13] James B Robinson et al. “Detection of Internal Defects in Lithium-Ion Batteries Using Lock-in Thermography”. In: *ECS Electrochemistry Letters* 4.9 (2015), A106–A109. DOI: 10.1149/2.0071509eel.

[14] Howie N. Chu et al. “Parameterization of Prismatic Lithium–Iron–Phosphate Cells through a Streamlined Thermal/Electrochemical Model”. In: *Journal of Power Sources* 453 (Mar. 31, 2020), p. 227787. DOI: 10.1016/j.jpowsour.2020.227787.

[15] Todd M. Bandhauer, Srinivas Garimella, and Thomas F. Fuller. “A Critical Review of Thermal Issues in Lithium-Ion Batteries”. In: *Journal of The Electrochemical Society* 158.3 (Mar. 1, 2011), R1–R25. DOI: 10.1149/1.3515880.

[16] Ting Cai, Anna G. Stefanopoulou, and Jason B. Siegel. “Modeling Li-Ion Battery Temperature and Expansion Force during the Early Stages of Thermal Runaway Triggered by Internal Shorts”. In: *Journal of The Electrochemical Society* 166.12 (Jan. 1, 2019), A2431–A2443. DOI: 10.1149/2.1561910jes.

[17] Xuning Feng et al. “Thermal Runaway Mechanism of Lithium Ion Battery for Electric Vehicles: A Review”. In: *Energy Storage Materials* 10 (Jan. 1, 2018), pp. 246–267. DOI: 10.1016/j.ensm.2017.05.013.

[18] Xianming Wang et al. “Understanding Volume Change in Lithium-Ion Cells during Charging and Discharging Using In Situ Measurements”. In: *Journal of The Electrochemical Society* 154.1 (2007), A14–A21.

[19] Yukinori Koyama et al. “Harnessing the Actuation Potential of Solid-state Intercalation Compounds”. In: *Advanced Functional Materials* 16.4 (2006), pp. 492–498.

[20] Rutooj Deshpande et al. “Battery Cycle Life Prediction with Coupled Chemical Degradation and Fatigue Mechanics”. In: *Journal of The Electrochemical Society* 159.10 (2012), A1730–A1738.

[21] John Cannarella and Craig B Arnold. “Stress Evolution and Capacity Fade in Constrained Lithium-Ion Pouch Cells”. In: *Journal of Power Sources* 245 (2014), pp. 745–751.

[22] Nassim A. Samad et al. “Battery Capacity Fading Estimation Using a Force-Based Incremental Capacity Analysis”. In: *Journal of The Electrochemical Society* 163.8 (2016), A1584–A1594. DOI: 10.1149/2.0511608jes.

[23] Wei-Jen Lai, Mohammed Yusuf Ali, and Jwo Pan. “Mechanical Behavior of Representative Volume Elements of Lithium-Ion Battery Modules under Various Loading Conditions”. In: *Journal of Power Sources* 248 (Feb. 15, 2014), pp. 789–808. DOI: 10.1016/j.jpowsour.2013.09.128.

[24] Juner Zhu, Tomasz Wierzbicki, and Wei Li. “A Review of Safety-Focused Mechanical Modeling of Commercial Lithium-Ion Batteries”. In: *Journal of Power Sources* 378 (Feb. 28, 2018), pp. 153–168. DOI: 10.1016/j.jpowsour.2017.12.034.

[25] Liyuan Feng et al. "Experimental Investigation of Thermal and Strain Management for Lithium-Ion Battery Pack in Heat Pipe Cooling". In: *Journal of Energy Storage* 16 (Apr. 1, 2018), pp. 84–92. DOI: 10.1016/j.est.2018.01.001.

[26] Bernhard Rieger et al. "Strain Propagation in Lithium-Ion Batteries from the Crystal Structure to the Electrode Level". In: *Journal of The Electrochemical Society* 163.8 (May 27, 2016), A1595. DOI: 10.1149/2.0431608jes.

[27] Martin Winter et al. "Dilatometric Investigations of Graphite Electrodes in Nonaqueous Lithium Battery Electrolytes". In: *Journal of The Electrochemical Society* 147.7 (2000), pp. 2427–2431. DOI: 10.1149/1.1393548.

[28] Peyman Mohtat et al. "Towards Better Estimability of Electrode-Specific State of Health: Decoding the Cell Expansion". In: *Journal of Power Sources* 427 (2019), pp. 101–111.

[29] B. Rieger et al. "Multi-Scale Investigation of Thickness Changes in a Commercial Pouch Type Lithium-Ion Battery". In: *Journal of Energy Storage* 6 (May 1, 2016), pp. 213–221. DOI: 10.1016/j.est.2016.01.006.

[30] Ki-Yong Oh et al. "Rate Dependence of Swelling in Lithium-Ion Cells". In: *Journal of Power Sources* 267.0 (2014), pp. 197–202. DOI: 10.1016/j.jpowsour.2014.05.039.

[31] Johannes Schmalstieg and Dirk Uwe Sauer. "Full Cell Parameterization of a High-Power Lithium-Ion Battery for a Physico-Chemical Model: Part II. Thermal Parameters and Validation". In: *Journal of The Electrochemical Society* 165.16 (2018), A3811–A3819. DOI: 10.1149/2.0331816jes.

[32] Marius Bauer et al. "Understanding the Dilation and Dilation Relaxation Behavior of Graphite-Based Lithium-Ion Cells". In: *Journal of Power Sources* 317 (June 15, 2016), pp. 93–102. DOI: 10.1016/j.jpowsour.2016.03.078.

[33] S. Panchal et al. "Thermal and Electrical Performance Assessments of Lithium-Ion Battery Modules for an Electric Vehicle under Actual Drive Cycles". In: *Electric Power Systems Research* 163 (Oct. 1, 2018), pp. 18–27. DOI: 10.1016/j.epsr.2018.05.020.

[34] Matthias Fleckenstein et al. "Thermal Impedance Spectroscopy - A Method for the Thermal Characterization of High Power Battery Cells". In: *Journal of Power Sources* 223 (Feb. 1, 2013), pp. 259–267. DOI: 10.1016/j.jpowsour.2012.07.144.

[35] Jianbo Zhang et al. "Simultaneous Estimation of Thermal Parameters for Large-Format Laminated Lithium-Ion Batteries". In: *Journal of Power Sources* 259 (Aug. 1, 2014), pp. 106–116. DOI: 10.1016/j.jpowsour.2014.02.079.

[36] Patrick J. Osswald et al. "Fast and Accurate Measurement of Entropy Profiles of Commercial Lithium-Ion Cells". In: *International Conference on Electrochemical Energy Science and Technology (EEST2014)* 177 (Sept. 20, 2015), pp. 270–276. DOI: 10.1016/j.electacta.2015.01.191.

[37] K. Jalkanen et al. "Cycle Aging of Commercial NMC/Graphite Pouch Cells at Different Temperatures". In: *Applied Energy* 154 (Sept. 15, 2015), pp. 160–172. DOI: 10.1016/j.apenergy.2015.04.110.

[38] Sun Ung Kim et al. “Thermoelectrochemical Simulations of Performance and Abuse in 50-Ah Automotive Cells”. In: *Journal of Power Sources* 268 (Dec. 5, 2014), pp. 625–633. DOI: 10.1016/j.jpowsour.2014.06.080.

[39] John Cannarella and Craig B. Arnold. “State of Health and Charge Measurements in Lithium-Ion Batteries Using Mechanical Stress”. In: *Journal of Power Sources* 269 (2014), pp. 7–14.

[40] Wesley Chang et al. “Measuring Effective Stiffness of Li-Ion Batteries via Acoustic Signal Processing”. In: *Journal of Materials Chemistry A* 8.32 (Aug. 18, 2020), pp. 16624–16635. DOI: 10.1039/D0TA05552B.

[41] Ira Bloom et al. “Differential Voltage Analyses of High-Power, Lithium-Ion Cells: 1. Technique and Application”. In: *Journal of Power Sources* 139.1 (Jan. 4, 2005), pp. 295–303. DOI: 10.1016/j.jpowsour.2004.07.021.

[42] Hannah M Dahn et al. “User-Friendly Differential Voltage Analysis Freeware for the Analysis of Degradation Mechanisms in Li-Ion Batteries”. In: *Journal of The Electrochemical Society* 159.9 (2012), A1405–A1409.

[43] Matthieu Dubarry and Bor Yann Liaw. “Identify Capacity Fading Mechanism in a Commercial LiFePO4 Cell”. In: *Journal of Power Sources* 194.1 (2009), pp. 541–549. DOI: 10.1016/j.jpowsour.2009.05.036.

[44] Matthieu Dubarry et al. “Identifying Battery Aging Mechanisms in Large Format Li Ion Cells”. In: *Journal of Power Sources* 196.7 (2011), pp. 3420–3425. DOI: 10.1016/j.jpowsour.2010.07.029.

[45] Christoph R. Birkl et al. “Degradation Diagnostics for Lithium Ion Cells”. In: *Journal of Power Sources* 341 (Feb. 15, 2017), pp. 373–386. DOI: 10.1016/j.jpowsour.2016.12.011.

[46] Trishna Raj et al. “Investigation of Path-Dependent Degradation in Lithium-Ion Batteries**”. In: *Batteries & Supercaps* 3.12 (Dec. 1, 2020), pp. 1377–1385. DOI: 10.1002/batt.202000160.

[47] Chang-Hui Chen et al. “Development of Experimental Techniques for Parameterization of Multi-Scale Lithium-Ion Battery Models”. In: *Journal of The Electrochemical Society* 167.8 (May 15, 2020), p. 080534. DOI: 10.1149/1945-7111/ab9050.

[48] W. Weppner and R. A. Huggins. “Determination of the Kinetic Parameters of Mixed-Conducting Electrodes and Application to the System Li3Sb”. In: *Journal of The Electrochemical Society* 124.10 (Oct. 1, 1977), p. 1569. DOI: 10.1149/1.2133112.

[49] E. Deiss. “Spurious Chemical Diffusion Coefficients of Li+ in Electrode Materials Evaluated with GITT”. In: *Electrochimica Acta* 50.14 (May 5, 2005), pp. 2927–2932. DOI: 10.1016/j.electacta.2004.11.042.

[50] Jong Hoon Kim et al. “A New Direct Current Internal Resistance and State of Charge Relationship for the Li-Ion Battery Pulse Power Estimation”. In: *2007 7th Internatonal Conference on Power Electronics*. 2007 7th Internatonal Conference on Power Electronics. 22–Oct. 26, 2007, pp. 1173–1178. DOI: 10.1109/ICPE.2007.4692563.

[51] Peter Keil et al. “Calendar Aging of Lithium-Ion Batteries”. In: *Journal of The Electrochemical Society* 163.9 (July 6, 2016), A1872. DOI: 10.1149/2.0411609jes.

[52] Stefan Käbitz et al. “Cycle and Calendar Life Study of a Graphite|LiNi1/3Mn1/3Co1/3O2 Li-Ion High Energy System. Part A: Full Cell Characterization”. In: *Journal of Power Sources* 239 (Oct. 1, 2013), pp. 572–583. DOI: 10.1016/j.jpowsour.2013.03.045.

[53] Yu-Chi Chang, Jyh-Hwa Jong, and George Ting-Kuo Fey. “Kinetic Characterization of the Electrochemical Intercalation of Lithium Ions into Graphite Electrodes”. In: *Journal of The Electrochemical Society* 147.6 (2000), p. 2033. DOI: 10.1149/1.1393481.

[54] Sun Ung Kim. “Multicomponent Diffusion Systems”. Ann Arbor, Michigan: University of Michigan, 2013.

[55] Paola Villano, Maria Carewska, and Stefano Passerini. “Specific Heat Capacity of Lithium Polymer Battery Components”. In: *Thermochimica Acta* 402.1 (June 3, 2003), pp. 219–224. DOI: 10.1016/S0040-6031(02)00612-3.

[56] Xiaoxuan Zhang et al. “Evaluation of Convective Heat Transfer Coefficient and Specific Heat Capacity of a Lithium-Ion Battery Using Infrared Camera and Lumped Capacitance Method”. In: *Journal of Power Sources* 412 (Feb. 1, 2019), pp. 552–558. DOI: 10.1016/j.jpowsour.2018.11.064.

[57] Hossein Maleki et al. “Thermal Properties of Lithium-Ion Battery and Components”. In: *Journal of The Electrochemical Society* 146.3 (Mar. 1, 1999), p. 947. DOI: 10.1149/1.1391704.

[58] Zachary J. Schiffer, John Cannarella, and Craig B. Arnold. “Strain Derivatives for Practical Charge Rate Characterization of Lithium Ion Electrodes”. In: *Journal of The Electrochemical Society* 163.3 (Dec. 16, 2015), A427–A433. DOI: 10.1149/2.0091603jes.

[59] Bernhard Rieger et al. “Multi-Directional Laser Scanning as Innovative Method to Detect Local Cell Damage during Fast Charging of Lithium-Ion Cells”. In: *Journal of Energy Storage* 8 (2016), pp. 1–5.

[60] Gregory J Offer et al. “Module Design and Fault Diagnosis in Electric Vehicle Batteries”. In: *Journal of Power Sources* 206 (2012), pp. 383–392. DOI: 10.1016/j.jpowsour.2012.01.087.

[61] Billy Wu et al. “Coupled Thermal–Electrochemical Modelling of Uneven Heat Generation in Lithium-Ion Battery Packs”. In: *Journal of Power Sources* 243 (2013), pp. 544–554. DOI: 10.1016/j.jpowsour.2013.05.164.

[62] Ki Hyun Kwon et al. “A Two-Dimensional Modeling of a Lithium-Polymer Battery”. In: *Journal of Power Sources*. Special Issue Including Selected Papers Presented at the Second International Conference on Polymer Batteries and Fuel Cells Together with Regular Papers 163.1 (Dec. 7, 2006), pp. 151–157. DOI: 10.1016/j.jpowsour.2006.03.012.

[63] Gi-Heon Kim et al. “Multi-Domain Modeling of Lithium-Ion Batteries Encompassing Multi-Physics in Varied Length Scales”. In: *Journal of The Electrochemical Society* 158.8 (Aug. 1, 2011), A955–A969. DOI: 10.1149/1.3597614.

[64] Ui Seong Kim et al. “Modeling the Dependence of the Discharge Behavior of a Lithium-Ion Battery on the Environmental Temperature”. In: *Journal of The Electrochemical Society* 158.5 (May 1, 2011), A611–A618. DOI: 10.1149/1.3565179.

[65] Ui Seong Kim et al. “Modelling the Thermal Behaviour of a Lithium-Ion Battery during Charge”. In: *Journal of Power Sources* 196.11 (June 1, 2011), pp. 5115–5121. DOI: 10.1016/j.jpowsour.2011.01.103.

[66] Scott Peck and Matt Pierce. *Development of a Temperature-Dependent Li-Ion Battery Thermal Model*. SAE Technical Paper 2012-01-0117. Warrendale, PA: SAE International, Apr. 16, 2012. DOI: 10.4271/2012-01-0117.

[67] P. Ramadass et al. “Mathematical Modeling of the Capacity Fade of Li-Ion Cells”. In: *Journal of Power Sources* 123.2 (Sept. 20, 2003), pp. 230–240. DOI: 10.1016/S0378-7753(03)00531-7.

[68] R. B Wright et al. “Calendar- and Cycle-Life Studies of Advanced Technology Development Program Generation 1 Lithium-Ion Batteries”. In: *Journal of Power Sources* 110.2 (Aug. 22, 2002), pp. 445–470. DOI: 10.1016/S0378-7753(02)00210-0.

[69] Mark W. Verbrugge and Robert S. Conell. “Electrochemical and Thermal Characterization of Battery Modules Commensurate with Electric Vehicle Integration”. In: *Journal of The Electrochemical Society* 149.1 (Jan. 1, 2002), A45–A53. DOI: 10.1149/1.1426395.

[70] X Lin et al. “Online Parameterization of Lumped Thermal Dynamics in Cylindrical Lithium Ion Batteries for Core Temperature Estimation and Health Monitoring”. In: *IEEE Transactions on Control Systems Technology* 21.5 (2013), pp. 1745–1755. DOI: 10.1109/TCST.2012.2217143.

[71] Hector E. Perez et al. “Parameterization and Validation of an Integrated Electro-Thermal Cylindrical LFP Battery Model”. In: ASME 2012 5th Annual Dynamic Systems and Control Conference Joint with the JSME 2012 11th Motion and Vibration Conference. American Society of Mechanical Engineers Digital Collection, Sept. 17, 2013, pp. 41–50. DOI: 10.1115/DSCC2012-MOVIC2012-8782.

[72] Youngki Kim, Jason B. Siegel, and Anna G. Stefanopoulou. “A Computationally Efficient Thermal Model of Cylindrical Battery Cells for the Estimation of Radially Distributed Temperatures”. In: *2013 American Control Conference*. 2013 American Control Conference. June 2013, pp. 698–703. DOI: 10.1109/ACC.2013.6579917.

[73] Youngki Kim et al. “The Estimation of Temperature Distribution in Cylindrical Battery Cells Under Unknown Cooling Conditions”. In: *IEEE Transactions on Control Systems Technology* 22.6 (Nov. 2014), pp. 2277–2286. DOI: 10.1109/TCST.2014.2309492.

[74] J. Christensen, D. Cook, and P. Albertus. “An Efficient Parallelizable 3D Thermoelectrochemical Model of a Li-Ion Cell”. In: *Journal of the Electrochemical Society* 160.11 (Jan. 2013), A2258–A2267. DOI: 10.1149/2.086311jes.

[75] Marc Doyle, Thomas F Fuller, and John Newman. “Modeling of Galvanostatic Charge and Discharge of the Lithium/Polymer/Insertion Cell”. In: *Journal of The Electrochemical Society* 140.6 (1993), pp. 1526–1533. DOI: 10.1149/1.2221597.

[76] Thomas F Fuller, Marc Doyle, and John Newman. "Simulation and Optimization of the Dual Lithium Ion Insertion Cell". In: *Journal of The Electrochemical Society* 141.1 (1994), pp. 1–10. DOI: 10.1149/1.2054684.

[77] Thomas F Fuller, Marc Doyle, and John Newman. "Relaxation Phenomena in Lithium-Ion-Insertion Cells". In: *Journal of The Electrochemical Society* 141.4 (1994), pp. 982–990. DOI: 10.1149/1.2054868.

[78] Sun Ung Kim and Charles W. Monroe. "Increasing the Rate Capability of Batteries with Electrolyte Flow". In: *Applied Energy* 103 (Mar. 1, 2013), pp. 207–211. DOI: 10.1016/j.apenergy.2012.09.028.

[79] Jing Liu and Charles W. Monroe. "Solute-Volume Effects in Electrolyte Transport". In: *Electrochimica Acta* 135 (July 20, 2014), pp. 447–460. DOI: 10.1016/j.electacta.2014.05.009.

[80] John S. Newman and Charles W. Tobias. "Theoretical Analysis of Current Distribution in Porous Electrodes". In: *Journal of The Electrochemical Society* 109.12 (Dec. 1, 1962), p. 1183. DOI: 10.1149/1.2425269.

[81] Venkat Srinivasan and C Y Wang. "Analysis of Electrochemical and Thermal Behavior of Li-Ion Cells". In: *Journal of The Electrochemical Society* 150.1 (2003), A98–A106. DOI: 10.1149/1.1526512.

[82] Meng Guo, Godfrey Sikha, and Ralph E White. "Single-Particle Model for a Lithium-Ion Cell: Thermal Behavior". In: *Journal of The Electrochemical Society* 158.2 (2011), A122–A132. DOI: 10.1149/1.3521314.

[83] Karthikeyan Kumaresan, Godfrey Sikha, and Ralph E. White. "Thermal Model for a Li-Ion Cell". In: *Journal of The Electrochemical Society* 155.2 (Feb. 1, 2008), A164–A171. DOI: 10.1149/1.2817888.

[84] Nerea Nieto et al. "Thermal Modeling of Large Format Lithium-Ion Cells". In: *Journal of The Electrochemical Society* 160.2 (Nov. 30, 2012), A212. DOI: 10.1149/2.042302jes.

[85] E Prada et al. "Simplified Electrochemical and Thermal Model of LiFePO4-Graphite Li-Ion Batteries for Fast Charge Applications". In: *Journal of The Electrochemical Society* 159.9 (2012), A1508–A1519. DOI: 10.1149/2.064209jes.

[86] Meng Xu et al. "Two-Dimensional Electrochemical–Thermal Coupled Modeling of Cylindrical LiFePO4 Batteries". In: *Journal of Power Sources* 256 (June 15, 2014), pp. 233–243. DOI: 10.1016/j.jpowsour.2014.01.070.

[87] Matthias Fleckenstein et al. "Current Density and State of Charge Inhomogeneities in Li-Ion Battery Cells with LiFePO4 as Cathode Material Due to Temperature Gradients". In: *Journal of Power Sources* 196.10 (May 15, 2011), pp. 4769–4778. DOI: 10.1016/j.jpowsour.2011.01.043.

[88] D. Bernardi, E. Pawlikowski, and J. Newman. "A General Energy Balance for Battery Systems". In: *Journal of The Electrochemical Society* 132.1 (Jan. 1, 1985), pp. 5–12. DOI: 10.1149/1.2113792.

[89] Christophe Forgez et al. "Thermal Modeling of a Cylindrical LiFePO4/Graphite Lithium-Ion Battery". In: *Journal of Power Sources* 195.9 (May 1, 2010), pp. 2961–2968. DOI: 10.1016/j.jpowsour.2009.10.105.

[90] S. Al Hallaj et al. “Entropy Changes Due to Structural Transformation in the Graphite Anode and Phase Change of the LiCoO2 Cathode”. In: *Journal of The Electrochemical Society* 147.7 (July 1, 2000), p. 2432. DOI: 10.1149/1.1393549.

[91] Karen E. Thomas, Christian Bogatu, and John Newman. “Measurement of the Entropy of Reaction as a Function of State of Charge in Doped and Undoped Lithium Manganese Oxide”. In: *Journal of The Electrochemical Society* 148.6 (June 1, 2001), A570–A575. DOI: 10.1149/1.1369365.

[92] M. R. Zakin et al. “Dependence of Metal Cluster Reaction Kinetics on Charge State. I. Reaction of Neutral (Nb x) and Ionic (Nb + x , Nb - x) Niobium Clusters with D 2”. In: *The Journal of Chemical Physics* 88.6 (1988), pp. 3555–3560. DOI: 10.1063/1.453903.

[93] Carosena Meola, Simone Boccardi, and Giovanni maria Carlomagno. “Chapter 4 - Nondestructive Testing With Infrared Thermography”. In: *Infrared Thermography in the Evaluation of Aerospace Composite Materials*. Ed. by Carosena Meola, Simone Boccardi, and Giovanni maria Carlomagno. Woodhead Publishing, Jan. 1, 2017, pp. 85–125. DOI: 10.1016/B978-1-78242-171-9.00004-8.

[94] Huai Wang, Marco Liserre, and Frede Blaabjerg. “Toward Reliable Power Electronics: Challenges, Design Tools, and Opportunities”. In: *IEEE Industrial Electronics Magazine* 7.2 (June 2013), pp. 17–26. DOI: 10.1109/MIE.2013.2252958.

[95] Mehrdad Mastali et al. “Electrochemical-Thermal Modeling and Experimental Validation of Commercial Graphite/LiFePO4 Pouch Lithium-Ion Batteries”. In: *International Journal of Thermal Sciences* 129 (July 1, 2018), pp. 218–230. DOI: 10.1016/j.ijthermalsci.2018.03.004.

[96] Hossein Maleki et al. “Thermal Stability Studies of Li-Ion Cells and Components”. In: *Journal of The Electrochemical Society* 146.9 (1999), pp. 3224–3229. DOI: 10.1149/1.1392458.

[97] Jie Lin et al. *Multiscale Coupling of Surface Temperature with Solid Diffusion in Large Lithium-Ion Pouch Cells*. Sept. 27, 2021. arXiv: 2109.12903 [physics, stat]. URL: http://arxiv.org/abs/2109.12903 (visited on 10/13/2021).

[98] W M Deen. *Analysis of Transport Phenomena*. OUP USA, 2012.

[99] Marc Doyle and Yuris Fuentes. “Computer Simulations of a Lithium-Ion Polymer Battery and Implications for Higher Capacity Next-Generation Battery Designs”. In: *Journal of The Electrochemical Society* 150.6 (2003), A706–A713. DOI: 10.1149/1.1569478.

[100] J Newman and K E Thomas-Alyea. *Electrochemical Systems*. Wiley, 2012.

[101] Sarah Grace Stewart. “Determination of Transport Properties and Optimization of Lithium-Ion Batteries”. PhD thesis. United States – California: University of California, Berkeley, 2007. 158 pp.

[102] Jing Liu and Charles W Monroe. “On the Characterization of Battery Electrolytes with Polarization Cells”. In: *Electrochimica Acta* 167 (2015), pp. 357–363. DOI: 10.1016/j.electacta.2015.03.104.

[103] Hossein Maleki et al. "Li-Ion Polymer Cells Thermal Property Changes as a Function of Cycle-Life". In: *Journal of Power Sources* 263 (Oct. 1, 2014), pp. 223–230. DOI: 10.1016/j.jpowsour.2014.04.033.

[104] Howie N Chu. *Howiechu/Lock-in-Thermography-Model: Electrochemical Thermal Model*. Aug. 2019. DOI: 10.5281/zenodo.3369805.

[105] R B Bird, E N Lightfoot, and W E Stewart. *Transport Phenomena*. Wiley, 2002.

[106] S J Bazinski and X Wang. "The Influence of Cell Temperature on the Entropic Coefficient of a Lithium Iron Phosphate (LFP) Pouch Cell". In: *Journal of The Electrochemical Society* 161.1 (Jan. 2014), A168–A175. DOI: 10.1149/2.082401jes.

[107] I Bloom et al. "An Accelerated Calendar and Cycle Life Study of Li-Ion Cells". In: *Journal of Power Sources* 101.2 (Oct. 15, 2001), pp. 238–247. DOI: 10.1016/S0378-7753(01)00783-2.

[108] Arijit Guha and Amit Patra. "State of Health Estimation of Lithium-Ion Batteries Using Capacity Fade and Internal Resistance Growth Models". In: *IEEE Transactions on Transportation Electrification* 4.1 (Mar. 2018), pp. 135–146. DOI: 10.1109/TTE.2017.2776558.

[109] Dian Wang, Yun Bao, and Jianjun Shi. "Online Lithium-Ion Battery Internal Resistance Measurement Application in State-of-Charge Estimation Using the Extended Kalman Filter". In: *Energies* 10.9 (9 Sept. 2017), p. 1284. DOI: 10.3390/en10091284.

[110] Matthew Li et al. "30 Years of Lithium-Ion Batteries". In: *Advanced Materials* 30.33 (2018), p. 1800561. DOI: 10.1002/adma.201800561.

[111] Wangda Li, Bohang Song, and Arumugam Manthiram. "High-Voltage Positive Electrode Materials for Lithium-Ion Batteries". In: *Chemical Society Reviews* 46.10 (2017), pp. 3006–3059. DOI: 10.1039/C6CS00875E.

[112] Ira Bloom et al. "Differential Voltage Analyses of High-Power Lithium-Ion Cells. 4. Cells Containing NMC". In: *Journal of Power Sources* 195.3 (Feb. 1, 2010), pp. 877–882. DOI: 10.1016/j.jpowsour.2009.08.019.

[113] Peter Keil and Andreas Jossen. "Calendar Aging of NCA Lithium-Ion Batteries Investigated by Differential Voltage Analysis and Coulomb Tracking". In: *Journal of The Electrochemical Society* 164.1 (2017), A6066–A6074. DOI: 10.1149/2.0091701jes.

[114] Maitane Berecibar et al. "Online State of Health Estimation on NMC Cells Based on Predictive Analytics". In: *Journal of Power Sources* 320 (July 15, 2016), pp. 239–250. DOI: 10.1016/j.jpowsour.2016.04.109.

[115] Tianhong Hou and Charles W. Monroe. "Composition-Dependent Thermodynamic and Mass-Transport Characterization of Lithium Hexafluorophosphate in Propylene Carbonate". In: *Electrochimica Acta* 332 (Feb. 1, 2020), p. 135085. DOI: 10.1016/j.electacta.2019.135085.

[116] Andrew A. Wang et al. "Shifting-Reference Concentration Cells to Refine Composition-Dependent Transport Characterization of Binary Lithium-Ion Electrolytes". In: *Electrochimica Acta* 358 (Oct. 20, 2020), p. 136688. DOI: 10.1016/j.electacta.2020.136688.

[117] Madeleine Ecker et al. “Parameterization of a Physico-Chemical Model of a Lithium-Ion Battery”. In: *Journal of The Electrochemical Society* 162.9 (2015), A1836–A1848. DOI: 10.1149/2.0551509jes.

[118] Johannes Landesfeind and Hubert A. Gasteiger. “Temperature and Concentration Dependence of the Ionic Transport Properties of Lithium-Ion Battery Electrolytes”. In: *Journal of The Electrochemical Society* 166.14 (2019), A3079–A3097. DOI: 10.1149/2.0571912jes.

[119] Ratnakumar V. Bugga and Marshall C. Smart. “Lithium Plating Behavior in Lithium-Ion Cells”. In: *ECS Transactions* 25.36 (Apr. 16, 2010), p. 241. DOI: 10.1149/1.3393860.

[120] Jacqueline S. Edge et al. “Lithium Ion Battery Degradation: What You Need to Know”. In: *Physical Chemistry Chemical Physics* 23.14 (2021), pp. 8200–8221. DOI: 10.1039/D1CP00359C.

[121] Xiao-Guang Yang et al. “Modeling of Lithium Plating Induced Aging of Lithium-Ion Batteries: Transition from Linear to Nonlinear Aging”. In: *Journal of Power Sources* 360 (Aug. 31, 2017), pp. 28–40. DOI: 10.1016/j.jpowsour.2017.05.110.

[122] Ian D. Campbell et al. “How Observable Is Lithium Plating? Differential Voltage Analysis to Identify and Quantify Lithium Plating Following Fast Charging of Cold Lithium-Ion Batteries”. In: *Journal of The Electrochemical Society* 166.4 (Mar. 6, 2019), A725. DOI: 10.1149/2.0821904jes.

[123] Pallavi Verma, Pascal Maire, and Petr Novák. “A Review of the Features and Analyses of the Solid Electrolyte Interphase in Li-Ion Batteries”. In: *Electrochimica Acta* 55.22 (Sept. 1, 2010), pp. 6332–6341. DOI: 10.1016/j.electacta.2010.05.072.

[124] Jorn M. Reniers, Grietus Mulder, and David A. Howey. “Review and Performance Comparison of Mechanical-Chemical Degradation Models for Lithium-Ion Batteries”. In: *Journal of The Electrochemical Society* 166.14 (2019), A3189–A3200. DOI: 10.1149/2.0281914jes.

[125] Johannes Schmalstieg et al. “Full Cell Parameterization of a High-Power Lithium-Ion Battery for a Physico-Chemical Model: Part I. Physical and Electrochemical Parameters”. In: *Journal of The Electrochemical Society* 165.16 (2018), A3799–A3810. DOI: 10.1149/2.0321816jes.

[126] Jiantie Xu et al. “The Effect of Different Binders on Electrochemical Properties of LiNi1/3Mn1/3Co1/3O2 Cathode Material in Lithium Ion Batteries”. In: *Journal of Power Sources* 225 (Mar. 1, 2013), pp. 172–178. DOI: 10.1016/j.jpowsour.2012.10.033.

[127] Jette K. Mathiesen et al. “Understanding the Structural Changes in Lithiated Graphite through High-Resolution Operando Powder X-Ray Diffraction”. In: *Carbon* 153 (Nov. 1, 2019), pp. 347–354. DOI: 10.1016/j.carbon.2019.06.103.

[128] John Cannarella. “Coupled Mechanical and Electrochemical Phenomena in Lithium-Ion Batteries”. Princeton University, 2015.

[129] Martin Wünsch, Jörg Kaufman, and Dirk Uwe Sauer. "Investigation of the Influence of Different Bracing of Automotive Pouch Cells on Cyclic Liefetime and Impedance Spectra". In: *Journal of Energy Storage* 21 (Feb. 1, 2019), pp. 149–155. DOI: 10.1016/j.est.2018.11.019.

[130] M. R. Wagner et al. "Dilatometric and Mass Spectrometric Investigations on Lithium Ion Battery Anode Materials". In: *Analytical and Bioanalytical Chemistry* 379.2 (May 1, 2004), pp. 272–276. DOI: 10.1007/s00216-004-2570-9.

[131] S. Panchal et al. "Cycling Degradation Testing and Analysis of a LiFePO4 Battery at Actual Conditions". In: *International Journal of Energy Research* 41.15 (2017), pp. 2565–2575. DOI: 10.1002/er.3837.